Title
Three-dimensional structural characterization of chromosome pairing and synapsis

Author
Fung, Jennifer C.

Publication Date
1996

Peer reviewed|Thesis/dissertation

Three-Dimensional Structural Characterization of Chromosome

Pairing and Synapsis

by

Jennifer C. Fung

DISSERTATION

Submitted in partial satisfaction of the requirements for the degree of

DOCTOR OF PHILOSOPHY

in

Biophysics

in the

GRADUATE DIVISION

of the

UNIVERSITY OF CALIFORNIA

San Francisco

Date **University Librarian**

Degree Conferred: . . . . . .

Dedication

This thesis is dedicated to my parents, Wallace and May, for all the love and support they provided throughout the years, and to my aunt, Susan Kung, who as a surrogate parent always watched over me and encouraged me in all my endeavors.

Acknowledgments

This work could not have been accomplished without the friendship and help of several special people who became part of my life during my time as a graduate student at UCSF.

First of all, I would like to especially thank, John Sedat, who as a mentor embodied many of the qualities that I hope to aspire to as I continue my career in science. Your insistence on high caliber research, your constant pursuit of new methods and approaches, and your selflessness in promoting others above yourself are qualities that I have learned to appreciate while being in your lab. In addition, your weird stories and far-out topics of conversation, though not something I want to duplicate, helped make the lab a fun place to work;

Dave Agard, whose advice kept me on track and who always had the right answer to any question I brought to him;

Special thanks goes to Wallace Marshall, who not only is a good husband, but one of the best colleagues I had in science. You were there to help me when work was not going well and extremely happy for me when it did. You were instrumental in helping formulate some of the questions that eventually led to some results in my research. You helped me out in ways to numerous to detail. You were also the only person that could beat me in DOOM;

Sue Parmelee, thank you very much for being a good colleague as well as a good friend. I always came to you for sound advice, good discussions, and sometimes a little sympathy. Also thank you for letting me participate in some of your outdoor adventures. The white-water rafting, caving, back-packing, and back-country skiing were the most exciting and memorable events during my time at graduate school;

Abby Dernburg, I was very privileged to have you both as a colleague and a friend. I appreciate how you helped me in the early days to get a minimal grasp of the biology. You showed me what it takes to be an excellent scientist and taught me by example that one should always strive for the best and that nothing is impossible;

Jason Swedlow, who convinced me to try out John's lab for a rotation in the first place. Thanks for all the good advice, the sympathetic ear, and the falsetto singing that used to fill the lab in the wee hours of the morning;

I especially like to thank Hans Chen who worked tirelessly to make the best imaging system available for our research. Thank you for patiently tolerating our constant late night telephoning and our occasional flares of temper. Much of our work was made easy because of your excellent ability to think up creative solution to our problems;

Thanks to Diana Diggs (Hughes) who constantly had to devise new methods to analyze our data. Your innovative ideas and the speed in which you incorporated them made it possible to complete this thesis;

Angus McDonald, thank you for keeping the software system up and running. I know its a hard task and we often don't show enough appreciation;

Mel Jones, thank you for keeping the hardware in working order and letting us have one less thing to worry about;

For Weiping Liu, a special thanks for finally putting the reconstruction software together into one package. You are a good friend as well as a fun person to have worked with on the tomographic automation;

To Hank Bass, thanks for the peppage and the good discussions on corn, meiosis and the number 3;

To Bethe Scalettar and Kelly Dawe, thank you for all the early help in starting me out on working with the corn;

Thanks to Karen Han for being a good friend and tolerating my jokes. I enjoyed working with you on the EM. Also thank you for letting me know that fashion design is much more competitve than science;

As for Michael Braunfeld, thanks for all the interesting gossip. I will miss sharing complaints about the EM;

Thanks also to Mei Li, who provided advice, conversation and jelly beans in equal measure;

Also an appreciative thanks to all my bay-mates, Guo Feng Zhang, Hiro Itoi, Yoji Urata who kept their side of the bay clean and didn't seem to mind my mess too much and the fact that it tended to spread;

To Michael Paddy and Yasushi Hiraoka, thanks for all the early advice;

To Wendy, thanks for being a good friend and classmate;

And special thanks to Julie Ransom, who kept all of the biophysics students on the right track and made sure we were all doing ok;

To Stasia and Gina, who always kept me company and made sure I occasionally came home at night;

To my sister and brother, Elaine and Denis, thank you for enriching my life by taking me to all those expensive restaurants and shows in SF which I couldn't afford on a graduate student salary;

Finally, I would like to thank all my relatives in the Bay Area who have encouraged me during my time in graduate school. To my grandmother, my aunts: Helen, Dolly, Julia, and Alice, my Uncle Tai, and my cousins Christine and Eddy, thank you for all your support. Also I would like to extend my gratitude to my Aunt Rita and Uncle James who provided a place for me to live during my last year in graduate school.

Permission to reprint two 1996 articles: Phase Behavior of Ordered Diblock Copolymer Blends: Effects of Compositional Heterogeneity in Macromolecules 29(13): 4494-4507 and Architecture-Induced Phase Immiscibility in a Diblock/Multiblock Copolymer Blend in Macromolecules 29 (8): 2850-2856, is provided by Macromolecules through the American Chemical Society for paper and microfilm copies only.

ABSTRACT

Three-dimensional Structural Characterization of Chromosome Pairing and Synapsis

by

Jennifer C. Fung

Chromosome organization is a highly dynamic process characterized by changes in a chromosome's overall structure and motion. Such changes are required to adapt to the myriad of functions that a chromosome must perform in its disparate roles in transcription, replication, and segregation. Recently, development of three-dimensional (3-D) microscopy both at the optical and electron microscopic level, in conjunction with fluorescence in-situ hybridization (FISH) and in vivo imaging techniques, have allowed direct visualization of chromosomal arrangements and interactions. Using these microscopical techniques, this thesis addresses two levels of chromosome organization 1) chromosome synapsis through the assembly of the synaptonemal complex (SC) and 2) somatic pairing of homologous chromosomes during Drosophila embryogenesis. To understand how chromosomes synapse, electron tomography was used to analyze the ultrastructure of the SC. The SC is a structure that forms during the first meiotic division and is thought to mediate intimate synapsis between homologous chromosomes. It also

believed to have a role in genetic recombination and the creation chiasmata. In order to understand how the structural features of the synaptonemal complex correlate with its various functions, I analyzed the structural changes that occurred during two different timepoints in the synapsis process. This involved, in part, developing some of the techniques used to reconstruct the tomographic data. The results showed that using this approach, novel components of the SC were revealed and that the temporal pattern for their incorporation into the SC could also be discerned. The other major part of this thesis addresses the question how pairing between homologous chromomes is achieved. This study focused on the examination of the pairing state of several loci from the left arm of chromosome 2 at various stages of Drosophila embryogenesis. This study resulted in showing that pairing occurred in a site-specific fashion. In addition, it was determined that, at least for one site, the mechanism of pairing involves the random collision of chromosomal sites and and does not require an active mechanism to pull homologous sites together.

Table of Contents

List of Tables

List of Figures

Preface

Chromosome organization is a highly dynamic process characterized by great changes in overall structure and motion. Within one cell cycle, chromosomes can undergo a 10,000 fold linear compaction of DNA forming tightly folded metaphase chromosomes which can later decondense into the 36-42 fold compaction ratio more typical of the 10-30 nm fiber architecture of chromosomes found during interphase. Besides intrachromosomal changes, interchromosomal interactions also exist and are key components in the organization of the interphase and meiotic nucleus. One example is the pairing of homologous chromosomes which occurs primarily during meiosis for most organisms but also can be found as part of the natural order of chromosomes as in the case of Dipteran insects. Understanding the dynamics of some of these chromatin-related processes forms the main topic of my thesis. In many cases, the questions relating to chromosome interactions can only be explored using 3-D microscopy. Part of my thesis is devoted to the development of such microscopic techniques as well as showing how such techniques can be extended to address many other relevant topics both in biology and material sciences. The following paragraphs outline and summarize the subsequent chapters that form the bulk of my work.

Chapter 1 describes how somatic pairing develops during Drosophila embryogenesis. Using 3-D optical sectioning microscopy and fluorescence in situ hybridization (FISH), a time course was developed showing that pairing of chromosome arm 2L occurred in a site-specific manner. The histone locus was shown to pair first after 2 hours of development in cycle 14 followed by the Responder locus which paired after approximately 2.5 hours of embryogenesis. In the end, all loci became paired within 6 to 13 hrs of development. In general, no zippering of the chromosome from one site to the next was seen, instead, all sites seemed to pair independently from each other. Another key part of this study was to demonstrate for the first time a mechanism by which pairing

takes place. By using changes in nuclear morphology, i.e. nuclear length, to substitute as a measure of time, pairing events obtained by FISH could be recorded with measurements of nuclear elongation to later represent pairing as a function of the elasped time. At the same time, profiles of pairing events were also generated by simulations based on current models for homolog pairing. Two models, random walk and directed motion models were tested. By comparing the histone profiles for pairing with those generated by the two models, it was clear that histone pairing arose from motion due to diffusion of the sites. This model of histone pairing was then used to explain why, in strains where histone had been translocated or inverted, the pairing frequency of histone was lower than found in wild type.

Chapter 2 describes the assembly of the synaptonemal complex in Zea mays meiocytes using intermediate voltage electron tomography. The synaptonemal complex is a structure that mediates the synapsis between homologous chromosomes during meiosis. Previous studies had not revealed any detailed information about its structure and how it changes during progression through meiosis. Part of my thesis research was to characterize the assembly of the synaptonemal complex in maize meiocytes. A combination of high pressure freezing techniques and tomography was used to show the existence of novel structures in the central region of the mature synaptonemal complex. A careful examination of the central region showed that it consists of three parts, a novel 8- to 10-nm cable-like structure, a more globular 50-nm structure, and a set of transverse elements. In contrast, early in the assembly of the synaptonemal complex, when the homologs are just beginning to synapse, only the 8- to 10-nm cable is visible. This suggests that the 8-to 10-nm cable is the first to be assembled and only later do the other components of the central region come into place.

Chapter 3 describes my original thesis project to determine the higher order organization of chromatin using electron tomographic methods. Part of the architecture of chromatin is the 130 nm fiber which had been identified as an intermediate fiber in the

folding pathway of the mitotic chromosome. The goal of the research was to elucidate the folding pattern of this fiber. The majority of this work was devoted to finding ways to improve the interpretation of the tightly packed architecture. Efforts focused on devising new chromatin stains, improving data collection parameters, using image processing techniques to enhance the reconstruction and attempting to decondense the chromatin for greater separation between fibers.

Chapter 4 describes the development of the automated data collection and reconstruction package used for the electron tomographics studies contained in chapter 2 and in the appendices. A general description of all the steps involved in generating a reconstruction using our system is included.

Chapter 5 is a discussion of the algorithms developed to align the tomgraphic sections. There are four algorithms that make up the consolidated alignment program: BEAD_FINDER, BEAD_MATCHER, BEAD_CHASER, and BEAD_ALIGN. Since gold beads were used as fidicial markers for aligning the tilt sections from the tomography data stack, several programs were developed to find, sort and analyze the beads so that the end result would be an aligned data stack. The BEAD_MATCHER program was my main contribution. The other programs were modified by both me and Weiping Liu but originally written by Craig Abbey except for BEAD_CHASER which was written by Weiping Liu.

The Appendix contains collaborative work arising from the reconstruction of 3-D morphology of copolymer blends. For these two studies, we focused on examining the phase behavior of equimolar diblock/multiblock and copolymer/copolymer blends. Tomographic data of these blends were used to characterize their exact 3-D morphology.

Chapter 1 :

Dynamics of Homologous Chromosome Pairing During Drosophila Embryonic Development

Summary

The mechanism by which homologous chromosomes pair is currently unknown. Here, we use in-situ hybridzation in combination with three-dimensional optical microscopy to show that somatic homologous pairing of chromosome arm 2L in Drosophila occurs by independent initiation of pairing at discrete loci rather than by a processive zippering of sites along the length of chromosome. By comparing the dynamics of pairing to simulations based on different models of pairing motion, we show that the observed pairing kinetics are most consistent with a constrained random walk model and not consistent with a directed motion model. Thus, we conclude that simple random contacts through diffusion could suffice to allow pairing of homologous sites.

Introduction

In eukaryotes, a chromosome is sometimes non-randomly associated with its homolog over part or all of its length. For some organisms such as Dipteran insects, this association, termed homologous chromosome pairing, is observed to be a normal part of nuclear organization (Metz, 1916). For most other organisms, less extensive homologous pairing is seen (e.g. Vourc'h et al, 1993; Lewis et al, 1993). For all sexually reproducing organisms, however, homologous pairing figures prominently during meiosis. Such pairing leads to a tight synapsis of homologs during the first meiotic prophase and where failure to attain this synapsis usually results in chromosome missegregation (Roeder, 1995).

Pairing of homologous chromosomes can also influence gene regulation. In Drosophila melanogaster, there are a large number of cases in which gene expression can be modulated by physical pairing of homologous loci (reviewed in Tartof and Henikoff, 1991). Similar observations have been reported in such widely divergent organisms as Antirhinnum majus (Bollman et al., 1991) and Neurospora crassa (Arramayo, 1996). In these cases, either suppression or enhancement of a phenotype is observed when pairing is

disrupted by chromosomal rearrangements. In cases where it has been explicitly tested (e.g. Goldsborough and Kornberg, 1996), the effects can be accounted for by changes levels of transcription that accompany the disruption of pairing.

Homologous chromosome pairing is also thought to play a role in other epigenetic phenomena such as genomic imprinting and paramutation. Genetic imprinting, in which the parental origin of a particular allele affects its expression, may also involve physical association between the homologous materal and paternal allele (LaSalle and Lalande, 1996). In plants, paramutation, an interaction between alleles that leads to a directed heritable change at a locus at high frequency is likewise thought to be promoted from interactions arising from homologous pairing (Patterson, 1995). Moreover, methylation transfer, believed to be important for many epigenetic phenenoma, may require pairing of the homologs as an initial and crucial step in the process (Colot et al., 1996).

Although progress is being made in determining the biological relevance of homologous pairing, few insights can be reported in elucidating the mechanism for how homologs become paired. This is primarily due to the inability so far to directly monitor two homologous sites as pairing proceeds. Therefore, many basic questions about how pairing develops still remain unanswered. Is the homology search carried out by discrete sites or simultaneously along the entire length of the chromosome? How do those sites which undergo homology search locate each other in the nucleus? Numerous models have been put forth for how this pairing might take place (as reviewed in Loidl, 1990). In general, these models can be characterized as those emphasizing active movement of chromatin to bring homologous regions into contact or those relying mainly on fortuitous encounters of homologous sites brought about by random movements of the chromatin by diffusion (also referred to here as random walk motion). Further complicating this issue is what role, if any, has nuclear organization in facilitating the homology search. This question has been raised by numerous studies suggesting that prealignment through bouquet formation, an alignment of telomeres and chromosomes within meiotic nuclei

(reviewed in Dernburg et al., 1995; Scherthan, 1996), Rabl orientation, a centromere to telomere polarity found in interphase nuclei (Rabl, 1865; Fussel, 1987) or juxtaposition of chromosomes during metaphase congression (Maguire, 1983a) can reduce the area over which homology search takes place and is thus a necessary part in the pairing process. We attempt to address these questions and related ones by following the kinetics of homolog pairing in Drosophila embryos.

Drosophila melanogaster offers a unique system in which to study homologous pairing. Drosophila chromosomes are thought to be homologously associated in the early stages of development in addition to its association observed during meiosis . For instance, the giant polytene chromosomes found in larval tissue, exhibit a close synapsis of homologs along their entire lengths. Observations of a side-by-side alignment of metaphase chromosomes in squashed neuroblast preparations lend further support that homologs pair early in this organism (Metz, 1916). Furthermore, one study probing homologous pairing during embryogenesis for a single site, the histone locus, suggests that the onset of homologous pairing occurs early in the embryo after the 13th nuclear division (Hiraoka et al., 1993).

There are several advantages for studying the dynamics of homolog pairing during the well-characterized stages of embryonic development (reviewed in Foe, 1993). Between the 10-13th nuclear cycles, nuclei divide in tight synchrony every 10-17 minutes as a monolayer at the embryo surface. At cycle 14, interphase increases in duration and is followed by a patterned mitosis where patches of cells enter mitosis at different points in time. Up until gastrulation, about an hour into cycle 14, the embryo exists as a cellular blastoderm such that cells continue to be arrayed as a monolayer at the surface of the embryo. So within one embryo, a synchronous population of nuclei in an defined orientation is available for statistical analysis of pairing events. After cycle 14, most cells, unlike at earlier stages, have defined cell fates and undergo two more cell cycles, again with patterned mitosies, ending with a terminal intephase at cycle 16. Imaginal discs and

neuroblasts are the exceptions, the former undergoes one more cell division and the latter several cycles more. Although nuclei no longer behave identically at these later developmental stages, analysis of how pairing changes between the differentiated groups of cells can give us information on what factors influence a chromosome's ability to pair. Also aiding in the pairing analysis is that the embryonic developmental stages described here are all extremely amenable to the 3-D imaging techniques needed to properly observe the pairing. Particularly useful is that many of these nuclear cycles can be imaged as they proceed in vivo, which is important for developing time courses necessary for determining the mechanisms governing the homology search.

To elucidate how pairing develops during Drosophila development, we used fluorescence in situ hybridization (FISH) and immunofluorescence under conditions that preserve nuclear and chromosomes substructure combined with high resolution 3-D optical microscopy to examine how pairing evolves along a chromosome arm. The pairing frequencies of 11 loci distributed over chromosome arm 2L were evaluated at several timepoints during Drosophila development. This analysis revealed that all 11 loci are paired within 13 hours of development demonstrating that pairing along the entire length of the chromosome is attained very early in the Drosophila life cycle. More crucially, the frequencies of pairing at different sites indicate that this side-by- side alignment is achieved through the independent initiation of pairing at discrete loci rather than by a processive zippering of sites along the length of chromosome.

Towards elucidating the mechanisms involved in the homology search, we provide evidence that simple random contacts through diffusion are sufficient to allow pairing of a homologous sites. We measured the time course of pairing of the histone locus through a cycle of interphase and compared our observations to computer simulations of pairing based upon different models of chromosome motion. From this comparison, we find that the pairing kinetics of this locus are most consistent with a constrained random walk model, rather than with a directed motion model.

Results

Different sites along a chromosome arm show distinct pairing dynamics

To characterize how pairing initiates for a large chromosomal region, we hybridized probes to a series of sites spanning chromosome arm 2L at several timepoints in Drosophila development. We chose to focus on chromosome arm 2L since the onset of pairing for one locus, the histone gene cluster, had previously been determined (Hiraoka et al., 1993) and could be compared to pairing of other sites. FISH probes were made as described in Dernburg et al. (1996) to eight sites spanning 2L, each no more than five polytene sections apart, and to three sites in the heterochromatin. Probes to both euchromatic and heterochromatic sites were synthesized to detect any differences in pairing that might be associated with the different chromatin states. Figure 1A diagrams the probes and their positions along 2L.

Embryos at several different developmental stages (2.0 (cycle 13), 2.3 (cycle 14), 4, 6, and 13 hours after egg deposition (AED)) and wing discs dissected from climbing third instar larvae were fixed and then hybridized with one or two FISH probes (see Experimental Procedures). After hybridization, both embryos and wing discs were stained with antibodies to the nuclear lamin to mark the volume of the nucleus. This marker was particularly useful for at later stages of development when nuclei are sometimes smaller and more densely packed. To confine our pairing observations to interphase nuclei, nuclei were counterstained with DAPI.

A wide field deconvolution optical microscope with a CCD camera was used to record 3-D images of hybridized nuclei. Figure 1B shows a representative focal series of optical sections collected from nuclei of an embryo at cycle 14. Signals corresponding to two FISH probes, the anti-lamin antibody (middle right) and DAPI (far right) were recorded. Examination of the full 3-D nuclear volume showed that each interphase nucleus generally contained one or two FISH signals of similar shape and size which are interpreted

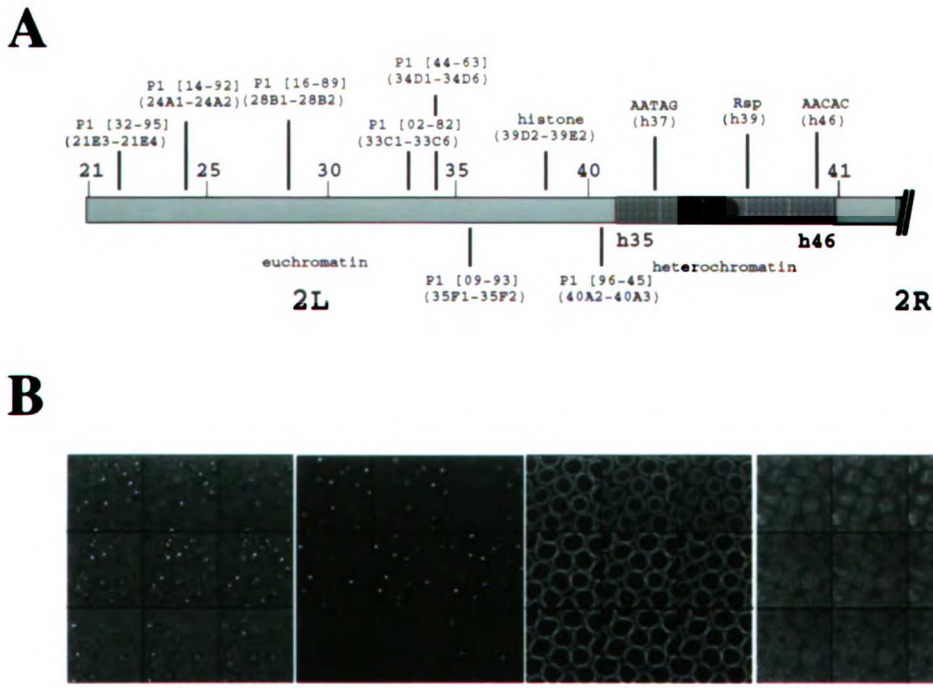

Figure 1.1 Probe positions and probe signal in a 3-D data stack of cycle 14 embryonic nuclei.
(A) Names and positions of probes on chromosome 2. Locations refer to cytological map positions determined by hybridization to polytene or metphase spread chromosomes. P1 refers to probes from P1 clones. Rsp refers to the Responder locus. Probes were either labeled directly with rhodamine-4-UTP or indirectly with digoxigenin-dUTP and detected using rhodamine, fluorescein or Cy 5 labeld anti-digoxigenin antibodies.
(B) Representative multi-wavelength 3-D data stack from a cycle 14 embryo. A subset of 9 sections 0.5 um focal steps apart of a field of nuclei. (Sections read from bottom left corner, right to left, ending at the top right corner.) FISH data from P1 probe 09-93 (far left) and from histone probe (middle-left), were simultaneously visualized for the same set of nuclei together with lamin immunofluorescence (middle-right) and DAPI chromatin staining (far right).

to be the paired and unpaired homologous loci respectively. A site was defined as paired if only one signal at twice the intensity of the unpaired locus was seen or if the distance between two signals was less than the signal diameter. By counting the number of nuclei with paired FISH signals, a pairing frequency for each of the probes was determined for embryos at different timepoints of development. The cumulative result of all the probes is shown in Figure 2, where the pairing frequencies for the different probes for each of the selected times of Drosophila development were plotted and fitted with a surface grid map to better clarify the pairing behavior over the chromosome arm .

Figure 2 illustrates that all sites eventually pair during embryonic development but the timing of the initiation of pairing is specific to each individual locus. Between 6 and 13 hours of development, all sites attain pairing levels of > 60%, much greater than the background level of pairing (~ 10%) seen early in development at cycle 13 for many of the sites. This increase in pairing levels continues into the larval stage (wing discs) where > 95% of the nuclei contain paired loci. By examining when pairing initiates for the individual loci, we found a variation in the onset of pairing for different sites on the chromosome. Of the 11 loci examined, the histone locus was observed to pair first (61% paired at cycle 13), followed by the Responder (Rsp) locus (85% at cycle 14). In contrast, significant levels of pairing for other sites were often only seen after 6 hours of development indicating that the onset of pairing occurred later for these sites.

We looked for general trends in pairing over the whole chromosome arm (Figure 2). Previously, it has been proposed that pairing might occur through a zippering process originating at one site which would then spreading processively down the chromosome arm (Hiraoka, 1993; Lewis, 1954;.Smolik-Utlaut and Gelbart, 1987) If this were true, sites closer to the initiation point should exhibit higher levels of pairing than those farther away with pairing levels falling off with increasing distance from the origin. However, such a spreading phenomenom is inconsistent with our observation that the histone and Rsp loci both show higher levels of pairing than the intervening AATAG locus. Another possibility

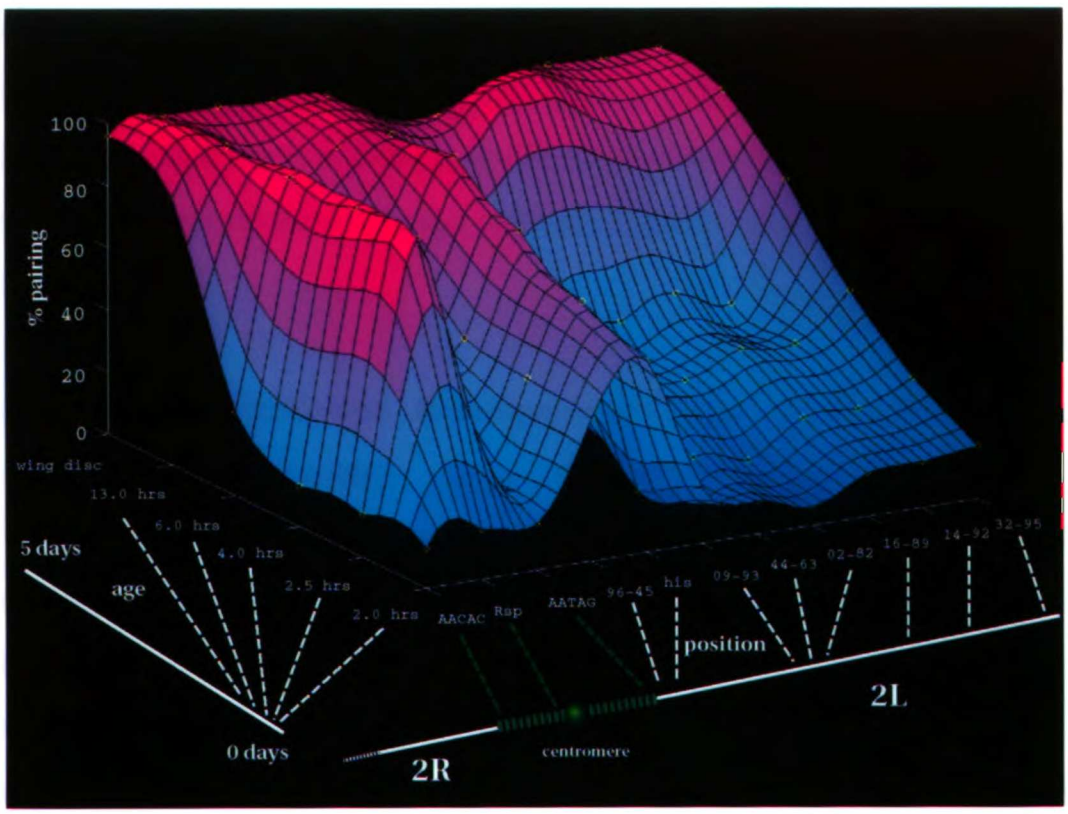

Figure 1.2 Site-specific pattern of homologous pairing for chromosome arm 2L. A surface mesh plot was fit to the measured pairing frequencies (yellow o) to depict general trends in pairing. The height and color of the surface serve to indicated the level of pairing. High pairing frequencies are coded by increasing shades of pink whereas low frequencies are represented by deepening colors of blue. Embryonic age and probe positions were spaced at equal intervals along their respective axes. Below the position axis, a probes's relative location is indicated by dashed lines to a representation of chromosome 2. Embryonic age is mapped to a time line drawn below the age axis.

for the early attainment of high levels of pairing for some sites may be that repetitive loci have some preferential pairing ability because of the greater probability that a single repeat would find a matching site. Both the histone and Rsp locus, the two sites that pair the earliest, consist of several repeated sequences (Lifton et al.,1977; Lohe et al.,1993). However, examination of other repetitve probes such as the satellite sequences AATAG and AACAC, both which show background levels of pairing at a time when both histone and Rsp show high levels of pairing, provide the necessary evidence that the number of repeats in a locus is not the dominant contributing factor for the early onset of homologous pairing.

Cells Following Different Developmental Paths Show No Significant Variation in Pairing Levels

In later stages of embryogenesis, the initially homogeneous cell population divides into diverse cell groups, each following different developmental paths. Hence, the possibility existed that pairing levels would vary between each subpopulation of nuclei. We first tested whether any difference could be observed in pairing levels between nuclei destined for germline and somatic lineages. Starting at cycle 9, cells fated to form the germline (pole cells) separate from the main body of nuclei. These pole cells begin protein synthesis early and divide two more times on their own schedule. Comparison of the pairing levels from pole cell nuclei (53%, n=19) and the main body of nuclei (60%, n=44) for the histone locus obtained from the same cycle 14 embryo did not reveal a significant variation in pairing frequency between the two types of nuclei. In fact, the observed variation fell within the normal range found between separate internal groups of synchronized blastoderm nuclei. For instance, when four randomly chosen regions of nuclei from the same early cycle 14 embryo were examined for their levels of pairing, pairing frequencies of 39% (n=100), 36% (n=117), 46% (n=118), and 40% (n=107) were observed. This shows that a 10% range in pairing levels is within the normal fluctuation

expected for measurements between synchronized populations. Similarly, no large differences were found in the pairing frequencies of the P1 09-93 locus between nuclei within the ectoderm (25%, n=44) and mesoderm (27%, n=26) germ layers in a 6 hour AED embryo. This was particularly surprising since the size and morphology of the nuclei differed greatly between the two layers; ectoderm nuclei are columnar with an average volume of 43 μm^3 whereas the mesoderm nuclei are squamous with an average volume of 69 μm^3, a 60% increase in volume over the ectoderm nuclei. Therefore, at least in these cases, pairing was not affected by changes related to cell differentiation.

Pairing Does Not Depend on Targeting Loci to Special Regions within the Nucleus

We then wished to determine whether the position of a site in the nucleus has any influence on pairing. For example, there might be specific territories in the nucleus, such as near or on the nuclear envelope, where pairing preferentially takes place. It has recently been shown in Drosophila embryos that different loci reproducibly occupy different discrete regions within the nucleus (Marshall et al., 1996). Moreover, a set of loci have been identified that associate specifically with the nuclear envelope, while other loci are localized to a distinct internal subregion. Furthermore, theoretical considerations of how pairing could be optimized suggest that by limiting homology search over the nuclear envelope, a reduction in the search space from 3-D to 2-D could be obtained (Loidl and Langer, 1993; Dorninger et al., 1995). This often has been proposed as the means by which telomeres pair (Loidl, 1990 and references therein). In such a case, we would expect that sites closer to the nuclear envelope should pair more frequently than sites that are far from the nuclear periphery. Therefore, measurements were made to compare a site's distance from the nuclear envelope as well as evaluating its radial and vertical (Rabl) locations in order to look for potential differences between paired and unpaired loci (Table 1). Table 1 shows the average radial and vertical positions of sites measured from cycle 14

Table 1.1 Comparison of probe position in the nucleus for paired and unpaired sites. Average radial positions, vertical (Rabl) positions and average distance from the nuclear envelope were measured for all the sites to determine whether any differences existed between paired and unpaired loci. Measurements were taken from cycle 14 nuclei, 7 to 9 microns in length. Probe order is listed from centromere proximal to distal.

Probe	No. of nuclei	Radial Position (+/- SD) (μm)		Vertical Position (+/- SD) (μm)		Distance to Nuclear Envelope (+/- SD) (μm)	
		paired	unpaired	paired	unpaired	paired	unpaired
AACAC	46	1.38 ± 0.61	1.50 ± 0.48	3.06 ± 1.00	3.55 ± 0.54	0.62 ± 0.56	0.47 ± 0.59
Rsp	29	1.41 ± 0.83	1.33 ± 0.54	1.00 ± 0.77	1.36 ± 0.63	1.39 ± 1.02	1.80 ± 1.95
AATAG	61	0.83 ± 0.40	1.22 ± 0.61	2.96 ± 0.46	2.84 ± 0.92	0.99 ± 0.38	0.79 ± 0.90
96-45	53	1.06 ± 0.44	1.17 ± 0.51	3.18 ± 0.63	3.15 ± 0.82	1.42 ± 0.59	1.25 ± 1.45
histone	100	0.95 ± 0.32	0.79 ± 0.34	0.53 ± 0.42	0.45 ± 0.31	1.60 ± 0.48	1.4 0± 0.48
09-93	38	1.72 ± 0.16	1.52 ± 0.61	0.18 ± 0.21	0.00 ± 0.65	0.51 ± 0.31	0.71 ± 1.0
44-93	49	1.12 ± 0.63	1.57 ± 0.53	0.00 ± 0.47	0.57 ± 0.84	1.30 ± 1.02	0.85 ± 1.10
02-82	41	2.11 ± 0.73	1.54 ± 0.62	0.24 ± 0.52	-0.31 ± 1.15	0.59 ± 0.62	0.87 ± 1.11
16-89	109	1.57 ± 0.56	1.70 ± 0.59	-1.21 ± 2.72	-1.20 ± 2.66	1.01 ± 0.72	0.83 ± 1.08
14-92	85	1.76 ± 0.76	1.92 ± 0.64	-1.53 ± 3.40	-1.67 ± 3.54	0.83 ± 0.91	0.70 ± 1.03
32-95	47	1.20 ± 0.46	1.11 ± 0.54	-1.22 ± 2.51	-1.11 ± 2.31	0.28 ± 0.37	0.34 ± 0.64

embryos together with the average distance from the nuclear envelope, calculated separately for paired and unpaired sites. Using Welch's t-test, the difference between the proximity of a locus to the nuclear envelope for paired and unpaired states was determined to be not significant, even at the 0.01 significance level. We then tested whether pairing is restricted to particular domains or territories within the nucleus. To explore this question, we used cycle 14 nuclei which are arranged in a monolayer on the surface of the embryo thus fixing the orientation of the nuclei so that radial and vertical distributions of a site can be measured. Based on the data from Table 1, no discernable difference in spatial localization for the paired and unpaired sites for either radial or vertical positioning were found at the 0.01 significance level, using the same statistical test to compare distance from the nuclear envelope. The results did show that most sites, paired or unpaired, were contained in a confined spatial distribution imposed by the Rabl orientation as had been previously reported (Marshall et al.,1995). For each individual site, a radial confinement was also seen, but varied in extent between the different sites. We therefore conclude that although sites are spatially confined to a specified volume or domain in the nucleus, sites are not specially targeted to a particular nuclear territory in order to be paired.

Progression in Cycle 14 Interphase Determined by Changes in Nuclear Length

In order to analytically test models of pairing, quantitative measures of the pairing rate must be determined. However, because FISH must be carried out on fixed organisms, it is usually considered impossible to measure rates using FISH to monitor the homologous sites. This is a general problem that arises whenever microscopy with fixed samples is used to study dynamic processes. Although overall developmental time courses can be determined and are very useful to study trends in pairing over large chromosomal regions, this approach does not provide a quantitative measure of the rate of pairing within a given stage. So to circumvent the usual limitations preventing measurement of rates using FISH,

we have developed a strategy to accurately gauge elasped time in cycle 14 interphase by measuring changes in nuclear morphology for use in developing time courses for pairing during this stage.

The first step required exploring whether such a functional relationship actually existed for a easily measurable feature of nuclear morphology. Changes in nuclear dimensions were tracked by injecting fluorescent dextrans into living embryos and taking 3-D data sets of the nuclei as they progressed through the cell cycle, starting from early cycle 13 through 60 minutes of cycle 14 interphase (Figure 3A). This use of fluorescent dextrans had been employed previously in the live analysis of nuclear embryo breakdown and reformation in Drosophila embryos and had been shown not to disrupt the timing of the nuclear divisions (Kalpin et al.,1994). During interphase, the high molecular weight (40,000 MW) dextrans are excluded by the nuclear membrane so that nuclei image as dark holes surrounded by bright fluorescent background (Figure 3B-C). However, when the nuclei enter mitosis, the nuclear envelope breaks down allowing the dextran to enter where it had been previously excluded, so only an even background of fluorescence is seen (see Figure 3B, cyc 13 t=17.5 min). The start of a cycle is marked by the reappearance of the nuclei as dark holes (Figure 3B, cyc14 t=0.0 min). When nuclear length was measured for each timepoint from the volume of each nucleus (Figure 3C), it was found that nuclear length increases monotonically with time in interphase of cycle 14 (Figure 3D). A similar behaviour is observed for both nuclear volume and diameter as seen by DIC microscopy (Foe and Alberts, 1985). By using a least squares fit to the plotted data, a quadratic equation was found relating nuclear elongation to elasped time in cycle 14 interphase (Figure 3D). This equation allows the conversion of nuclear height, which is readily measured from lamin-stained, in situ hybridzed embryos into a measure of time in cycle 14 interphase providing a means by which to obtain the kinetics of pairing at that stage.

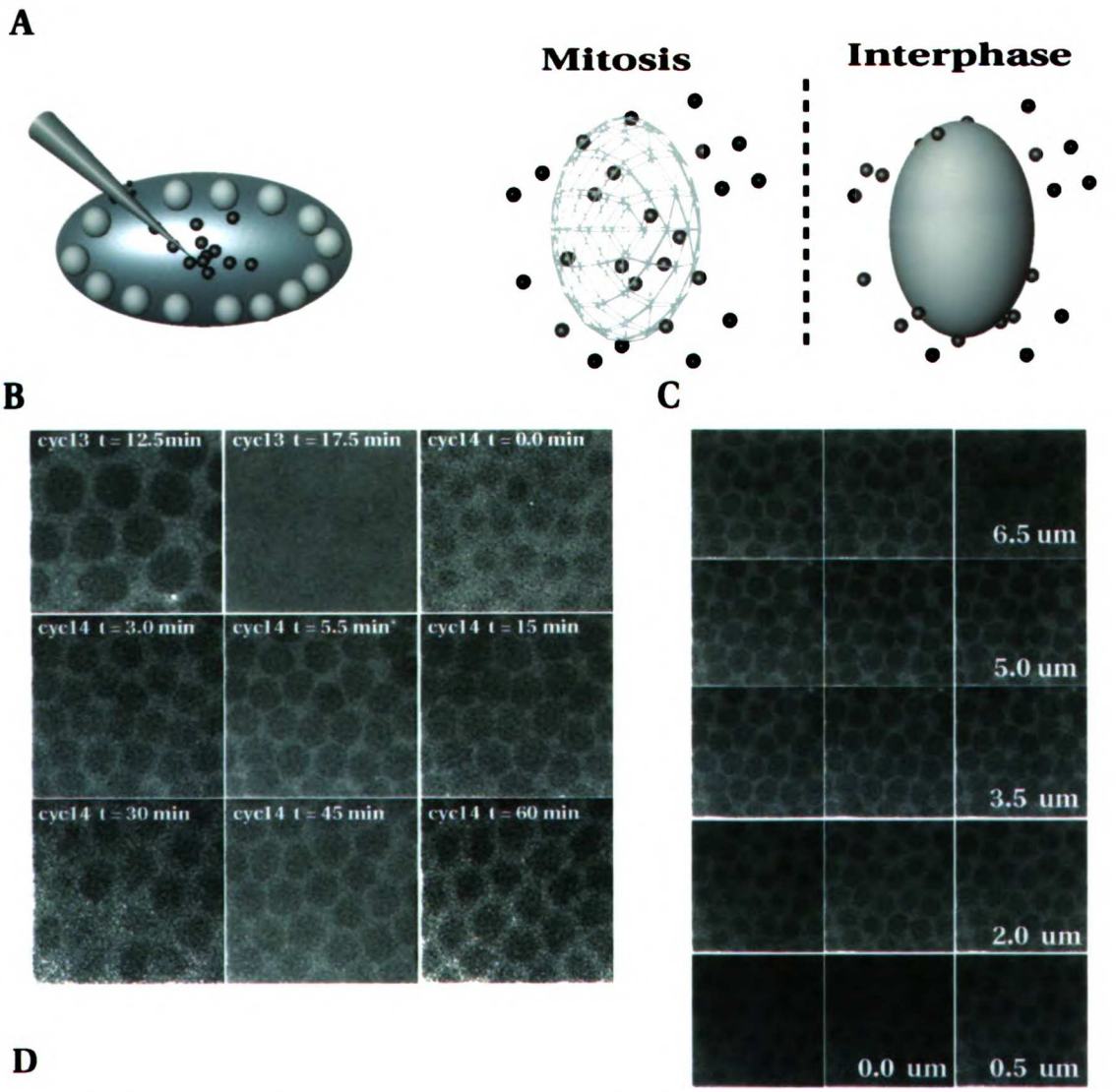
A
Mitosis
Interphase
B
cycl3 t = 12.5min
cycl3 t = 17.5 min
cycl4 t = 0.0 min
cycl4 t = 3.0 min
cycl4 t = 5.5 min
cycl4 t = 15 min
cycl4 t = 30 min
cycl4 t = 45 min
cycl4 t = 60 min
C
6.5 um
5.0 um
3.5 um
2.0 um
0.0 um
0.5 um
D
average nuclear length (um)
20
15
10
5
0
0
10
20
30
40
50
−0.0044t2 + 0.4371t + (4.0754−ht) = 0

Figure 3. Nuclear Elongation as a Gauge for Elasped Time in Cycle 14 Interphase

(A) Procedure for live analysis of nuclear volume using fluorescent-labeled dextrans. Fluorescent-labeled dextran (40,000 MW) is injected into the lumen of the embryo. At interphase, the dextran is excluded from the nucleus but during mitosis, the dextran is able enter into the nuclear region due to NE breakdown.

(B) Time series recording morphological changes in the embryonic nucleus. Single optical sections from 3-D data sets of nuclei as imaged by exclusion of the FITC-labeled dextran. Both the cell cycle stage and elasped time in each stage is marked. Entry into mitosis is observed by the appearance of an even background of fluorescence (see cycle 13, t=17.5 min) brought upon by the NE breakdown. The start of cycle 14 (cycle 14, t=0.0) is set at the first reappearance of excluded nuclear volumes.

(C) Representative 3-D data set of nuclei at cycle 14 t=5.5 min showing that nuclear length can be easily determined from the excluded volume images.

(D) Plot of nuclear length against elasped time in cycle 14 interphase showing a monotonic increase in average nuclear length with increasing time. The quadratic equation was determined by a least squares fit to the plotted data. Such an equation allows the direct conversion from measurements of nuclear height from FISH prepared embryos into elasped time.

Time Profiles for Histone Pairing

The histone locus seemed the best candidate to focus our analysis of a pairing mechanism. Besides having a sharp increase in the level of pairing at cycle 14, the histone locus pairs early (Figure 2), lessening the probability that the pairing of neighboring sites would complicate the analysis through tethering effect. By using the relation determined in Figure 3D for nuclear length together with data obtained from the FISH signals, time profiles for the frequency of pairing as well as for temporal changes in distances between unpaired loci (inter-homolog distances) were generated to characterize pairing of the histone locus (Figure 4). Surprisingly, we found that the pairing of histone locus was relatively rapid with the majority of the pairing (80%) completed in the first 20 minutes of cycle 14 interphase (Figure 4A). At the same time, examination of the time profile of average inter-homolog distances (Figure 4B) showed that as time increased, the average distance between unpaired loci also increased.

Distinguishing between Constrained Random Walk and Directed Motion Models for Pairing.

Having demonstrated two characteristics of how pairing developed for the histone locus in cycle 14, we next wanted to test if the observed behavior of the histone locus conforms to any of the proposed mechanisms for pairing. Two models that might account for how homologous sites become paired are either a directed motion model or random walk model for pairing (Figure 5). In a simple directed motion model, homologous sites would be pulled together at some constant velocity. This type of motion could arise if interhomolog connections were already in place to drive homologs closer together by some type of a contractile force (Holliday, 1968; Maguire, 1983a; Smithies and Powers, 1986). Alternatively, if the homologs were already tethered together at some point, chromosome condensation could potentially bring homologous sites together (Kleckner et al.,1991). In contrast, for motion to arise from a random walk, each step taken must be independent

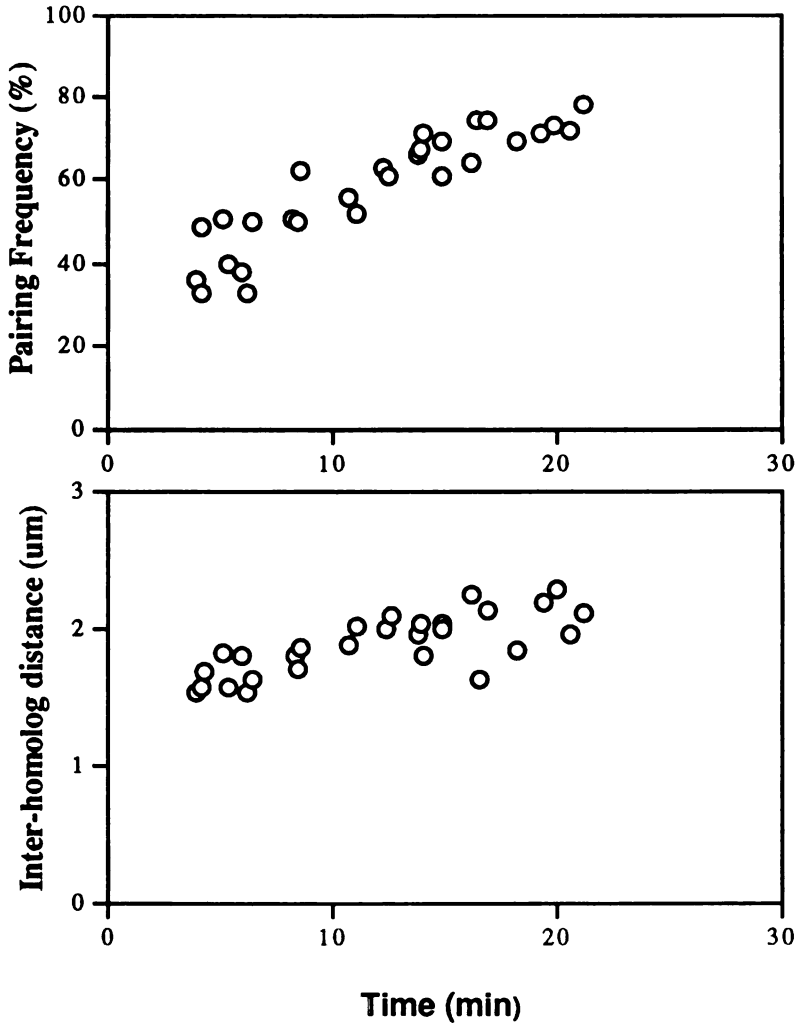

Figure 1.4 Time Profiles of Histone Pairing

(A) Pairing frequency was measured from FISH signals to the histone locus in cycle 14 embryos and plotted as a function of elasped time in interphase as measured by length of the nucleus. A substantial amount of pairing, starting from ~ 20% and rising to ~80%, is completed within the first 20 minutes of cycle 14 interphase.

(B) Average interhomolog distance between unpaired histone loci was plotted as a function of elapsed time in interphase. The average distance between unpaired histone loci at the beginning of interphase is approximately 1.2 mm apart and gradually increases to > 2 mm as interphase progresses.

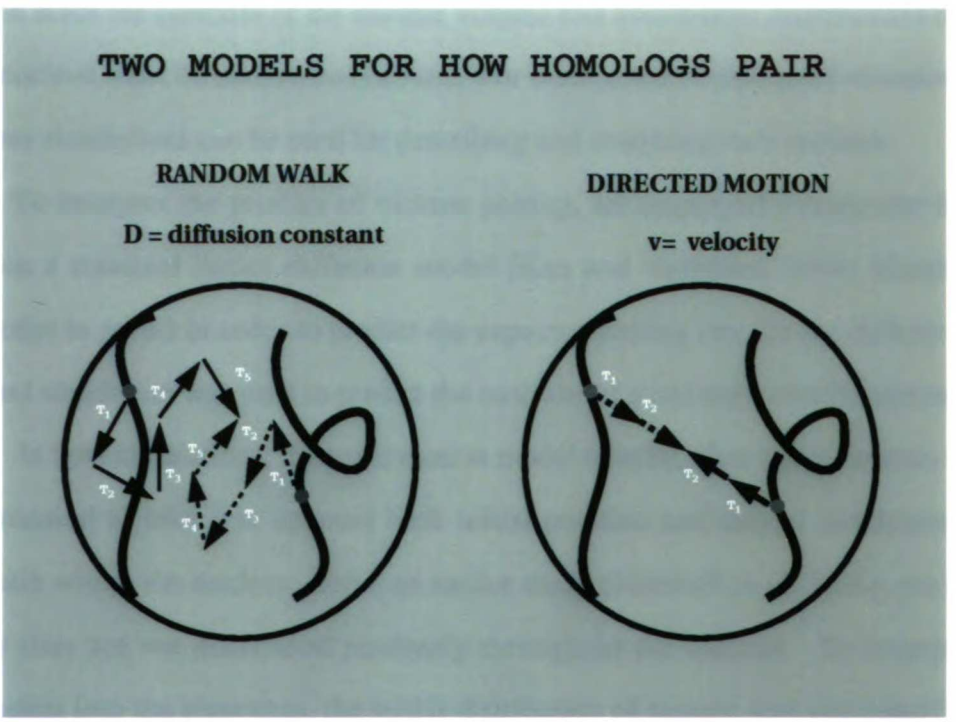

Figure 1.5 Two potential models for homolog pairing.
In the random walk model, the movement of a locus can be separated into units steps that are independent from the previous step, random in direction, and unrelated to the movements of the homologous locus. The diffusion coefficient, D, reflects how fast the random walk is occuring. In the nucleus, chromatin domains and the nuclear boundary would restrict movement from being completely random, so a constrained rather than pure random walk would be expected. In contrast, for the directed motion model, each pair of homologous loci take a unit step in a direction pointed towards the other locus. Here, a velocity constant is used to represent how fast motion is occurring.

from the previous step and random in direction (Crank, 1956). This results in the relation that the mean squared displacement in 3-D be given by the equation $\langle r^2 \rangle = 6Dt$, where t is time and D is the diffusion coefficient which reflects how fast the random walk is occurring. Inside a nucleus, equations describing random walk motion become more complex since the confines of the nuclear volume and nonrandom distributions of the sites in the nucleus must be taken into account. For these more complicated situations, simple computer simulations can be used for describing and analyzing such motions.

To interpret the profiles of histone pairing, we employed a computer simulation based on a standard lattice diffusion model (Kao and Verkman, 1994; Marshall et al., manuscript in prep.) in order to predict the expected pairing rate for the diffusive motion. A second simulation was used to predict the outcome of a constant velocity directed motion model. In both simulations, the basic motion model whether directed or random walk, was supplemented to take into account both initial position and spatial confinement of the chromatin within the nucleus. From an earlier study (Marshall et al, 1996), we know that histone sites are not distributed randomly throughout the nucleus. To incorporate this information into the algorithm, the initial distribution of histone loci was specified by the average radial (r_o) and vertical positions (z_o) and their respective standard deviations (σ_{ro} and σ_{zo}) measured from nuclei representing the earliest time point in interphase (Figure 6). Spatial confinement was modeled by limiting motion within a cylindrical volume as given by the radial boundary (tether) and vertical boundary (ht). These values are obtained by measuring respectively, the average standard deviations, σ_r and σ_z, for the radial and vertical positions of the loci over the duration of the pairing (Figure 6), which in turn is a measure of the potential range of radial and vertical position (see Experimental Proceedures).

The result of using such simulations to characterize the behavior of the pairing of the histone loci is given in Figure 7 for changes in pairing frequency and interhomolog distances, both for the case of diffusional motion and directed motion at constant velocity.

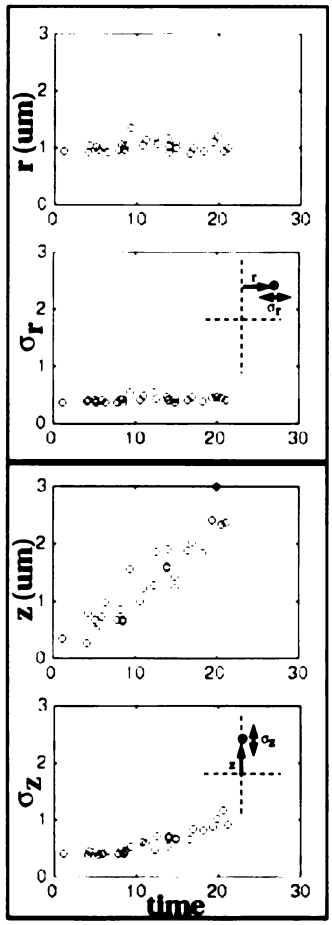

Figure 1.6 Characterization of temporal changes in the distribution of histone loci in cycle 14 interphase nuclei.
The top two panels report the average radial position and its variance for the histone locus used to characterize histone's radial distribution in cycle 14 interphase. Note that the average radial position and the variance remain relatively constant throughout the observed portion of cycle 14 interphase. The bottom two panels report the average vertical position and its variance for the histone locus. Here, the average vertical position increases but the variance remains relatively constant. The increasing average vertical position reflects the fact that the nuclei are lengthening. However since the variance remains relatively constant, this indicates that the volume over which the loci occupy remain relatively the same and that no significant spreading effect is caused by the upward movement of the locus. In the simulation, the normal distributions are generated based on variances measured at the earliest timepoints.

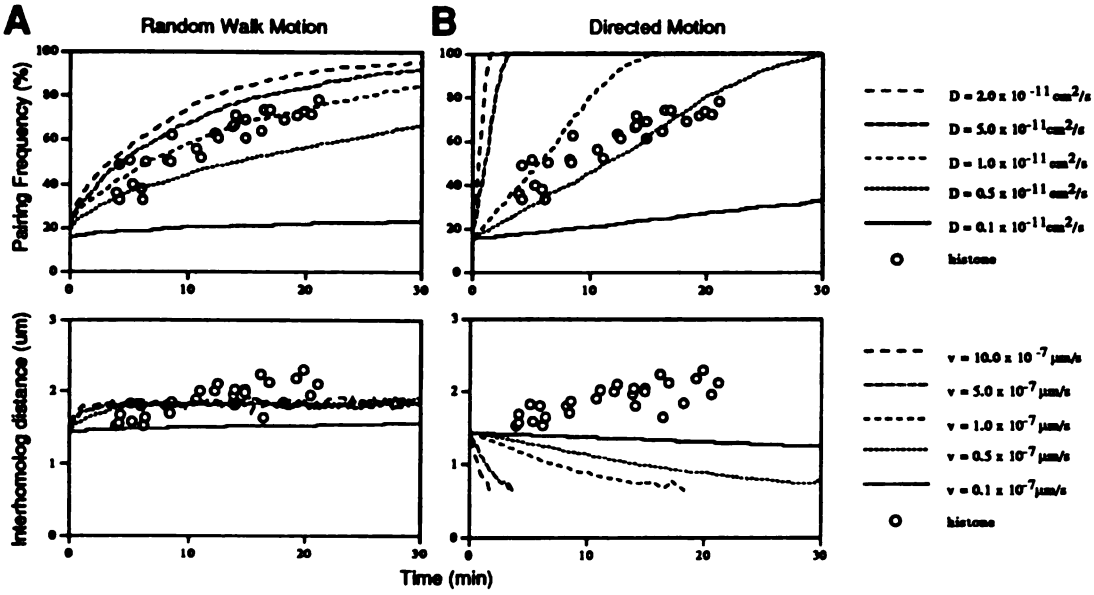

Figure 1.7 Comparison of pairing kinetics of the histone locus as predicted by random walk and directed motion models plotted against experimentally measured values.
(A) Random Walk Motion: (Top Panel) Plots of the pairing frequency as a function of elasped time in cycle 14 were generated from simulations based on the random walk model of pairing for several values of the diffusion constant and are represented by different line patterns. The empty circles are the actual experimental values for the pairing frequency of the histone locus replotted from Figure 1.4. (Bottom Panel) Plots of the inter-homolog distances generated from the simulation using the same D values as above. The empty circles here are the experimentally measured distances.
(B) Directed Motion: Same types of plots as in (A) except this time they were generated using the directed motion model for several values of the velocity. Again, the appropriate experimental data was plotted as empty circles for comparison.

Profiles for both the frequency of pairing and the interhomolog distance as a function of time have been plotted for several values of the diffusion coefficient and velocity (Figure 7A and 7B). As might be expected, the time profiles for the frequency of pairing show a more gradual approach towards the completion of pairing in the random walk model (top panel, Figure 7A) as compared to the faster approach predicted by the model using directed motion (top panel, Figure 7B). Similarly, for time profiles expressing the changes in inter-homolog distance, we also see qualitatively distinct behavior for the different models. In the case of random walk, as sites that are near each other pair and are no longer included in the calculation of average distance between unpaired homologous sites, we intuitively expect that the average inter-homolog distance should shift to greater distances with time, while also showing the distances leveling off after longer time periods as a result of the imposed spatial confinement. The bottom panel of Figure 7A clearly demonstrates that this indeed is the case for this simulation. In contrast, we would expect an entirely different behavior for the inter-homolog distances based a directed motion model. Here as shown in the bottom panel of Figure 7B, the average distnace between between homologous sites should monotonically decrease, since by this model, sites are being pulled together at a constant velocity.

We then compared the actual measured profiles of histone pairing with those generated by the simulations. We only found good correlation in the pairing frequency plot between the experimental data and the simulations when motion is predicted to occur by a constrained random walk with a diffusion coefficient of $D = 1.0 \times 10^{-11}$ cm^2/s (top panel, Figure 7A). In contrast, the shape of the pairing frequency plots for the directed motion model did not fit the experimental data for any value of velocity (top panel, Figure 7B). When comparing actual and simulated inter-homolog distances (bottom panel, Figure 7A), the experimentally derived values again agreed only in the case when motion is modeled as a random walk where both the simulation and actual data show an increasing distance between unpaired loci with elasped time. In contrast, when the measured profiles of

histone pairing were compared with those obtained from the simulations based on the directed motion model (Figure 7B), little correspondence could be detected. This is particularly evident in the plots of inter-homolog distance (bottom panel, Figure 7B) where the simulations predict a decrease in the distance whereas the actual data shows a distinct increase. From these comparisons, we thus conclude that the pairing behaviour of the histone locus is consistent with a random walk model for chromatin motion. Further confirmation for this model is provided by the fact that the diffusion coefficient, $D = 1.0 \times 10^{-11}$ cm^2/s that we obtained from our pairing analysis is in excellent agreement with $D = 1.25 \times 10^{-11}$ cm^2/s obtained in a separate study directly measuring chromatin motion in Drosophila embryonic nuclei (Marshall et al., 1996). Combined, these results provide strong evidence that the pairing of histone loci occurs by constrained random walk motion.

Perturbation of Pairing as a Consequence of Chromosome Rearrangement

The lt^{x13} strain (Wakimoto and Hearn, 1990) contains a reciprocal translocation between the centromereic heterochromatin on chromosome arm 2L and a subtelomeric site on arm 3R that moves the entire histone locus near the end of 3R (Figure 8A). Surprisingly, in strains homozygous for the lt^{x13} chromosome translocation, pairing levels for the histone locus during cycle 14 was found to be ~ 30% on average compared to ~70% for wild type (Hiraoka et al., 1993). In this strain, the average vertical position of the histone locus measured at the beginning of cycle 14 is shifted from the center of the nucleus (as seen in wild type strains) to a position ~1.5 um lower. Why this positional change would result in much lower levels of histone pairing was never clear given that both loci are shifted equally in this homozygous translocation. Could it be that the intrinsic pairing ability of the histone locus is somehow affected by this translocation? This seemed unlikely to us given the independence of the histone pairing from neighboring sites as shown earlier in this paper and the fact that high levels of pairing (83%) are again seen at the 13 hrs AED timepoint. In the Hiraoka study, a plot of the distribution of of histone loci

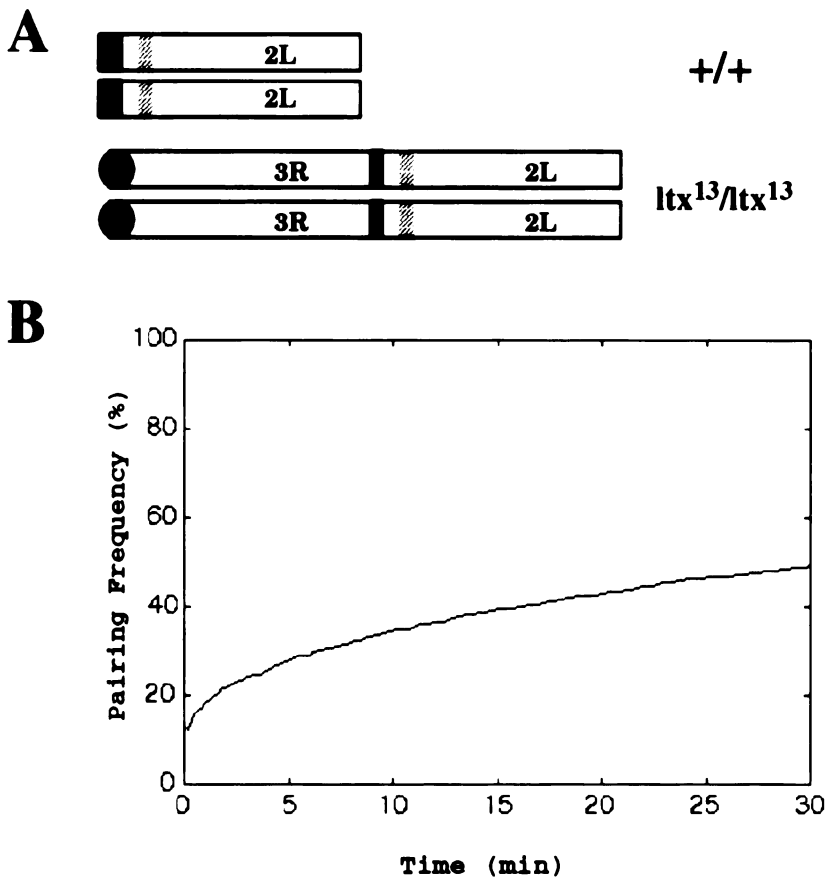

Figure 1.8 Perturbation of pairing by rearrangements.
(A) Diagram illustrating chromosome arm 2L in a homozygous wild type strain and in a homozygous ltx^{13} strain where 2L is translocated to the end of 3R. The dark filled areas indicate heterochromatic regions. The cross-hatched areas indicate the approximate location of the histone locus.
(B) Plot of the simulated pairing frequency for the histone locus in a ltx^{13} strain as a function of elasped time in cycle 14. Plots were generated based on actual experimental data of the distribution of the histone locus using $D=1.0 \times 10^{-11}$ cm^2/s as our value for the diffusion coefficient. Note that the pairing frequency is predicted to be much lower for the ltx^{13} strain.

for the wild type and homozygous lt^{x13} strain revealed a slightly wider range in the distribution for the lt^{x13} strain. Given that histone pairing occurs by diffusion, the fact that histone loci now start farther apart on average may explain why, granted the same amount of time, pairing levels for the lt^{x13} strain are lower. To test this possibility, we measured the initial variances in the radial and vertical positions for the lt^{x13} ($\sigma_{ro} = 1.1$ and $\sigma_{zo} = 1.7$; compare with wild type, $\sigma_{ro} = 0.4$ and $\sigma_{zo} = 0.4$) and used simulations to predict the pairing behavior. The resulting profile (Figure 8B) shows that given this initial distribution of histone loci, a lowered pairing frequency is indeed expected. Moreover, similar levels of pairing were observed here (for t=15 min, pairing level = 40% for lt^{x13}; compare this to 70% for wild type (see Figure 4A)) as were seen in the Hiraoka study (~30% for lt^{x13} and ~70% for wild type). The slight discrepancy between the pairing levels for lt^{x13} from the different studies, 40% vs 30%, is most likely attributed to the fact that, in the Hiraoka study, no attempts were made to distinguish between embryos at different elasped times in cycle 14. From these results, we conclude that the inherent pairing ability of histone is not affected by the translocation, but rather, the wider distribution (i.e. larger variance) imposed by histone's new location is responsible for the lower frequency of pairing seen in these strains. This result, moreover, dramatically confirms the predictive power of the constrained random walk model, further increasing our confidence in its validity.

Disruption of Pairing By Mitosis

To determine whether the pairing interactions are maintained throughout the cell cycle, we examined the level of histone pairing during the mitotic stages. During mitosis, several forces act upon chromosomes eventually resulting in chromosome separation to opposite poles (reviewed in Gorbsky,1992). These forces include chromosome condensation, forces involved in metaphase congression and forces contributing to anaphase separation, all of which could potentially disrupt any homologous pairing associations formed in the preceding interphase. Evidence that pairing is indeed disrupted

during mitosis is indicated here by the observation of a decrease in pairing levels for the histone locus in the transition between cycle 13 and cycle 14 interphase. At cycle 13 interphase, the average pairing frequency for this locus is 62% (Figure 2) but at the beginning of cycle 14 interphase, the pairing level is down to 22% (Figure 4A). The reduction of the pairing level to 22% suggests that homologous pairing is completely dissociated during passage through mitosis. To further narrow down the timing of this disruption, we examined the pairing levels for the histone locus at selected stages of cycle 13 mitosis. During metaphase of cycle 13, when the chromosomes are maximally condensed, the association level for the histone locus is 63% (Figure 9A). Since these values are equivalent to what is found during cycle 13 interphase, disruption of the pairing association has not occurred up to this point. Note that no gain in the pairing levels is seen either, indicating that no significant pairing is occuring during passage through the prophase (50%) and metaphase stages. Next, we examined nuclei undergoing anaphase and here a dramatic disruption in the pairing was observed (Figure 9B). Anaphase figures were either found with 4 (72%) , 3 (18%), or 2 (10%) FISH signals for the histone locus. Up to 4 signals are seen in anaphase due to sister chromatid separation unlike the one or two signals found during metaphase when sister chromatids are still associated. Because each anaphase figure eventually results in two telophase nuclei, we counted each set of sister chromosomes as a separate nucleus in our calculation of pairing frequency in order to take into account any anaphase figures with 3 FISH signals (one paired, one unpaired). This results in a pairing frequency of 19% for the histone locus at anaphase. We conclude that it is during anaphase that pairing interactions are dissociated thus explaining the low levels of pairing frequency found at the beginning of cycle 14 interphase.

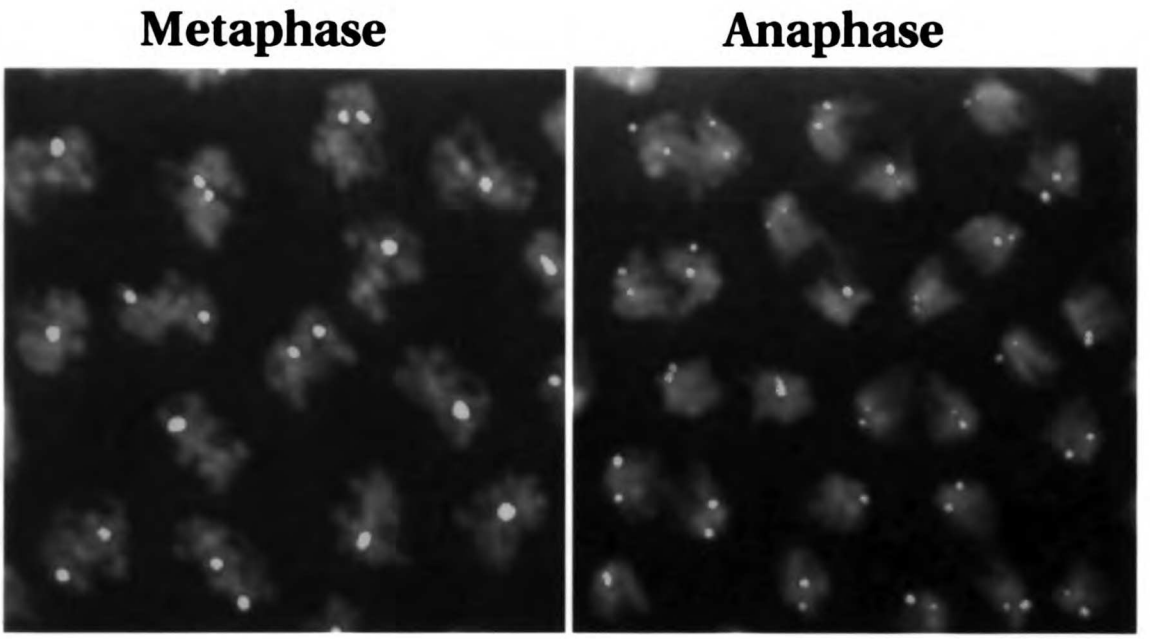

Figure 1.9 Perturbation of pairing occurs during anaphase.
(A) A volume rendered image of metphase chromosomes in several nuclei from a cycle 13 embryo overlayed with FISH signals from the histone probe. Over half the nuclei show a single FISH signal indicating that pairing of the histone locus is maintained.
(B) A volume rendered image of anaphase figures overlayed with the FISH signals from the histone probe. Here, four FISH signals are seen showing that pairing has been disrupted during this stage.

Discussion

Mechanism For Homolog Pairing

Greatly differing views exist for the mechanism whereby chromosomes find their homologous partners. On one hand, there are several models which propose active movements on the part of chromosomes to bring homologous sites together. Holliday (1968) postulated early on that one way for homologs to be drawn together is through the contraction of fibrillar connectors extending between specific DNA sequences on homologous chromosomes. A similar proposal was offered by Maguire (1983a) based on observations of homologous alignment at a distance (Maguire 1983b) and on reports of the existence of premeiotic and early meiotic intranuclear bundles of microfilaments in microsporocytes (Bennett et al, (1979)). More recently, Kleckner et al. (1991) modifying a proposal by Smithies and Powers (1986), alternatively favored the view that after the initial formation of unstable DNA-DNA interactions through chance encounters, chromosome condensation may be involved in further driving homologs closer together. A common feature in all of the aforementioned models is that at some point homologous regions are directed towards each other. This is in contrast to the opposing view that random contacts of homologous sequences, brought about by diffusion of chromatin, is the primary mode in establishing homologous pairing (e.g. Brown and Stack, 1968).

In this study, we provide the first demonstration of a means by which pairing can take place. By measuring the actual kinetics of pairing and using simulations of pairing based on a directed and random walk motion models, we show that pairing of the histone locus during Drosophila embryonic development is consistent with a mechanism that relies on finding a homologous locus through diffusive motion of the chromatin.

The occurrence of random walk motion of chromatin during interphase has been confirmed in several organisms. Recently, Marshall et al. (manuscript in preparation) directly measured chromatin motion in live interphase nuclei in Drosophila, maize and

budding yeast and found in all cases that the observed loci moved by random walk motion. Although the 359 bp satellite repeat on chromosome X and not the histone locus was analyzed in the case of Drosophila, the diffusion coefficient obtained for this locus corresponded well with the value acquired by our analysis of the histone pairing profile. The fact that the diffusion coefficient obtained from the histone pairing profile agrees with the value obtained in the independent study of chromatin motion in Drosophila gives further support that pairing of the histone locus does indeed occur via random walk motion of chromatin.

While this study strongly suggests a diffusion driven random walk mechanism for homolog pairing, there may be other mechanisms that pair other sites. There still could be a combination of mechanisms including condensation and/or active processes which also play important roles in achieving full homologous association. Active movement of telomere-led chromosome motions that occur preceding meiosis.in fission yeast (Chikaskige et al., 1994) may be one example of how active processes may used to create conditions that promote the homology search.

Disruption of Pairing Interactions by Mitosis

Our histone results indicate that pairing interactions begin to form at the start of interphase. During interphase when pairing is in progress, chromosomes are at their most decondensed state which is in agreement with previous suggestions that pairing occurs when chromatin is not greatly compacted (Dawe et al., 1994; Kleckner et al., 1991). During this time, DNA replication and histone gene transcription are also occurring concomitantly (Edgar and O'Farrell, 1990; Edgar and Schubiger, 1986) with no obvious interference to the pairing interactions. Nor is there any disruption due to forces involved in chromosome condensation or metaphase congression as seen by the maintenance in pairing levels up to the metaphase stage. Consequently, we believe that relatively strong interactions are created between the two homologous regions when they contact, which are

only disrupted in mitosis during anaphase. A possible explanation for this disruption at anaphase is that spindle forces that act upon the chromosomes to segregate the sister chromatids to opposite poles somehow exert enough force or create enough agitation to cause dissociation of homologous pairing. However, equally plausible is the idea that the same factors regulating the end of sister chromatid cohesion may also release homologous associations.

The fact that mitosis almost completely disrupts the pairing formed during the previous interphase has bearing on the proposed concept of graduality in the pairing process. It has been suggested that meiotic pairing results from gradually increasing the number of loci that are paired over the course of several cell cycles preceding meiosis (Brown and Stack, 1968). However, if it is true that complete disruption of pairing interactions occur at every mitosis, no significant accumulation of pairing should be obtained from successive cell cycles. Rather, in order for pairing to be established over long stretches of chromatin, it seems that a long interphase or an uninterrupted period during which chromosomes are still decondensed is required, particularly if part or all of the pairing is to occur by random walk motion. The importance of the length of the cell cycle was also stressed by Golic and Golic (1996). In their study, they found that Minute mutations which significantly slow the rate of cell division in imaginal discs could suppress the effects of rearrangements on transvection. A longer period where chromosomes are still decondensed also coincides nicely with observations in several organisms that the duration of premeiotic interphase (Bennett et al., 1973; Williamson et al., 1983) and prophase I (reviewed in Bennett (1977)) are quite lengthy in comparison to their mitotic counterparts.

Reevaluation of the Onset of Pairing for the Histone Locus

The requirement for a sufficiently long interphase period may also explain why in early nuclear divisions of Drosophila embryogenesis the level of pairing of the histone

locus on average is much lower than the level seen at cycle 14 (Hiraoka et al.,1993). The dramatic change in the level of histone pairing at cycle 14 was used to propose that the histone locus had the capability to pair only after the transition to cycle 14. We now believe that it is timing and not competence for pairing that explains the change in pairing levels. We now propose that the pairing capability for the histone locus exist for all cell cycles, but the shorter cell cycle times for early divisions (e.g. cycle 12, 13 min; cycle 13, 17 min, time includes mitosis, (Foe and Alberts, 1983) do not allow enough time to achieve higher levels of pairing. Corroborating evidence is that the cycle 13 pairing frequency of 61% which we measured in this study shows that the histone locus is indeed becoming paired before the transition to cycle 14. One possibility why only a 32% pairing frequency for cycle 13 was seen in the previous work may be that only earlier cycle 13 embryos were examined due to differences in the collection temperature, leading to the impression of a very sharp change in the pairing frequency at the transition between cycle 13 and 14.

What governs the ability for homologous pairing?

The variation in the temporal pattern of pairing onset seen during Drosophila development in this study, raises the question why certain sites attain high levels of pairing very early in development whereas other sites take much longer. This question can be said to relate to the more general issue of what might govern the ability for homologous sites to pair. An answer to this question will not only help us understand how pairing develops so that a whole chromosome is completely aligned but will also help us comprehend observations that in most somatic tissues, except in the case of Dipterans, homologous pairing specifically occurs for some loci but not for others. For a long time, conflicting evidence existed whether somatic pairing, outside what was seen for Dipteran insects, occurred at all (Haaf and Schmid, 1991). However, recent evidence now indicates that somatic pairing does occur in a site specific manner and that the contradictory results obtained previously arose from the fact that such pairing is highly dependent on the

particular tissue being examined and the time frame being studied. For example, using 3-D FISH techniques combined with fluorescence-activated cell sorting, LaSalle and Lalande (1996) found in human lymphocytes that homologous association occurred specifically at the imprinted 15q11-q13 regions only during late S phase of the cell cycle. A related observation was made for the existence of a tissue dependence for somatic pairing in earlier work by Arnoldus et al (1989) showing that homologous association is detected for human chromosome 1 from nuclei taken from cerebellar tissue but not in nuclei from cerebral tissue. Even in Drosophila where somatic homolog pairing is complete in many cases, there is also evidence suggesting inherent differences in pairing ability of different loci in meiosis (McKee et al. (1993); Dernburg et al., 1995) For example, McKee et al. (1993) examining the distribution of autosomal pairing ability in Drosophila males during meiosis by characterizing the pairing and segregation patterns of males carrying various transpositions of regions derived from chromosome 2 into Y, identified a strong pairing site found to contain the histone locus. Other studies focusing instead on the sex chromosomes show that the rDNA locus is a strong pairing site as well (reviewed in McKee (1996). Thus in many organisms, it appears that different sites have different inherent tendencies to homologously pair, but the basis for these differences is currently unknown.

In this paper, we examined and eliminated several possibilities as reasons why certain sites may demonstrate preferential pairing abilities over others. In the two loci that paired the earliest, histone and Rsp, a common feature in both is that each locus consists of several repetitions of their respective sequence. However, examination of other loci with repeated sequences (e.g AACAC) show quite clearly that repetition alone is not sufficient to confer early participation in the pairing process. Furthermore, through contrasting the pairing abilities of euchromatic and heterochromatic sites, no indication was found of a consistent difference in pairing ability thus removing the possibility that this characteristic of the chromatin directly influences the pairing process.

There remain several possible explanations for differences in pairing ability. One suggestion that has been made is that transcriptional activity may also correlate with pairing ability (McKee, 1996) since both the histone and rDNA loci, found to be strong pairing sites during male meiosis are also known to be highly transcribed. It is, however, unclear whether or not the heterochromatic Rsp locus, one of the earliest pairing sites in the embryo, is actually transcribed. The correlation between transcription and pairing is thus far from compelling at least in this case. Another possibility is that differences in pairing could arise from differences in protein binding sites at different loci. If homolog pairing is mediated by chromatin-associated proteins, then differences in the affinity of these proteins for certain regions will be reflected in differences in the propensity of those regions to pair. Thus, the explanation for differences in pairing ability remains an open question requiring further investigation.

The role of nuclear organization in homolog pairing

From our profile of the pairing frequency for the histone locus, we found that pairing can occur at a reasonable timescale, such that, by 20 minutes, 80% of the nuclei contain paired histone loci. It was also evident from monitoring histone pairing in the lt^{x13} strain, for pairing to occur by diffusion based mechanism, requires some limitation in the area over which homologous loci can occupy. Thus we would like to speculate that a key component for homologous pairing is the 3-D architecture of the nucleus. As discussed earlier, it has been shown that a given locus occupies a discrete subregion within the nucleus (Marshall et al, 1996) in the Drosophila embryo. First of all, these nuclei are strongly polarized in a classical "Rabl" configuration, with centromeres at one end of the nucleus, near the surface of the embryo, and telomeres at the other end of the nucleus, near the embryo interior. In fact, not only centromeres and telomeres but all loci are positioned along this axis of polarization. As a result, a given locus is found to occupy a narrow plane in the nucleus, where the position of this plane in the nucleus depends only on how far the

locus is from the centromere on the chromosome. In addition to the confinement on such a plane, there is an additional radial level of confinement, in which distance of a given locus from the nuclear envelope (NE) is relatively constant. In particular, a set of NE associated sites have been identified in the Drosophila embryo, approximatelyt 10-15 sites per chromosome arm, which during interphase are localized near or on the nuclear envelope. Similarly, another set of sites have been identified that are nonrandomly localized to the interior of the nucleus. Sites not associated with the NE or localized to the very interior of the nucleus localize to an intermediate region. The position of any particular locus is thus confined both in the vertical axis (by the Rabl orientation) and the radial axis (by distance to the NE), and thus the locus can only occupy a rather small toroid sub-region in the nucleus. Homology search by any given locus will thus be confined to the small sub-region in which it is localized. We propose that because both homologous copies of such a locus will, in general, occupy the same subregion, homology search will be greatly facilitated. Moreover, time spent exploring non-homologous loci will be greatly reduced, since most non-homologous loci will be confined in separate regions of the nucleus and will never come into contact during the pairing process. Thus, a highly defined nuclear architecture, such as is clearly seen in the Drosophila embryo, can dramatically enhance the rate of homology search. We can carry this hypothesis one step further. Computer simulations in this study indicate that the rate of homology search depends criticaly on both the initial distance between the loci and the size of the region in which the search takes place. Loci with more peripheral localizations will be found within a significantly larger annular region than loci positioned more internally, and thus the homology search should take longer. We thus predict that the sites which pair first will be those which are most internally localized. Interestingly, both histone and Rsp, the first sites to pair on chromosome 2, are nonrandomly internal (Marshall et al., 1996), indeed they are the only such sites known on chromosome 2. A picture is thus emerging in which position within the nucleus, as

specified via the nuclear architecture, plays a critical role in homolog pairing, and could in fact explain why some sites pair much earlier than others.

In spite of clear evidence for a number of functional attributes of homologous pairing in Drosophila and other organisms, a number of issues remain outstanding. Perturbation of homologous pairing by chromosome rearrangements do indeed change pairing, but eventually these rearranged sites do fully pair, thus function is likely not compromised. The functional consequences of pairing are thus unclear. Somatic pairing in the Drosophila embryo nevertheless serves as a useful model system for studying homolog pairing in general, and many lessons learned from this study are likely to apply to meiotic pairing as well.

Experimental Procedures

Drosophila Stocks

Wild-type flies were obtained from an (Oregon-R) stock maintained at UCSF. The lt^{x13} strain (Wakimoto and Hearn, 1990) was provided by B. Wakimoto (University of Washington, Seattle WA). All stocks were maintained at 24°C.

Preparation of DNA probes

Probes were prepared as described in (Hiroaka et al.,1995) for the histone gene clone, in (Dernburg et al, 1996) for the synthetic oligonucleotides (AATAG, AACAC) used to detect heterochromatic repeats and in (Marshall et al., 1995) for the P1 genomic clones. The plasmid containing the 4.8 kb HindIII fragment of Drosophila melangaster histone genes [Lifton, 1977 #6] was kindly donated by G. Karpen (Salk Institute, La Jolla, CA). The Rsp probe was a gift from C.I. Wu (University of Chicago, IL). The P1 clones [Hartl, 1994 #8]32-95 (DS03071), 14-92 (DS01340), 16-89 (DS01529), 2-82 (DS00178), 44-63 (DS0419), 9-93 (DS00436), and 96-45 (DS09165) were obtained from the Berkeley

Drosophila Genome Project. The labeling procedure, used for the histone gene clone, the oligonucleotides and the P1 clones was carried out exactly as described in Marshall et al (1995) and Dernburg et al. (1996) Probe DNA (except for oligos) was first amplified using degenerate oligonucleotide-primed polymerase chain reaction [Telenius, 1992 #9]. 4-base cutting restriction enzymes were then used to digest the DNA before end-labeling with either rhodamine-4-dUTP (FluoroRed, Amersham, Arlington Heights, IL) or digoxigenin-dUTP (histone and oligos only) in a terminal transferase (Ratliff Biochemical, Los Alamos,NM) reaction [Dernburg, 1996 #5]. In some cases, fluorescein-12-dUTP (Renaissance Inc., Boston, MA) was used instead of the other fluorescent labels.

Confidence of FISH Signal

In order to be confident that the FISH spots that we observe actually represent hybridization to the paired or unpaired location of a particular site, probes were selected or tested for unique localization. The heterochromatic sites used in this study were found only on chromosome 2 (ref:Lohe) except for AATAG. Since AATAG satellite sequences are also found on the Y chromosome, a chromosome Y specific probe was used to identify male embryos so not to include them in the study. To ensure that euchromatic probes made from the P1 clones also marked unique sites, neighboring clones 80 kb away were labeled with a different fluorophore and simultaneously observed with the corresponding probe to establish whether similar regions of localization could be found (data not shown). Only probes meeting this criteria were used for the subsequent pairing experiments.

Preparation of Embryos and Wing Discs

To obtain embryos in cycle 13 and early cycle14, embryos were collected for 1.0 hours and aged for 1.83 hours before fixation. For the 4, 6, and 13 hour timepoints, collection was set for one hour with 3.5, 5.5, and 12.5 hour aging periods, respectively, at 24^{o}C. Embryos were then bleach dechorionated, fixed in 3.7% formaldehyde, and

devitellinized as described by [Hiraoka, 1993 #1]. FISH was performed using a method reported in [Dernburg, 1996 #5]. To clearly delineate the nuclear boundaries, anti-Drosophila lamin monoclonal T40 was added and detected using either fluorescein or Cy5-conjugated goat anti-mouse secondary antibodies (Jackson Immunoresearch Laboratories) [Paddy, 1990 #11]. Before imaging, embryos were stained with 0.5 ug/ml DAPI in 50 mM Tris-Cl for 10 min and mounted on # 1.5 coverslips coated with 1% poly-L-lysine to aid in embryo adherence. Most of the buffer was removed and a Vectashield antifade mounting medium (Vector Laboratories, Burlingame, CA) was applied to the embryos before sealing the coverslip to the slide with nailpolish.

Wing discs were dissected from climbing third instar larvae in Robb's saline (Ashburner, 1989). The wing discs were then transferred to a hypotonic 0.7% Na citrate solution for 5-10 minute and then to 45% acetic acid on a 18x18, no. 1.5 siliconized coverslip for 3 minutes. Squashing followed by inverting a slide over the coverslip and applying pressure. The slide was immediately transferred to 100% methanol after popping the coverslip off in liquid nitrogen. Hybridization was performed as described by (Pardue, 1986).

Three Dimensional, Multi-Wavelength, Fluorescence Microscopy

3-D datasets were acquired with a scientific-grade cooled CCD camera (Photometrics, Tucson, AZ) attached to an Olympus inverted fluorescence microscope IMT-2. Action of the shutters, filter combinations, stage movement, and data collection were under the control of the Resolve3D data collection program [Chen, 1996 #15] developed for use on an Indy workstation (Silicon Graphics, Sunnyvale, CA). A 60x 1.4 NA Olympus lens (0.1117x 0.1117 pixel size in the xy-plane) and n=1.5180 immersion oil (Cargille Laboratories, Cedar Grove, NJ) were used to image 512 x 512 pixel fields of 40-130 embryonic nuclei. Early cell cycle stages of the embryos were determined by the number of nuclei in a 512 x 512 pixel image. Each image of a 3-D stack were acquired by

moving the stage in 0.5 um intervals, thus setting the z-axis resolution to be 0.5 um. For every focal position, an image was taken for each of the wavelengths corresponding to the fluorophores used in the experiment. After collection, data stacks were corrected for fluorescence bleaching and deconvolved with experimentally determined point spread functions using a constrained interative deconvolution method (Agard, 1989 #16). The wing disc squashes were collected as a multi-wave 2-D images at a single focal plane.

Analysis of Lamin and FISH Signals

The lamin signal was used to delineate the boundary of each nucleus. An outline of the lamin signal for each focal plane of the nucleus was determined by using a function which creates 2D polygons to represent the outline. Each 2D polygon was created semi-automatically by manually placing a seed point somewhere internal to the lamin; from this point an automatic search for the internal edge of the lamin extending radially outward from the seed point was initiated. A percentage change of intensity relative to the seed point was used to evaluate whether each encountered pixel was at the edge of the lamin signal. The actual outline pixel, selected to be at the middle of the lamin signal, was obtained by extending the location of the pixel to be a fixed distance from the determined edge. All the pixels belonging to a nucleus were obtained by grouping together all 2D polygons with the greatest z-axis overlap. Once a set of outline points belonging to a nucleus was determined, a surface harmonic expansion was used to fit a surface to each nucleus as described in [Marshall, 1996 #3].

The 3-D location of each paired or unpaired FISH spot was obtained by first interactively picking a point in the vicinity of the FISH spot in each nucleus. Note that only nuclei with signals of distinct size and intensity were examined. From that picked point, an automatic search for the maximum intensity pixel was made in an area specified by a given xy and z-range. The 3-D location was further refined by calculating the intensity-weighted center of mass coordinates for that spot. Each FISH spot was then assigned to the nucleus

whose surface enclosed it. At this point, its 3-D location was converted into the coordinate system of its assigned nucleus.

Determination of Progression in Cycle 14 Interphase from Nuclear Elongation

Embryos were bleach-dechorionated and injected at midlength as generally described in (Minden, 1989) 40,000 MW fluorescein dextran (Molecular Probes, Eugene, OR) was injected at a concentration of 2 mg/ml. Time-lapse, 3-D data stacks of embryonic nuclei starting from mid-cycle 13 interphase to mid-cycle 14 interphase were collected with our CCD-based 3-D wide-field fluorescence microscope. Using a 0.2 sec exposure time, the living embryos were imaged using the same lens and oil configuration as for the hybridized embryos. The average nuclear length was obtained by measuring the top and the bottom of the nuclear volumes created by the excluded dextran. A least-squares analysis of nuclear length as a function of time determined a best-fit second degree polynomial with an R^2 value of 0.9188. Using the equation from the fit, -0.0044t2 + 0.4371t + (4.0754-ht) = 0 where t=time and ht =nuclear length, the time of progression for any cycle 14 embryo for the first 50 minutes of cycle 14 interphase was determined from knowledge of average height of the nuclei for that embryo.

Simulations

Diffusive motion was simulated using a random walk on a cubic lattice (Kao and Verkman, 1994). The average size of unpaired FISH signals was used for the size of the particles representing the unpaired loci. For each run, pairs of particles were initialized to positions reflecting the initial distribution of the site obtained from the experimentally measured average radial and vertical positions, $\langle r_o \rangle$ and $\langle z_o \rangle$ and their respective standard deviations, σ_{ro} and σ_{zo}. A normal distribution of the particles was generated using these measured values as a starting point for the simulation. A 3-D random walk for each pair of

particles was then simulated. Each iteration of the simulation represented a small time step of $\tau = 50$ ms. At each step, the x, y, and z coordinates were incremented and decremented with equal probability by an amount $\delta = 2D\tau$, where D is the diffusion coefficient. Spatial constraints were imposed on the entire random walk by limiting motion within a cylindrical volume specified by a radial boundary and a vertical boundary. In order to measure the potential range of radial and vertical positions, we measured the average radial and vertical postions <r> and <z> along with their standard deviations, σ_r and σ_z over the duration of pairing. The radial and vertical boundaries were then taken as $\langle r \rangle + \sigma_r$ and $\langle z \rangle \pm \sigma_z$. Also at each step, the pairing state and the distance between unpaired particles were calculated. Two particles were considered paired if the distance between them was less than the diameter of an particle. The results from the pairing evaluations were recorded every 20 secs of the simulation. 1000 such runs were carried out for each simulation and the results pooled to obtain the profiles of the overall pairing frequency and average inter-homolog distance as a function of time.

To simulate a directed motion model with constant velocity, the same initial conditions, boundaries, and pairing evaluations employed in the random walk simulations were used. However at each step, the positions of the two points were moved directly towards each other by an amount $\delta = v\tau$, where v is the velocity.

References

Aramayo, R. and Metzenberg, R. L. (1996). Meiotic transvection in fungi. Cell *86*, 103-13.

Arnoldus, E. P., Peters, A. C., Bots, G. T., Raap, A. K. and van der Ploeg, M. (1989). Somatic pairing of chromosome 1 centromeres in interphase nuclei of human cerebellum. Human Genetics *83*, 231-4.

Bennett, M. D. (1977). The timing and duration of meiosis. Phil. Trans. R. Soc. Lond. Ser. B *277*, 201-226.

Bennett, M. D., Rao, M. K., Smith, J. B. and Bayliss, M. W. (1973). Cell development in the anther, ovule, and young seed of Triticum aestivum L. cv. Chinese Spring. Phil. Trans. R. Soc. Ser. B *266*, 39-81.

Bennett, M. D., Smith, J. B., Simpson, S. and Wells, B. (1979). Intranuclear fibrillar material in cereal pollen mother cells. Chromosoma *71*, 289-332.

Bollmann, J., Carpenter, R. and Coen, E. S. (1991). Allelic interactions at the nivea locus of Antirrhinum. Plant Cell *3*, 1327-36.

Brown, W. V. and Stack, S. M. (1968). Somatic pairing as a regular prelimary to meiosis. Bull. Torrey Bot. Club *95*, 369-378.

Cabot, E. L., Doshi, P., Wu, M. L. and Wu, C. I. (1993). Population genetics of tandem repeats in centromeric heterochromatin: unequal crossing over and chromosomal divergence at the Responder locus of Drosophila melanogaster. Genetics *135*, 477-87.

Chikashige, Y., Ding, D. Q., Funabiki, H., Haraguchi, T., Mashiko, S., Yanagida, M. and Hiraoka, Y. (1994). Telomere-led premeiotic chromosome movement in fission yeast. Science *264*, 270-3.

Colot, V., Maloisel, L. and Rossignol, J. L. (1996). Interchromosomal Transfer Of Epigenetic States In Ascobolus - Transfer Of Dna Methylation Is Mechanistically Related To Homologous Recombination. Cell *86*, 855-864.

Crank, J. (1956). The mathematics of diffusion. (Oxford: Clarendon Press).

Dawe, R. K., Sedat, J. W., Agard, D. A. and Cande, W. Z. (1994). Meiotic Chromosome Pairing In Maize Is Associated With A Novel Chromatin Organization. Cell *76*, 901-912.

Dernburg, A. F., Sedat, J. W., Cande, W. Z. and Bass, H. W. (1995). Cytology of Telomeres. In Telomeres, E. H. Blackburn and C. W. Greider, ed. (Plainview: Cold Spring Harbor Laboratory), 295-338.

Dernburg, A. F., Sedat, J. W. and Hawley, R. S. (1996). Direct Evidence Of A Role For Heterochromatin In Meiotic Chromosome Segregation. Cell *86*, 135-146.

Dorninger, D., Karigl, G. and Loidl, J. (1995). Simulation of chromosomal homology searching in meiotic pairing. Journal of Theoretical Biology *176*, 247-60.

Edgar, B. A. and O'Farrell, P. H. (1990). The three postblastoderm cell cycles of Drosophila embryogenesis are regulated in G2 by string. Cell *62*, 469-80.

Edgar, B. A. and Schubiger, G. (1986). Parameters controlling transcriptional activation during early Drosophila development. Cell *44*, 871-7.

Foe, V. E. (1989). Mitotic domains reveal early commitment of cells in Drosophila embryos. Development *107*, 1-22.

Foe, V. E. and Alberts, B. M. (1983). Studies of nuclear and cytoplasmic behaviour during the five mitotic cycles that precede gastrulation in Drosophila embryogenesis. Journal of Cell Science *61*, 31-70.

Foe, V. E. and Alberts, B. M. (1985). Reversible chromosome condensation induced in Drosophila embryos by anoxia: visualization of interphase nuclear organization. Journal of Cell Biology *100*, 1623-36.

Foe, V. E., Odell, G. M. and Edgar, B. A. (1993). Mitosis and Morphogenesis in the Drosophila Embryo. In The Development of Drosophila melanogaster, M. Bate and A. Martinez Arias, ed. (Plainview, N.Y.: Cold Spring Harbor Laboratory Press), 149-300.

Fussell, C. P. (1987). The Rabl orientation: A prelude to synapsis. In Meiosis, P. B. Moens, ed. (Orlando, Florida: Academic Press), 275-.

Goldsborough, A. S. and Kornberg, T. B. (1996). Reduction of transcription by homologue asynapsis in Drosophila imaginal discs. Nature *381*, 807-10.

Gorbsky, G. J. (1992). Chromosome motion in mitosis. Bioessays *14*, 73-80.

Haaf, T. and Schmid, M. (1991). Chromosome topology in mammalian interphase nuclei. Experimental Cell Research *192*, 325-32.

Haaf, T., Steinlein, K. and Schmid, M. (1986). Preferential somatic pairing between homologous heterochromatic regions of human chromosomes. American Journal of Human Genetics *38*, 319-29.

Hartl, D. L., Nurminsky, D. I., Jones, R. W. and Lozovskaya, E. R. (1994). Genome structure and evolution in Drosophila: applications of the framework P1 map. Proceedings of the National Academy of Sciences of the United States of America *91*, 6824-9.

Hiraoka, Y., Dernburg, A. F., Parmelee, S. J., Rykowski, M. C., Agard, D. A. and Sedat, J. W. (1993). The Onset Of Homologous Chromosome Pairing During Drosophila-Melanogaster Embryogenesis. Journal Of Cell Biology *120*, 591-600.

Holliday, R. (1968). Genetic recombination in fungi. In Replication and recombination of genetic material, W. J. Peacock and R. D. Brock, ed. (Canberra: Australian Academy of Science), 157-174.

Kalpin, R. F., Daily, D. R. and Sullivan, W. (1994). Use of dextran beads for live analysis of the nuclear division and nuclear envelope breakdown/reformation cycles in the Drosophila embryo. Biotechniques *17*, 730, 732-3.

Kao, H. P. and Verkman, A. S. (1994). Tracking of single fluorescent particles in three dimensions: use of cylindrical optics to encode particle position. Biophysical Journal *67*, 1291-300.

Kleckner, N., Padmore, R. and Bishop, D. K. (1991). Meiotic chromosome metabolism: one view. Cold Spring Harbor Symposia on Quantitative Biology *56*, 729-43.

Kleckner, N. and Weiner, B. M. (1993). Potential Advantages Of Unstable Interactions For Fairing Of Chromosomes In Meiotic, Somatic, And Premeiotic Cells. Cold Spring Harbor Symposia On Quantitative Biology *58*, 553-565.

LaSalle, J. M. and Lalande, M. (1996). Homologous association of oppositely imprinted chromosomal domains. Science *272*, 725-8.

Lewis, E. B. (1954). The theory and application of a new method of detecting chromosomal rearrangements in Drosophila melanogaster. Am. Nat. *88*, 225-239.

Lewis, J. P., Tanke, H. J., Raap, A. K., Beverstock, G. C. and Kluin-Nelemans, H. C. (1993). Somatic pairing of centromeres and short arms of chromosome 15 in the hematopoietic and lymphoid system. Human Genetics *92*, 577-82.

Lifton, R. P., Goldberg, M. L., Karp, R. W. and Hogness, D. S. (1977). The organization of the histone genes in Drosophila melanogaster: function and evolutionary implications. Cold Spring Harbor Symp. Quant. Biol. *42*, 1047-1051.

Lohe, A. R., Hilliker, A. J. and Roberts, P. A. (1993). Mapping simple repeated DNA sequences in heterochromatin of Drosophila melanogaster. Genetics *134*, 1149-1174.

Loidl, J. (1990). The initiation of meiotic chromosome pairing: the cytological view. Genome *33*, 759-78.

Loidl, J. and Langer, H. (1993). Evaluation of models of homologue search with respect to their efficiency on meiotic pairing. Heredity *71 (Pt 4)*, 342-51.

Maguire, M. (1983a). Chromosome behavior at premeiotic mitosis in maize. J. Hered. *74*, 93-96.

Maguire, M. (1983b). Homologous chromosome pairing remains an unsolved problem: a test of a popular hypothesis utilizing maize meiosis. Genetics *104*, 173-179.

Marshall, W. F., Dernburg, A. F., Harmon, B., Agard, D. A. and Sedat, J. W. (1996). Specific Interactions Of Chromatin With The Nuclear Envelope - Positional Determination Within The Nucleus In Drosophila Melanogaster. Molecular Biology Of The Cell *7*, 825-842.

Mckee, B. D. (1996). The License To Pair - Identification Of Meiotic Pairing Sites In Drosophila. Chromosoma *105*, 135-141.

McKee, B. D., Lumsden, S. E. and Das, S. (1993). The distribution of male meiotic pairing sites on chromosome 2 of Drosophila melanogaster: meiotic pairing and segregation of 2-Y transpositions. Chromosoma *102*, 180-94.

Metz, C. W. (1916). Chromosome studies on the Diptera II. The paired association of chromosomes in the Diptera and its significance. J. Exp. Zool. *21*, 213-279.

Patterson, G. I. and Chandler, V. L. (1995). Paramutation in maize and related allelic interactions. Current Topics in Microbiology and Immunology *197*, 121-41.

Roeder, G. S. (1995). Sex And The Single Cell - Meiosis In Yeast. Proceedings Of The National Academy Of Sciences Of The United States Of America *92*, 10450-10456.

Scherthan, H. S., Weich, S. H., Harle, M., Heyting, C. and Cremer, T. (1996). Centromere and telomere movements during early meiotic prophase of mouse and man are associated with the onset of chromosome pairing. J. Cell Biol. *134*, 1109-1125.

Smithies, O. and Powers, P. A. (1986). Gene conversions and their relation to homologous chromosome pairing. Philosophical Transactions of the Royal Society of London. Series B: Biological Sciences *312*, 291-302.

Smolik-Utlaut, S. M. and Gelbart, W. M. (1987). The effects of chromosomal rearrangements on the zeste-white interaction in Drosophila melanogaster. Genetics *116*, 285-98.

Tartof, K. D. and Henikoff, S. (1991). Trans-sensing effects from Drosophila to humans. Cell *65*, 201-3.

Vourc'h, C., Taruscio, D., Boyle, A. L. and Ward, D. C. (1993). Cell cycle-dependent distribution of telomeres, centromeres, and chromosome-specific subsatellite domains in the interphase nucleus of mouse lymphocytes. Exp. Cell Res. *205*, 142-151.

Wakimoto, B. T. and Hearn, M. G. (1990). The effects of chromosome rearrangements on the expression of heterochromatic genes in chromosome 2L of Drosophila melanogaster. Genetics *125*, 141-54.

Weiner, B. M. and Kleckner, N. (1994). Chromosome Pairing Via Multiple Interstitial Interactions Before And During Meiosis In Yeast. Cell *77*, 977-991.

Williamson, D. H., Johnston, L. H., Fennell, D. J. and Simchen, G. (1983). The timing of S phase and other nuclear events in yeast meiosis. Exp. Cell Res. *145*, 209-217.

Chapter 2 :

Assembly of the Synaptonemal Complex from Zea mays Observed by Electron Microscopic Tomography

Summary

The synaptonemal complex (SC) has been shown to be necessary in maintaining synapsis between homologous chromosomes and in ensuring proper segregation of the homologs through the establishment of functional chiasmata. In order to understand how the structural components of the SC relate to its function, we have studied the three-dimensional organization of the SC in *Zea mays L* meiocytes as a function of its progression through the early stages of prophase I. To obtain high resolution details of SC structure in three-dimensions, we have utilized the technique of intermediate voltage electron microscopy (IVEM) tomography. High pressure freezing of maize anthers was also employed to best preserve the the early SC and its surrounding chromatin in the prophase I meiocytes. IVEM tomographic reconstructions from pachytene meiocytes reveal that the central element of the SC, thought to be amorphous in maize in fact consists of two subunits. The most prominent of these subunits is a 110 Å central component which runs longitudinally down the center of the central element (CE). Flanking this component is a larger element, 530 Å in width, which runs down the long axis of the CE. Transverse elements running from the 530 Å component to the lateral elements can also be observed in these reconstructions. Interestingly, in the synapsed regions from zygotene meiocytes, the CE consists only of the 110 Å central component and no evidence of transverse elements is found. This suggests that the CE formation is a multistep process with the 110 Å central component forming first in zygotene, followed by the incorporation of the 530 Å subunits and the transverse elements during pachytene.

Introduction

Meiosis is a type of cell division in which the number of chromosomes are reduced in half in preparation for gamete fusion during sexual reproduction. Critical to this process is the proper segregation of the homologous chromosomes at the first of the two meiotic divisions. Successful segregration of the chromosomes greatly depends on three

important events: homolog pairing (Loidl, 1990; Kleckner et al., 1991), homolog synapsis (Roeder, 1995) and reciprocal recombination (Kleckner, 1996). In turn, these events are all linked to the assembly and function of a meiosis specific organelle, the synaptonemal complex (SC) (Westergaard and von Wettstein, 1972; von Wettstein et al., 1984).

The SC is a macromolecular structure assembled during prophase of the first meiotic division. SC assembly is first detected by the formation of axial elements which appear as proteinaceous structures between the sister chromatids of each homologue during the leptotene stage of prophase I. When axial element assembly is completed, these structures are seen to run along the entire length of the condensed homologue and, in the context of the SC, are referred to as lateral elements. At zygotene, synapsis of short segments of the axial elements follows. This synapsis is most often seen beginning at telomeres but can originate at interstitial regions as well. Next, elongation of the SC between the homologs is observed as the cells progress from zygotene into pachytene. It is during pachytene that the SC is considered completely assembled. At this point, chromosomes are found fully synapsed with only a 100 nm separation between lateral elements (formerly axial elements) which run parallel along the entire chromosomal length. This separation between the two lateral elements marks the width of the central region. The central region's most prominent feature is the central element that runs longitudinally down the middle of the SC. Between the central element and the lateral elements, the central region appears less dense. In many organisms, transverse elements, perpendicular to the length of the SC, can been seen joining the central element to the lateral elements across this region..

Cytological examination of SCs from a wide variety of organisms has shown that the basic features of SC organization are conserved (von Wettstein et al., 1984). These basic features, consisting of two lateral elements and a central element, form what is refered to, as the tripartite structure of the SC. However, for most SCs, except for those found in

many fungi and most insects (Westergaard and von Wettstein, 1972), the details of the structure of each individual component remain obscure. Revealing the subtler details requires higher resolution imaging techniques combined with better preservation methods for the sample.

Advances are now being made in high resolution 3-D microscopy where the use of intermediate and high voltage electron tomography is paving the way to revelations into the intricate details of biological substructure from such cellular components as centrosomes (Moritz et al., 1995), chromatin (Horowitz et al., 1994) and kinetochores (McEwen et al., 1993). Because this method creates a 3-D representation of the electron microscopic sample, a clearer picture of the actual construction of the biological structure, which itself is three-dimensional, can be obtained.

In addition, new techniques have been developed that provide an alternative to the standard chemical fixation methods used normally to preserve samples destined for the electron microscope. The recent ability to use high pressure freezing improves specimen preparation so that relatively large (< 0.5 mm), difficult-to-fix, whole tissues can be preserved intact with little disruption of native structure (Dahl and Staehelin, 1989; Dubochet, 1995). This technique has already been shown to better preserve the morphology of cellular structures from a large range of organisms including yeast cells (Winey et al., 1995), Drosophila embryos (Mcdonald and Morphew, 1993) and several tissues in plants (Studer et al., 1992; Kaneko and Walther, 1995; Samuels et al., 1995). In this paper, we focused on using these techniques to address the details in the architecture of the SC. In particular, we have concentrated on following the assembly of the amorphous central region of the maize SC.

One important function for the SC is the creation and maintenance of synapsis between homologous chromosomes. Many meiotic mutants found with defects in segregation also display defects in synapsis (Hollingsworth et al., 1990; Rockmill and Roeder, 1990; Maguire et al., 1993). In yeast, lack of synapsis, in some instances, can be

attributed to mutations affecting proteins in the central region of the SC. One such protein is Zip1 which is a candidate for being major subunit of the transverse elements. Null mutations of the Zip1 protein, result in axial elements that are paired but not synapsed (Sym et al., 1993). A similar significance of the central region for attaining synapsis can also be demonstrated in maize. In maize, desynaptic mutants (Nelson and Clary, 1952; Golubovskaya and Mashnenkov, 1976; Golubovskaya and Urbach, 1981) are found which exhibit only partial synapsis of the homologous chromosomes. Cytological examination of the SCs from such mutants have determined that although lateral element formation is complete, central region formation is incomplete as inferred by the wider than normal average for central region widths (Maguire et al., 1991; 1993). Some consequences of such defective synapsis are premature degradation of the SC and precocious sister chromatid separation (Maguire, 1978b). Normally, degradation of the SC and dissolution of sister chromatid cohesion normally only occur after pachytene during the following diplotene and diakinesis stages of prophase I. To more fully understand how changes in the central region can lead to such dire consequences in SC function, greater understanding of how synapsis is attained will be an important part in solving this puzzle.

A good model system to study the cytology of the SC is the male meiocyte of maize (Zea mays). The most attractive aspect of the maize system is the ability to identify meiotic stages using the natural biology of the developing maize tassel. Anthers, organs containing the precursors of pollen, are arranged in order of increasing meiotic development along the length of the tassel. Within each anther, all meiocytes are synchronized to the same meiotic stage. In this maize system, the lengths of the anthers correlate well with particular stages of meiosis (Chang and Neuffer, 1989). The maize system provides another advantage, in that the chromosomes can be easily identified and assigned to particular stages of prophase I (Dawe et al., 1994; Bass et al., 1997). The combination of all these features of maize pollen development allows for easy

identification of the meiotic progression of each anther, as well as exact staging of the temporal course of meiosis from one anther relative to another.

Here, by using intermediate voltage electron tomography, we report that the previously described amorphous central element in the mature maize SC consists in fact of two distinct subunits. The most prominent of these subunits is an 110 Å component that runs straight through the center of the central element. Flanking this 110 Å component is a larger 530 Å subunit making up the bulk of the central element down the axis of the synapsed homologs. We find that transverse elements are evident in the central region of the mature pachytene SC and are seen to loop from one lateral element to the central element and back to the same lateral element, thereby showing a more complex connection between lateral element and central element than had been previously noted in other organisms. Furthermore, by reconstructing the synapsed regions of zygotene chromosomes, we show that the structures found in the central region of the pachytene bivalent are not all present during the zygotene stage. During the zygotene stage, when synaptic initiation begins, only the 110 Å component could be found. This suggests that both the missing 530 Å subunit and the transverse elements are not needed in the early step of synaptic initiation and may be part of a later SC function. However, because the 110 Å component was present at this early stage, it may function as part of the synapsis initiation machinery.

Materials and Methods

Preparation of Meiocytes in Pachytene

The inbred W23 line was obtained from the UC Berkeley greenhouse courtesy of W. Zacheus Cande. Anthers ~ 2mm in length were dissected from florets in buffer A (Belmont et al., 1989) and placed in fixative buffer solutions containing 4% formaldehyde (diluted from a freshly prepared 16% solution of formaldehyde), 1%

glutaldehyde (EM Grade, Polysciences Inc., Warrington, PA), buffer A and a variety of concentrations of sorbitol (0.275, 0.300, 0.325, 0.350 M) in petri dishes. The different sorbitol concentrations were necessary to best match the osmolarity of the anthers. The petri dishes were placed on a shaker (120 rpm) for 2 hours at room temperature. Fixative buffers were changed twice in the 2 hours. Anthers were rinsed twice with buffer A for 5 minutes each on the shaker before being dissected in buffer A with the corresponding sorbital concentration on a "Silastic" pad (FD Titus Inc, Oakland, CA). One end of each anther was cut using a Micro-Couteau 15^{o} scalpel (Fine Science Tools (USA) Inc, Foster City, CA) . By gently stroking the anthers towards the cut end, meiocytes were extruded in a column. Columns were then examined in the dissecting microscope to assess if the osmolarity conditions were chosen correctly. Columns containing meiocytes that were not shriveled or broken were retained in an 1.5 ml Eppendorf in buffer A without the DTT on ice. After 20 or more anthers were collected, the anthers were post-fixed with 2% glutaldehyde in the buffer A with the matching sorbitol concentration for 4 hours on ice under constant shaking. After 3 rinses, the anthers were fixed again with 1% osmium tetroxide in buffer A for 1 hour. The samples were dehydrated on ice in increasing 10% steps of ethanol in buffer A with 2 steps in 100% ethanol and each step lasting 15 minutes. The samples were infiltrated with Epon 812 using standard protocols (Hayat, 1981) and cured for 1 day at 40^{o} C and 2 days at 60^{o} C.

Preparation of Zygotene Meiocytes

Due to the inability of using conventional methods to fix meiocytes in the zygotene stage while maintaining the structural integrity of the chromosomes and the SC, it was necessary to use the alternative method of high pressure freezing to prepare zygotene meiocytes. 1.5 - 1.75 mm anthers were dissected from florets in buffer A containing 0.300 M sorbitol. In this case, the sorbitol was also used as a cryoprotectant in addition to its use in adjusting the osmolarity. The two pairs of locules making up the anther were

dissected apart using a microsurgical scalpel. Any bubbles attached to the anthers were removed before placing one to two pairs of locules either in the copper sample holder (Dahl and Staehelin, 1989) or in the brass sample holder (Swiss Precision Inc., Palo Alto, CA). Enough buffer was added so that no air was present when the sample holders were closed. Immediately the samples were frozen in a Balzers HPM010 high pressure freezer (Bal-Tec Corp., Middlebury, CT). Permission to use of the high pressure freezer was courteously granted by Andrew Staehelin and Tom Giddings at the University of Colorodo, Boulder. Samples were then stored under liquid nitrogen and dry-shipped to UCSF until freeze-substitution. Freeze-substitution was carried as described in Morphew and McDonald (1993) in 2% osmium tetroxide and 8% dimethoxypropane in anhydrous acetone. Samples were infiltrated with Epon as described in previous sections.

Electron Microscopy

Semi-thick 0.3um sections were cut using a semi Diatome diamond knife (Diatome-USA, Fort Washington, PA) on a Reichart Ultracut E microtome (Leica Instruments, Wein, Austria) and placed on formvar coated 50/200 copper grids (Ted Pella Inc, Redding, CA). Sections were then stained with 0.25% uranyl acetate in 70% ethanol for 45 min. and 0.02% lead citrate for 15 minutes. An intermediate voltage 300 kV Phillips EM430 transmission electron microscope equiped with a prototype CCD camera was used to image and obtain tomographic data stacks from the sections. Only sections showing no ice damage to the cell were used for the eventual data collections. 15 nm gold beads (Amersham Life Science Inc., Arlington Heights, IL) were sonicated and placed on the sections which were coated with a 1-2% poly-lysine solution (Sigma, St. Louis, MO). Grids were then carbon-coated for added support. Generally, data was collected at 10.3K or 13.6K magnification with corresponding pixel sizes of 27.65 Å and 21.0 Å. The angular range of the tilts were at least +/- 70 degrees every 1.25 degree.

Tomographic data was collected as described in Fung et al. (1996). For most cases, an image of size 480 x 480 pixels was collected for each tilt angle.

For some data sets of the pachytene chromosomes, an extended region of the chromosomes was obtained by collecting a series of montage views for every tilt angle. For these montage data sets, each view contained five images: a center 480 x 480 image and four surrounding images whose center positions were offset by 200 pixels in x and y (position of center pixel of the 4 surrounding images: -200, 200; -200, -200; 200, 200 and 200, -200). Cross-correlation was used in the overlap regions of each of the four surrounding images with the center image to align all five images to form a montaged 880 x 880 view to be subsequently used in the reconstruction.

3D Reconstuction, Image Processing and Modeling

Reconstruction of the tomographic data was carried out as described in Fung et al. (1993). The reconstruction method used was the elliptical weighted back projection. Shrinkage was measured and the cummulative lateral shrinkage was less than 1%. Most of the subsequent analysis and display was carried out on our Priism/IVE platform (Chen et al., 1996). 3-D modeling of the transverse elements was done using three views of the reconstructed SC at the same time: a projected view, a 90 degree rotated view and the original unrotated view. For some cases, a local contrast enhancement algorithm was used to process images so that unique features of the SC could be accentuated for easier modeling.

Results

Pachytene meiocytes show a high level of preservation

We began our study by determining the conditions that best preserved overall morphology of the meiocytes. Figure 1 shows images of meiocytes taken at 1700x magnification from of a 0.3 um thick section of a 2.0 mm (pachytene stage) maize anther prepared for the EM using conventional chemical fixation methods specifically derived to preserve the morphology of the meiocyte nuclei. The criteria for good preservation of the meiocytes within the anther is judged by the excellent preservation of the nuclear envelope as observed by the distinct doubleness of the membrane layers (Figure 1C) and the smoothness of its contour (Figure 1A and 1B). Evaluation of these cellular features is often used to indicate the quality of preservation of a sample (McDonald and Morphew, 1993). Good nuclear preservation is also evident in the sharp definition in the substructure of the chromatin. The two meioctyes (Figure 1A and 1B) are both in the pachytene stage of prophase I and correspond well to the characteristics of that stage as seen by optical microscopy (Dawe et al., 1994; Bass et al., 1997). During pachytene, the homologous chromosomes are completely synapsed along their lengths with the SC formed between them in the central region. Several examples of the side by side alignment of homologous chromosomes are evident (Figure 1A and 1B) but because the thickness of the sample, the SC is obscured and only a featureless space separating the two homologues is observed (Figure 1C and 1B).

Electron tomography is used to explore the detail architecture of the SC

To reveal details of SC architecture from within the surrounding chromatin, tomographic reconstruction was employed. The basis of electron tomography is to reconstruct a 3-D object from its projections taken at a series of different tilt angles (Frank, 1992). Because of the large depth of focus inherent to the electron microscope,

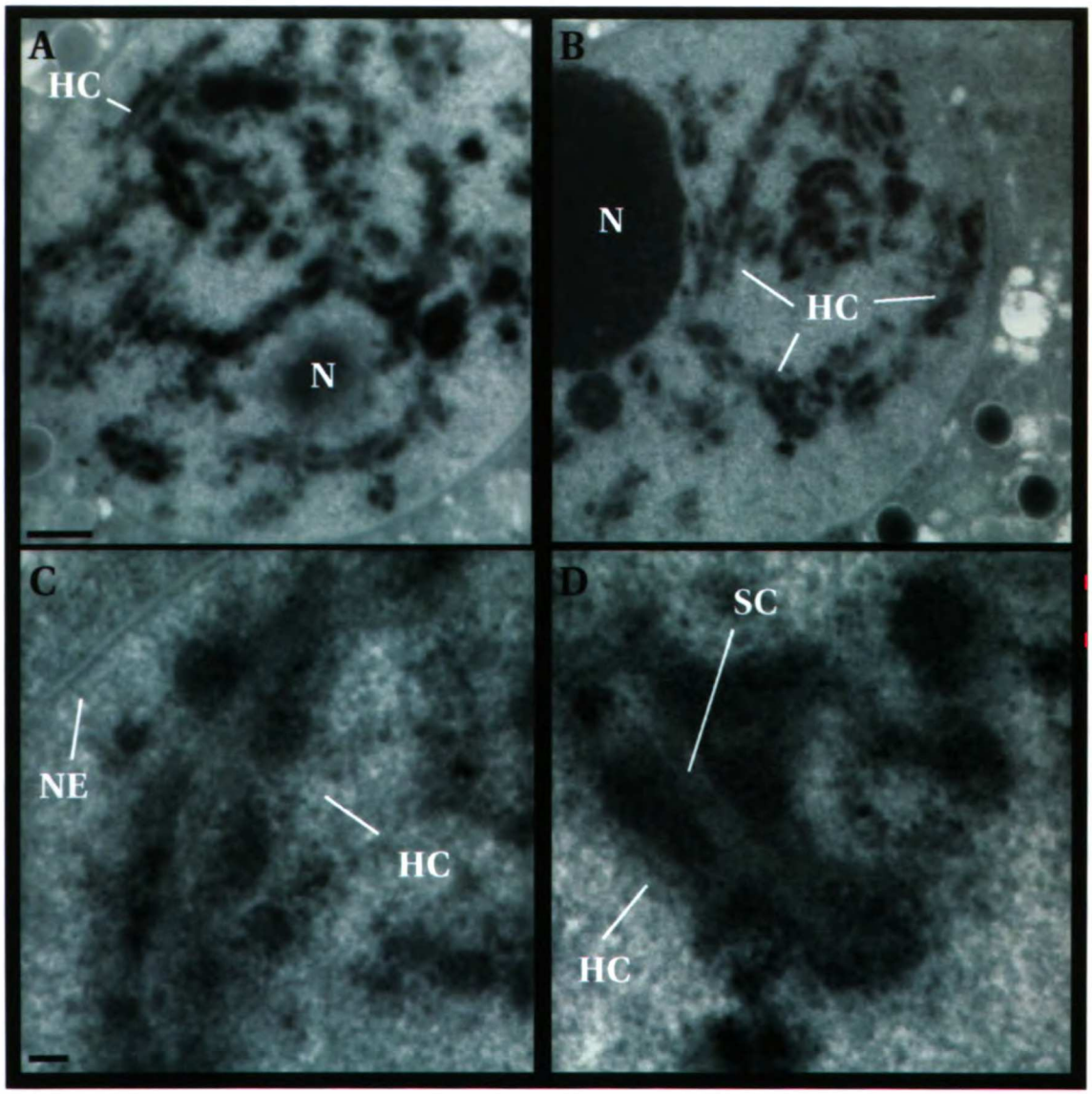

Figure 2.1 Electron micrographs taken of semi-thick sections from maize anthers showing the level of preservation for the pachytene meiocytes and chromosomes. (A–B) The top panels show low magnification views (1700x) of the meiocytes. Structures typically within this cell during the pachytene stage are evident. Homologous chromosomes (HC) are clearly synapsed all along their observable length. The nucleolus (N) is offset from the center of the nucleus as expected for pachytene meiocytes. The high level of preservation is indicated by the smoothness of the cell contour and sharpness of the chromatin boundaries. Scale bar, 1μm. (C–D) Higher magnification views (10,300x) of the meioctyes highlighting the synapsed chromosomes. The region between the synapsed homologues contains the synaptonemal complex (SC). The components of the tripartite SC structure are not visible in these semi-thick sections. At this magnification, the double membrane nuclear envelope (NE) can be seen. Scale bar, 100nm.

electron microscopic images, in fact, can be considered projections of the observed sample. By tilting a sample in the electron microscope at set angles around an axis perpendicular to the electron beam, a series of images (tilt sections) can be obtained which can then be used to reconstruct a 3-D representation of the sample. For our structural characterizations, electron tomography was carried out in an intermediate voltage electron microscope allowing for greater electron penetrance so that semi-thick sections of meiocytes could be examined. By cutting semi-thick sections (0.3 um), a greater likelihood existed that the SC could be entirely contained within one section, thereby, minimizing the damage to SC structure by the sectioning process.

Five tomographic data sets were collected from the fully synapsed pachytene homologues and reconstructed to a resolution of approximately 55 Å (see Materials and Methods for details on the reconstruction process). A typical reconstructed synapsed homologue is shown in Figure 2. Several equally spaced sections from the reconstruction are displayed showing the homologue and SC as the higher intensity regions. After the reconstruction, regions of increased mass density is shown as increased intensity. Note that the contrast is opposite to what is normally observed in a 2-D electron micrograph where the homologues are dark and the background is light (compare with Figure 1).

Novel components of the central region of the SC are revealed by the tomographic reconstructions

Initial analysis of the SC organization from our tomographic reconstructions showed that the basic features of the tripartite structure can be found and correspond well with earlier studies using single micrographs to examine the pachytene bivalent (Gillies, 1973). For instance, the average width of the lateral element, 500 Å, the average central element width, 530 Å, and the span of the central region, 1130 Å, were all within the range of previously reported values for these dimensions. Interestingly, the tomographic reconstructions of the SC showed several additional features of SC organization which

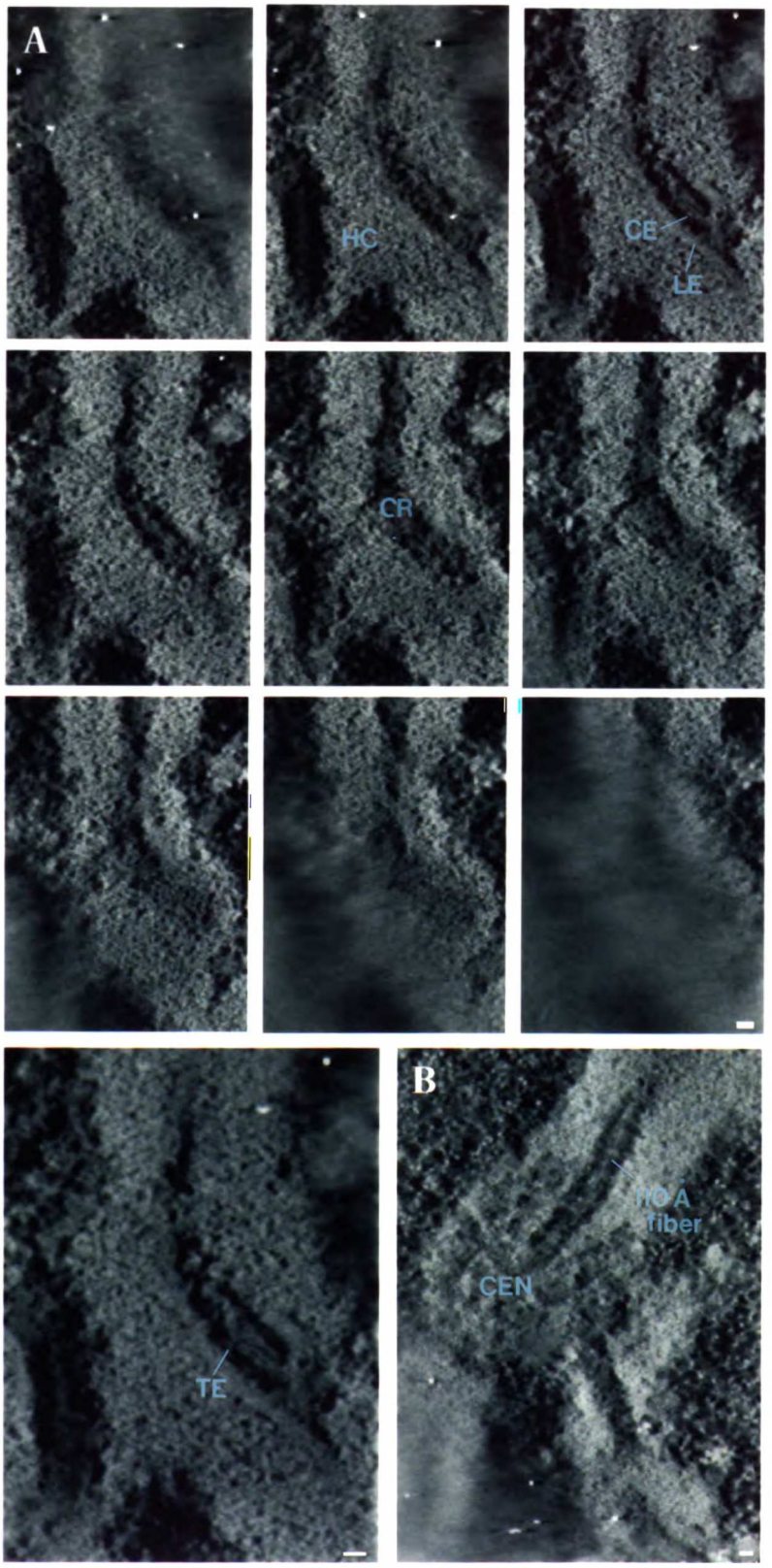
A
HC
CE
LE
CR
TE
B
HO A fiber
CEN

Figure 2.2 Representative reconstructions of the fully synapsed pachytene homologue. (A) The series of images are a subset taken from the 3-D reconstruction at intervals of 83 Å along the z-axis. The z-axis is parallel to the optical axis of the electron microscope. The sections are arranged so that the top of the reconstruction starts at the top left and reads from left to right, top to bottom. The bottom panel contains an enlarged view of the third image in the series to better display the SC. The series taken from the reconstuction indicate that the synapsed homologous chromosomes (HC) fully surround the SC forming a tube of chromatin in which the SC resides. After the reconstruction, several details of the components of the SC can now be detected. The lateral elements (LE), central element (CE), central region (CR) and transverse elements (TE) can all be found. The central element is observed to be formed of two distinct subunits: a 110 Å fiber running down the center of the CE and the larger 530 Å subunit which makes up the bulk of the central element. (B) A representative 2-D slice containing the SC of another pachytene reconstruction. Here the SC runs through the centromere (CEN). The 110 Å fiber can be more clearly observed in this reconstruction. (Scale bars, 50 nm)

had not been previously observed in either single micrograph analysis or serial section reconstructions studies. From Figure 2C and also in Figure XX, we see that the central element, reported to be amorphous, is clearly composed of two distinct subunits The most prominent subunit is a 110 Å component that runs down the center of the element parallel to the long axis of the homologues. This 110 Å component is embedded in a larger subunit, 530 Å wide, that makes up the bulk of the architecture of the central element. This larger 530 Å subunit seemed to split occasionally into two 200 Å subunits but most of the time remained in the 530 Å coalesced form.

Transverse elements were also observed in the central region of the pachytene chromosomes, generally as 100 Å fibers connecting the lateral element to the central element. In insects and fungi, where very regular central regions have been found, transverse elements organize into regular banded rods directly spanning the lateral to central element region. To determine whether such a regular organization also exists in maize, the paths of several transverse elements were traced through the 3-D reconstructions using 3-D polygon building and modeling algorithms. The results of a typical trace for several of the transverse elements are shown in Figure 5. Unexpectedly, these traces show that the paths that transverse elements adopt are quite complicated, much more than a straight lateral element to central element connection. For most cases that we examined, the transverse element forms a loop by starting from one lateral element, crossing to the central element and returning to the same lateral element. Occasionally, a path is found where the transverse element ends in the central element without looping back to lateral element from which it originated. In none of the traces was there evidence that the transverse element bridged both lateral elements. On average the transverse elements traced out a path with a contour length of 1250 Å.

High Pressure Freezing Preserves Zygotene Morphology

Having observed several unique structures making up the organization of the fully formed pachytene SC, we asked to what extent these structures are needed in the early steps of synaptic initiation during zygotene. As a first step towards answering this question, several attempts were made using conventional methods to prepare the zygotene meiocytes to a similar level of preservation as attained with the preparations of the pachtene meiocytes. Unlike the pachytene meiocytes where the developing cell wall nearly encloses the cells, the zygotene meiocytes have less protection from the cell wall where only about two-thirds of the cell's circumference is enclosed. Since a meiocyte column is extruded from the anther as part of the method of specimen preparation, zygotene meiocytes, lacking sufficient protection from the cell wall, are often damaged from this process and show poor signs of preservation in the electron microscope. To avoid this problem, we turned to the relatively new method of high pressure freezing (Studer et al., 1989) in combination with freeze substitution (Kiss and McDonald, 1993) to prepare the zygotene meiocytes. Sample preservation by freezing has been shown to offer the best preservation with little structural distortion (McDonald and Morphew, 1993). High pressure freezing shifts the range where ice crystal formation is problematic so tissues on the order of 0.5 mm can be frozen. Using this method, pairs of locules from zygotene anthers were frozen without the need for extrusion. A typical preparation is shown in Figure 3 demonstrating a high levels of preservation of the nucleus (Figure 3A) and the chromatin (Figure 3B) (compare with Figure 1). The zygotene stage marks the beginning of observable homologue synapsis so unlike in the pachytene nucleus where the homologues are completely synapsed along their lengths (Figure 1A and 1B), the homologues in zygotene nuclei demonstrate only partial synapsis (Figure 3A).

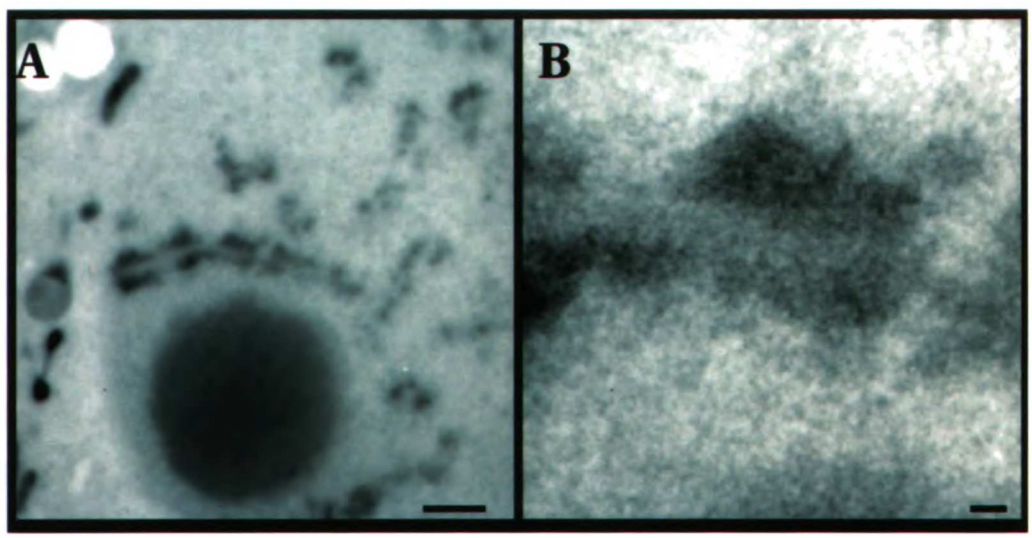

Figure 2.3 Electron micrographs taken of semi-thick sections from high pressure frozen and freeze-substituted maize anthers show the level of preservation for the zygotene meiocytes and chromosomes. (A) Low magnification view (1700x) of a zygotene nucleus. Unlike the pachytene meiocyte, not all regions of the homologous chromosomes are synapsed. Scale bar, 1 μm. (B) Higher magnification of a synapsed region of two homologous chromosomes. Scale bar, 100nm.

Central region components differ in early regions of synapsis and the fully formed SC

Reconstruction of three synapsed regions from different zygotene homologues revealed striking differences in the composition of the central region between zygotene and pachytene synapsed regions. As illustrated in Figure 4 by a series of z-axis slices from the reconstructed data, several substructures seen in the pachytene central region are not observed in the reconstruction of the zygotene central region. A side by side comparison of sections containing the synapsed regions from the two stages are shown and modeled in Figure 5. The central element in the zygotene reconstruction is seen to contain only one distinct subunit, 110 Å in width, whereas the pachytene central element consisted of two subunits 110 Å and 530 Å. A difference was also observed regarding the presence of the transverse elements. While the pachytene central region demonstrated distinct 100 Å transverse fibers, an absence of such transverse elements were noted in the zygotene reconstructions. Although neither the 530 Å central element subunit nor transverse elements were observed in the zygotene reconstruction, regions of detectable levels of density were observed in the central region where these subunits are normally located in the pachytene bivalent. It possible that these low density structures may eventually proceed to form these subunits but not enough information is available to make such a claim. Because the width of the central region was comparable between the zygotene and pachytene synapsed regions (1315 Å vs 1130 Å), we conclude that synapsis between the two homologous regions has already been attained for this particular area of the zygotene chromosomes. Since synapsis has occurred for this region, this implies that neither the 530 Å subunit of the central element nor the transverse elements are required for the early steps in the initiation of synapsis, as determined by their distinct absence at this stage. However, since the 110 Å component is found at the zygotene stage, it remains possible that this component does have a role in the initiation of synapsis of the SC.

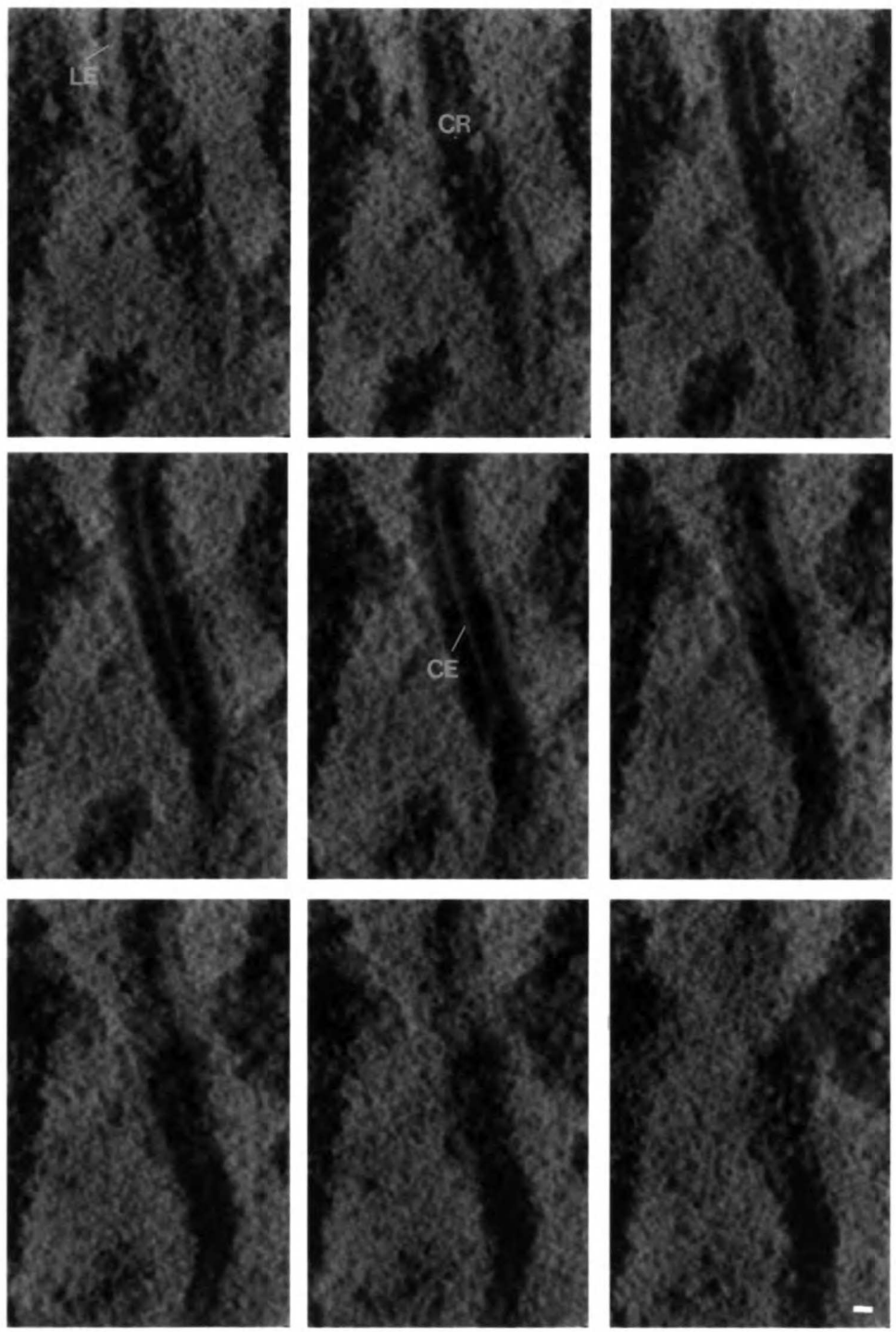
LE
CR
CE

Figure 2.4 Series of images from the reconstruction of the zygotene SC. Images are similarly ordered and are taken from the same interval along the z-axis as in Fig. 2.2. The lateral element (LE), central element (CE), and central region (CR) are all observed. (Scale bar, 50 nm)

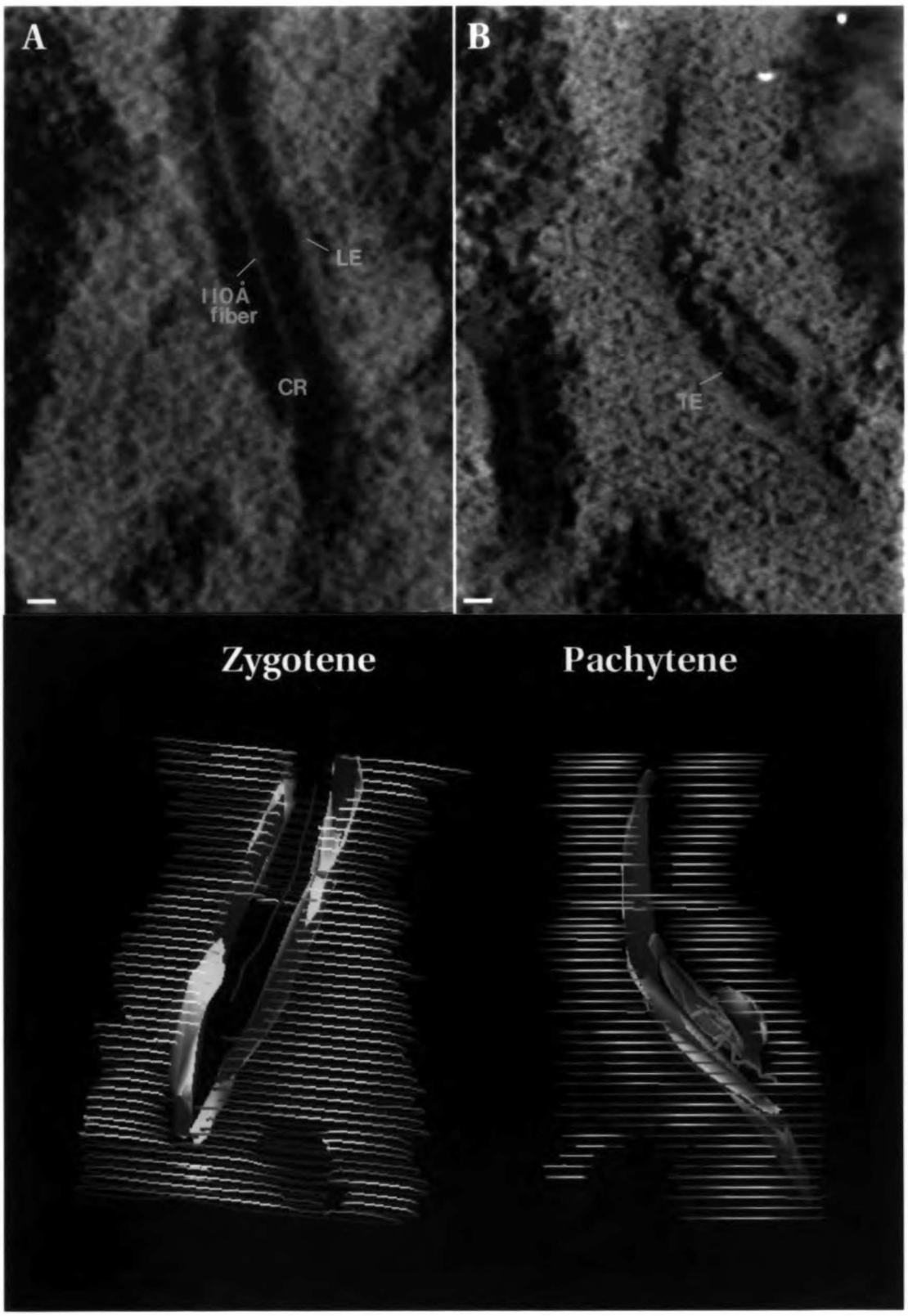
A
LE
110Å
fiber
CR
B
TE
Zygotene
Pachytene

Figure 2.5 Sections containing the SC from pachytene and zygotene reconstruction are compared side by side along with the results of the 3-D modeling. (A) Notably the zygotene SC lacks some of the structural components found in the pachytene SC. In the zygotene reconstruction, the lateral elements (LE) and the central region (CR) are well evident but the central element (CE) only consists of the 110 Å fiber and there is no evidence for transverse elements (TE). In contrast, the pachytene SC contains, in addition to the previous mentioned components, the larger 530 Å component of the central element as well as transverse elements. (B) 3-D models of the SC show that in the pachytene, transverse elements run from one lateral element to the central element but do not cross to the other lateral element often instead looping back to the original lateral element.

Because the reconstructions were obtained from semi-thick sections cut from the zygotene and pachytene anthers, much of the chromosomes surrounding the SC could also be observed. Earlier studies of pachytene chromosomes using serial sectioning techniques have shown that the chromatin fully surrounds the SC forming a tube in which the SC resides (Gillies, 1973). In the pachytene reconstructions, we found this also to be true. In addition, we saw that during zygotene, the chromatin was similarly organized around the synapsed regions making a tube with a slightly elliptical cross-section of (major axis - 1315 Å, minor axis - 870Å). The cross-section in the pachytene reconstructions were 1130 Å (major axis) and 740 Å (minor axis). Further examination of the chromatin showed that the levels of condensation of the chromatin were noticeably different between the two stages. During pachytene, distinct 180-250 Å wide fibers were observed making up the bulk of the substructure of the chromatin (Figure 4). In comparison, chromatin fibers from zygotene chromosomes were less tightly compacted and were grouped in large domains along the axis of the lateral element, unlike the the pachytene chromatin which was arranged more evenly along the lateral element length.

Discussion

Model for SC assembly

Use of intermediate voltage electron tomography to examine the formation of the synaptonemal complex from zygotene to pachytene has revealed specific details about the central region assembly in the maize meiocyte. Based on these observations, we propose a model of central region assembly which is summarized diagrammatically in Figure 6. Comparison of reconstructions from zygotene and pachytene meiocytes show that central element formation begins with assembly of an 110 Å component which is formed within a tube of chromatin constructed from the synapsed homologues. Later at pachytene, this

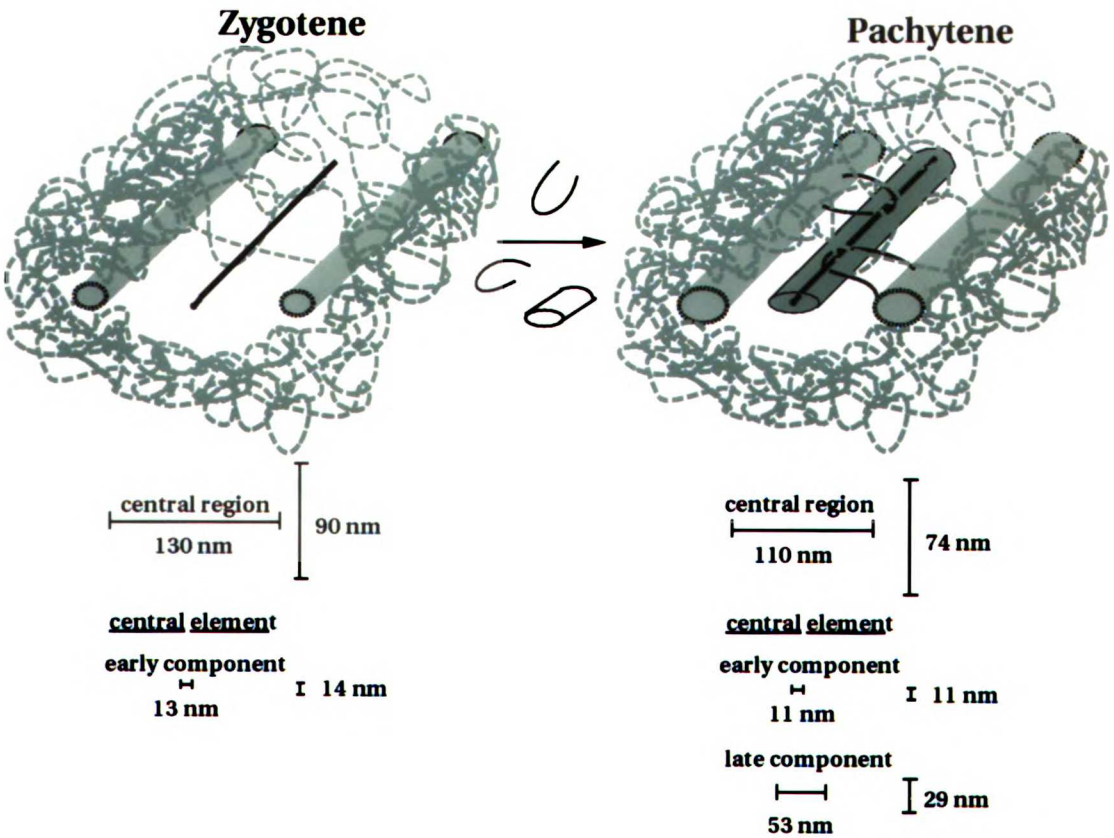

Figure 2.6 Model of SC assembly.

assembly progresses with the incorporation of the 530 Å component into the central element. This is accompanied by the appearance of the 100 Å transverse elements in the central region. The later appearance of both the 530 Å component and the transverse elements suggest that these structures are not involved in the function of synaptic initiation since synapsis has already been achieved at zygotene before the first detection of these structures. However, since the 110 Å is evident at early points of synapsis a possible role for this structure in synaptic initiation may exist.

Appearance of SC components may relate to diverse SC function

The fact that different parts of the central region are assembled at different times may correlate with the onset of the different functions proposed for the SC. Traditionally, the SC was thought to be important for attaining and maintaining the close synapsis of homologous chromosomes. Evidence for this role is demonstrated by the zip1 mutant of Saccharomyces cerevisiae, where homologous chromosomes pair, but fail to synapse, due to the absence of the central region (Sym et al., 1993). Other potential SC functions also includes involvement in promoting recombination. Analysis in yeast of a number of meiotic mutants defective in recombination (Klapholz et al., 1985; Game et al., 1980; Alani et al., 1990; Menees et al., 1992; Menees and Roeder, 1989) show that these mutants also fail to form SCs. It should be noted that although recombination is related to SC formation, the SC is apparently not required for recombination (Hollingsworth and Byers, 1989; Rockmill and Roeder, 1990; Engebrecht and Roeder, 1989; Engebrecht and Roeder, 1990) since detectable levels of recombination can be observed when SC formation is incomplete. Another proposed function for the SC is a role in converting crossovers into functional chiasmata. Chiasmata are important for ensuring proper disjunction of the homologous chromosomes (Maguire, 1978a). Finally, the SC may be important in the mediation of crossover interference such that regions that have already

undergone exchange have a lower probability of another crossover occurring in the same area (Sym and Roeder, 1994). Given the disparate functions proposed for the SC, it is quite possible, that different structures are needed for the early events of synapsis, recombination and cross-over interference than are needed for the later event of the formation of chiasmata. Thus, it is not surprising that different components are being assembled at different times as might be expected to accommodate the diverse functions of the SC which occur over the course of prophase I.

The generality of SC architecture

A review of the model of the pachytene SC based on our reconstructions shows that the maize SC does not fit into the notion that all SC architecture is equivalent. Several insect and fungal SCs have a very ordered appearance in which components of central regions, and sometimes the lateral elements, adopt a banded ladder-like configuration. This can be seen very clearly in single EM micrographs. Tomographic reconstruction of a Blaps cribosa SC indicated that the 3-D banding pattern for the central region arises from a distinct organization where each transverse element is associated with two short central element pillars which is then arranged in an ordered array within the central element (Schmekel et al., 1993a). It has been claimed that this organization of a transverse element associated with two short central pillars forms a basic structural unit not only for the well ordered SCs of the insects Blaps cribosa and Drosophila, but also for the amorphous rat SC (Schmekel et al., 1993b). As a result of this work, it was proposed that all SCs are build from this basic structural unit. However, our work shows that such a architecture cannot be universal since the pachytene reconstructions of maize SC show no such organization. In the maize central element, no such regular pattern of central pillars was observed nor did the transverse elements follow a direct lateral element to central element seen in the reconstruction of the insect and rat SCs. So until more

reconstructions of SCs from a variety of different are available, we propose that is still too soon to decide whether a basic organization for the SC exists for all organisms.

Structural observations correlate with genetic analysis that transverse elements probably involve maintainance of synapsis but not its attainment

In Saccharyomyces cerevisae, the Zip1 protein had been identified as a possible candidate for the transverse element (Sym et al., 1993; 1995). Antibodies against this protein localize to the SC but not unsynapsed axial elements. A prediction for the region within the protein found extensive areas of a-helical coiled coil motif. When dimerized, the predicted length of the Zip1 dimer approximates the width the central region. When the coiled-coil regions were altered to increase the number of copies of the coiled-coil region to two or three more than the normal complement, a corresponding increase in width was seen for the central region. However, when a deletion of the coiled-coil region was made, normal central region distances were found. This suggests that the Zip1 protein is not needed to attain synapsis but may be needed for its maintenance. From the work described in this paper, a structural correlation to this genetic result can drawn. Because we found that the transverse fibers are not seen in zygotene when synapsis is taking place, this agrees with the hypothesis that these fibers are not needed at this time and thus are not involved with attaining synapsis. The fact that these fibers are only seen during pachytene, is in agreement with the idea that the transverse elements may instead have a role in maintaining synapsis.

References

Alani, E., Padmore, R. and Kleckner, N. (1990). Analysis of wild-type and rad50 mutants of yeast suggests an intimate relationship between meiotic chromosome synapsis and recombination. Cell *61*, 419-36.

Bass, H. W., Agard, D. A., Sedat, J. W. and Cande, W. Z. (1997). Telomeres cluster de novo before the initiation of synapsis: a 3-dimensional spatial analysis of telomere positions before and during meiotic prophase. J. Cell Biol. *in press*..

Belmont, A. S., Braunfeld, M. B., Sedat, J. W. and Agard, D. A. (1989). Large-scale chromatin structural domains within mitotic and interphase chromosomes in vivo and in vitro. Chromosoma *98*, 129-43.

Chang, M. T. and Neuffer, M. G. (1989). Maize microsporogenesis. Genome *32*, 232-244.

Chen, H., Hughes, D. D., Chan, T. A., Sedat, J. W. and Agard, D. A. (1996). IVE (Image Visualization Environment): a software platform for all three-dimensional microscopy applications. Journal of Structural Biology *116*, 56-60.

Dahl, R. and Staehelin, L. A. (1989). High-Pressure Freezing For The Preservation Of Biological Structure - Theory And Practice. Journal Of Electron Microscopy Technique *13*, 165-174.

Dawe, R. K., Sedat, J. W., Agard, D. A. and Cande, W. Z. (1994). Meiotic chromosome pairing in maize is associated with a novel chromatin organization. Cell *76*, 901-12.

Dubochet, J. (1995). High-Pressure Freezing For Cryoelectron Microscopy. Trends In Cell Biology *5*, 366-368.

Engebrecht, J. and Roeder, G. S. (1989). Yeast mer1 mutants display reduced levels of meiotic recombination. Genetics *121*, 237-47.

Engebrecht, J. and Roeder, G. S. (1990). MER1, a yeast gene required for chromosome pairing and genetic recombination, is induced in meiosis. Molecular and Cellular Biology *10*, 2379-89.

Frank, J. (1992). Electron tomography : three-dimensional imaging with the transmission electron microscope. (New York: Plenum Press).

Fung, J. C., Liu, W., deRuijter, W. J., Chen, H., Abbey, C. K., Sedat, J. W. and Agard, D. A. (1996). Toward fully automated high-resolution electron tomography. Journal of Structural Biology *116*, 181-9.

Game, C. J., Zamb, T. J., Braun, R. J., Resnick, M. and Roth, R. M. (1980). The role of radiation (rad) genes in meiotic recombination in yeast. Genetics *94*, 51-68.

Gillies, C. B. (1973). Ultrastructural analysis of maize pachytene karyotypes by three dimensional reconstruction of the synaptonemal complexes. Chromosoma *43*, 145-176.

Golubovskaya, I. N. and Mashnenkov, A. S. (1976). Genetic control of meiosis II. A desynaptic mutant of corn induced by N-nitroso-N-methylurea. Genetika *12*, 7-14.

Golubovskaya, I. N. and Urbach, V. B. (1981). Allelic relationships between maize meiotic mutations with similar disturbances of meiosis. Genetika *17*, 1975-1982.

Hayat, M. A. (1981). Principles and techniques of electron microscopy : biological applications. (Baltimore: University Park Press).

Hollingsworth, N. M. and Byers, B. (1989). HOP1: a yeast meiotic pairing gene [published erratum appears in Genetics 1989 Jul;122(3):719]. Genetics *121*, 445-62.

Hollingsworth, N. M., Goetsch, L. and Byers, B. (1990). The HOP1 gene encodes a meiosis-specific component of yeast chromosomes. Cell *61*, 73-84.

Horowitz, R. A., Agard, D. A., Sedat, J. W. and Woodcock, C. L. (1994). The three-dimensional architecture of chromatin in situ: electron tomography reveals fibers composed of a continuously variable zig-zag nucleosomal ribbon. Journal of Cell Biology *125*, 1-10.

Kaneko, Y. and Walther, P. (1995). Comparison Of Ultrastructure Of Germinating Pea Leaves Prepared By High-Pressure Freezing-Freeze Substitution And Conventional Chemical Fixation. Journal Of Electron Microscopy *44*, 104-109.

Kiss, J. Z. and McDonald, K. (1993). Electron microscopy immunocytochemistry following cryofixation and freeze substitution. Methods in Cell Biology *37*, 311-41.

Klapholz, S., Waddell, C. S. and Esposito, R. E. (1985). The role of the SPO11 gene in meiotic recombination in yeast. Genetics *110*, 187-216.

Kleckner, N. (1996). Meiosis: how could it work? Proceedings of the National Academy of Sciences of the United States of America *93*, 8167-74.

Kleckner, N., Padmore, R. and Bishop, D. K. (1991). Meiotic chromosome metabolism: one view. Cold Spring Harbor Symposia on Quantitative Biology *56*, 729-43.

Loidl, J. (1990). The initiation of meiotic chromosome pairing: the cytological view. Genome *33*, 759-78.

Maguire, M. P. (1978). Evidence for separate genetic control of crossing over and chiasma maintenance. Chromosoma *65*, 173-183.

Maguire, M. P. (1978). A possible role for the synaptonemal complex in chiasma maintenance. Experimental Cell Research *112*, 297-308.

Maguire, M. P., Paredes, A. M. and Riess, R. W. (1991). The desynaptic mutant of maize as a combined defect of synaptonemal complex and chiasma maintenance. Genome *34*, 879-87.

Maguire, M. P., Riess, R. W. and Paredes, A. M. (1993). Evidence from a maize desynaptic mutant points to a probable role of synaptonemal complex central region components in provision for subsequent chiasma maintenance. Genome *36*, 797-807.

Mcdonald, K. and Morphew, M. K. (1993). Improved Preservation Of Ultrastructure In Difficult-To-Fix Organisms By High Pressure Freezing And Freeze Substitution .1. Drosophila-Melanogaster And Strongylocentrotus-Purpuratus Embryos. Microscopy Research And Technique *24*, 465-473.

McEwen, B. F., Arena, J. T., Frank, J. and Rieder, C. L. (1993). Structure of the colcemid-treated PtK1 kinetochore outer plate as determined by high voltage electron microscopic tomography. Journal of Cell Biology *120*, 301-12.

Menees, T. M. and Roeder, G. S. (1989). MEI4, a yeast gene required for meiotic recombination. Genetics *123*, 675-82.

Menees, T. M., Ross-MacDonald, P. B. and Roeder, G. S. (1992). MEI4, a meiosis-specific yeast gene required for chromosome synapsis. Molecular and Cellular Biology *12*, 1340-51.

Moritz, M., Braunfeld, M. B., Fung, J. C., Sedat, J. W., Alberts, B. M. and Agard, D. A. (1995). Three-dimensional structural characterization of centrosomes from early Drosophila embryos. Journal of Cell Biology *130*, 1149-59.

Nelson, O. E. and Clary, G. B. (1952). Genic control of semi-sterility in maize. J. Hered. *43*, 205-210.

Rockmill, B. and Roeder, G. S. (1990). Meiosis in asynaptic yeast. Genetics *126*, 563-74.

Roeder, G. S. (1995). Sex And The Single Cell - Meiosis In Yeast. Proceedings Of The National Academy Of Sciences Of The United States Of America *92*, 10450-10456.

Samuels, A. L., Giddings, T. H., and Staehelin, L. A. (1995). Cytokinesis in tobacco BY-2 and root tip cells: a new model of cell plate formation in higher plants. Journal of Cell Biology *130*, 1345-57.

Schmekel, K., Skoglund, U. and Daneholt, B. (1993). The three-dimensional structure of the central region in a synaptonemal complex: a comparison between rat and two insect species, Drosophila melanogaster and Blaps cribrosa. Chromosoma *102*, 682-92.

Schmekel, K., Wahrman, J., Skoglund, U. and Daneholt, B. (1993). The central region of the synaptonemal complex in Blaps cribrosa studied by electron microscope tomography. Chromosoma *102*, 669-81.

Studer, D., Hennecke, H. and Muller, M. (1992). High-Pressure Freezing Of Soybean Nodules Leads To An Improved Preservation Of Ultrastructure. Planta *188*, 155-163.

Sym, M., Engebrecht, J. A. and Roeder, G. S. (1993). ZIP1 is a synaptonemal complex protein required for meiotic chromosome synapsis. Cell *72*, 365-78.

Sym, M. and Roeder, G. S. (1994). Crossover interference is abolished in the absence of a synaptonemal complex protein. Cell *79*, 283-92.

Sym, M. and Roeder, G. S. (1995). Zip1-induced changes in synaptonemal complex structure and polycomplex assembly. Journal of Cell Biology *128*, 455-66.

von Wettstein, D., Rasmussen, S. W. and Holm, P. B. (1984). The synaptonemal complex in genetic segregation. Annual Review of Genetics *18*, 331-413.

Westergaard, M. and von Wettstein, D. (1972). The synaptinemal complex. Annual Review of Genetics *6*, 71-110.

Winey, M., Mamay, C. L., O'Toole, E. T., Mastronarde, D. N., Giddings, T. H. J. r., McDonald, K. L. and McIntosh, J. R. (1995). Three-dimensional ultrastructural analysis of the Saccharomyces cerevisiae mitotic spindle. Journal of Cell Biology *129*, 1601-15.

Chapter 3 :

Higher Order Chromatin Structure

Summary

My original plan for my thesis research focused on characterizing the "large scale" structures representing the higher levels of organization in the chromosome folding process. One such large scale structure is the 1300 Å fiber which has been identified as an intermediate fiber in the folding pathway of the mitotic chromosome (Belmont et al., 1987). My research was centered on examining the folding pattern of the 300 Å fiber within this 1300 Å fiber, first in Hela and then in Zea mays meiocytes using electron microscope (EM) tomography and three dimensional (3-D) image processing techniques. A wide range of sample preparation conditions and image enhancement algorithms were systematically tried in an effort to characterize this folding. The one clear result of this work was that the large scale organization of chromatin is made up of fibers with widths in the range of 150-250 Å and not 300 Å, for both the chromatin from Hela and maize. Unfortunately, it was not possible to trace the path of these 200 Å fibers so no conclusive results were obtained for the internal organization of the 1300 Å fiber, but a summary of this work will be presented in this thesis for use as a guideline in the future for others pursuing similar goals.

Introduction

The fully condensed mitotic chromosome arises from a series of hierarchical folding steps representing a 10,000-fold linear compaction of DNA. The initial steps of this process involve the formation of "lower order" structures which include the winding of DNA around nucleosomes, the formation of the nucleosome "beaded filament" (100 Å fiber) and the folding of the 100 Å fiber into a 300 Å fiber. The levels of linear compaction accounted for by these initial steps represent only a 42-fold packing ratio out of the total 10,000. The remaining 250-fold compaction is taken up by the creation of "higher order" or "large-scale" structures in which the 300 Å fiber is further folded into large domains which then undergo additional organization to give rise to the final levels of condensation. Unlike the lower order structures which have been well characterized by electron

microscopy (Olins and Olins, 1974), crystallography (Richmond et al., 1984), fiber diffraction (Widom and Klug, 1985; Langmore and Paulson, 1983), and biochemical procedures such as nuclease digestion (van Holde, 1989), a complete characterization of the higher order structures is still lacking.

Much of the difficulty in characterizing the higher levels of the mitotic chromosome is due to the complex 3-D pattern of the folding and the compact state of the large scale structures. Many attempts have been made to reduce the complexity of the problem by greatly perturbing the mitotic chromosome to reduce the level of compaction and observing the resulting structures in the electron microscope (Marsden and Laemmli, 1979; Wray et al., 1978). By approaching the problem in this manner, important information about the 3-D spatial relationships between the fibers is lost. In addition, questions arise as to the relevance of the resulting structures to actual structures of an intact chromosome.

To avoid these problems, we started with fresh approach designing experiments to preserve chromosome structure, keeping it as close to its native state as possible. Instead of unraveling the chromosomes, we employed electron tomography (Frank, 1992), intermediate voltage electron microscopy (IVEM), and image processing techniques to get a clearer view of the complex nature of the folding pathway of chromatin in its nuclear environment.. The combination of these three techniques provides several advantages over more conventional methods. With IVEM, the penetration power of the higher energy electrons allows thick sections incorporating entire large scale structures to be imaged. By imaging these thick sections at several tilt angles in the intermediate voltage transmission microscope, we can obtain micrographs which are projections of the thick sections at each respective tilt angle. From these projections, tomographic reconstruction techniques can be employed to create a 3-D representation of the large scale structure contained within the thick section. This eliminates the problem encountered in earlier studies that arises from trying to interpret a 3-D structure from only 2-D micrographs. Finally, since images are collected on a high quality charged coupled device (CCD), data exists in a digital format

that is readily accessible to image processing techniques. In this form, the images are subject to computational dissection and are easily displayed on computer graphics systems. Such imaging processing techniques aid in the interpretation of chromatin architecture by computationally reducing the complexity of the image through the enhancement of the relevant features from the background and by allowing direct tracing of the fibers through modeling of the folding pathway within the large-scale chromatin fiber.

Reconstructing a chromosome in its native state requires determining conditions which preserve chromosomal integrity. Correlative light and electron microscopic studies (Belmont et al., 1989), together with earlier work analyzing chromosome birefringence (Sedat and Manuelidis, 1978), have been carried out to determine the appropriate buffer, fixation, and isolation conditions. Under such conditions, intermediate structures representative of discrete folding domains were found. These domains were shown to have distinct widths of 240 (300 Å), 400-500, 800-1000, and 1200-1400 Å. The most prominent of these structures was the 1200-1400 Å domain (1300 Å fiber). From this result, our lab has postulated that the formation of the mitotic chromosome involves a progressive association of the smaller domains into larger domains. A proof of this statement requires further studies exploring the underlying organization of the large scale structures. Therefore, the goal of this work was to characterize the internal architecture of a 1300 Å fiber using the methods described above. We had chosen to model this fiber in telophase HeLa nuclei and in prophase of the Zea mays meiocyte to take advantage of the naturally decondensed state of the chromatin at these particular stages of the cell cycle. We were able to recognize in our initial tomographic reconstructions the underlying 150-250 Å fibers. Attempts to model the 150-250 Å fibers throughout the 1300 Å structure demonstrated that we could trace segments of the underlying fiber over considerable distances. However this ability is limited to those segments of the fiber which are slightly separated from the majority of the dense fibrous core.

Results

It is clear from initial studies (Belmont et al., 1987) that tomographic reconstruction can provide a means by which to comprehend the underlying structures forming the mitotic chromosome. Nevertheless, additional efforts are needed to optimize this procedure so that the entire organization of the large scale 1300 Å fiber can be revealed. We took a multi-level approach to this problem focusing on four general directions: 1) Improving the tomography by revising data collection conditions and by employing new and better reconstruction algorithms. 2) Using recently developed image processing techniques to enhance relevant chromosome features. 3) Using reversible or natural decondensation to slightly separate the individual fibers without significantly affecting chromosome integrity. and 4) Improving contrast by either developing chromatin specific stains or finding methods to further reduce the background staining.

Experimental Approaches Toward Improving The Tomographic Method

The large depth of focus of the electron microscope results in the formation of an image which is in effect a 2-D projection of the entire thick section containing the sample. From the Fourier slice theorem (Kak and Slaney, 1988), the projection of an object can be regarded as a 2-D slice in the 3-D Fourier tranform of that object at the particular angle that the projection was taken. This theorem is the key to all tomographic imaging since we can now relate the series of projections taken at different angles directly to the Fourier transform of our imaged object.

In EM tomography, the range of tilt angles should span +/- 90 degrees to completely sample the object. However with the increasing tilt angles, there exists an comcomitant increase in the path length that a electron must travel through a section. This in turn gives rise to multiple scattering events which are incoherent electron specimen interactions that distort the relationship between measured image intensity and the projected specimen mass density that is the basis for the tomographic reconstruction (Han et al.,

1995) Thus only a limited range of tilt angles(+/- 80 degrees in our system) can be collected resulting in a "missing wedge" of information in the object. This missing wedige of information results in an approximately 2-fold or greater reduction in resolution in the z-axis as compared to the resolution in x and y. In our initial reconstruction, a R(resolution)-weighted backprojection scheme (Frank, 1992) was used to reconstruct the projections into a 3-D representation of the 1300 Å fiber. This algorithm involves taking projections, filtering them, and then smearing them back along rays defined by the projection angle. A drawback to this reconstruction scheme is that it does not attempt to approximate the missing wedge of information given some a priori knowledge about the region.

One direction we took to improve the quality of the final reconstruction was to implement a newly developed iterative algorithm in which a positivity constraint (Youla and Webb, 1982) is applied. Since an image cannot have negative values, applying a positivity constraint restrains the reconstruction to reflect the more realistic condition. In addition, this new algorithm includes methods to reduce the data from surrounding objects, which at high tilts, contribute spurious information to the projection. Other improvements on the initial reconstruction include extending the data collection range to the full +/- 80 degrees instead of the +/- 60 degrees of the original data set, taking double exposures and setting the gain to improve the counting statistics, and keeping the beam intensity constant in order to better standardize the conversion of intensity into mass density. The cummulative effect of these changes resulted in better reconstructions but this was not quite enough to allow the tracing of the internal architecture. Although we could not find a way to trace pathways in the chromatin, we were able to determine that the majority of the internal fibers were of the 150 - 250 Å width rather than the 300 Å width as previously thought.

Use of Image Processing Techniques

To follow the pathway of fibers through a 3-D object requires the capability to quantitatively manipulate the reconstructed image. Within the lab, several methods of

image enhancement had been developed to aid in interpreting the reconstruction. Local constrast enhancement is one such method which we used enhance relevant chromosome features. Using the local contrast enhancement approach, the 150-250Å fiber definition became clearer through the reduction of the contribution to the image by the nucleoplasm background. The improvements using local contrast enhancement schemes are subtle due to the inherently low contrast of the reconstruction where only 5-10% changes in contrast levels were seen between relevant features. So as an alternative method to further define the fibers from the nucleoplasm background, we attempted to implement newly developed image segmentation routines based on gradient detection and region delimitation techniques in order to computationally reduce the complexity of the images. Again an improvement could be seen in fiber definition. It is clear that both of these schemes can simplify the image however without an outside criteria such as symmetry to judge the effect of the image processing it was difficult to assess whether the image had been over-manipulated. Additionally, by reducing the image to a more skeletonized structure, we often lost the continuity needed to trace structures throughout the reconstruction. Thus, although we were able to implement many of the image enhancement algorithms providing improved identification of fibers only short regions of the chromatin fiber pathways could be traced (300-500 Å) before continuity was lost due both to possible over image processing and the reduced resolution in the z-axis due to the missing wedge. More powerful image processing methods, based on modern techniques such as wavelet transforms and maximum entropy should overcome both these problems, while segmentation analysis is likely to provide ever greater assistance in interpreting these complex 3-D images.

Experimental Approaches to Decondensation

Another approach was to produce minor changes in chromosome condensation in order to decrease the compactness of the fibers enough to observe the fiber paths clearly. It has been shown previously that large decreases in polyamine concentration in the buffer

can dissociate the large scale structures into 300 Å fibers (Belmont et al., 1989). Further reduction of polyamines results in the entire chromosome unraveling into the 100 Å fiber. This process is known to be reversible; by returning chromosome preparations to normal polyamine levels, the normal distribution of sizes for the higher order structures is restored. Thus we believed these changes to be compatible with native structure. By controlling decondensation with polyamine titrations, it was thought to be possible to decrease the compactness of the 1300 Å enough to improve our ability to follow the course of the 300 Å fibers. However, the results showed that the change in condensation did not reflect a gradual unraveling of structures but resulted in an overall decondensation of the chromatin into 100 Å fibers evenly spaced in the 1300 Å fiber making it impossible to use this method for its intended purpose.

Another approach for observing decondensed chromosomes was to examine a different system where the chromosomes are already naturally less compact. The advantage of this type of study is that it would have precluded questions about the reliability of the structure due to unnatural perturbations. One such system is the prophase I stage in maize meiocytes. There are 5 substages of prophase I: leptotene, zygotene, pachytene, diplotene and diakinesis. From leptotene onwards, there is a gradual condensation of the chromatin which could be followed due to the fact that these stages were observed in maize anthers where increasing anther size correlated to progression of prophase I.

As part of this study, we devised a method to prepare meiocytes for examination by electron microscopy. Although normal chemical fixation worked well for the pachytene stages of the meiocytes, earlier stages were difficult to prepare by this method since this method required the extrusion of meiocytes after the initial fixation. The physical damage from this extrusion was minimal in pachytene staged anthers due to the increased buildup of the cell wall which protected the meiocytes; in earlier stages, cell wall formation is just beginning and does not provide enough protection to the meiocytes from the forces of the

extrusion. So an alternative method, high pressure freezing (Dahl and Staehelin, 1989) with freeze substituion (McDonald and Morphew, 1993), was used to prepare these earlier stages of prophase I where the chromatin was more likely to be decondensed. (for details see Chapter 3). Using this method, anthers or pairs of locules making up the anther could be fixed chemically in their entirety while in a frozen state. The improved fixation was indicated by the better preservation of the nuclear membranes which were smooth and exhibited the double bilayer of membranes. Little or no extraction of the cytoplasm was observed; generally in chemical fixation extraction is seen indicating poor fixation in those regions. In general, this quality of preservation of structure was seen in 5-10% of the anthers observed. In all other cases, ice damage was a major problem and caused the loss of structural integrity. However when no ice formation was evident, the high pressure freezing method preserved the maize anthers at these earlier stages well and often better than what was generally seen for chemical fixation. (see Chapter 3 for methods)

Once preservation schemes were established, all stages of prophase I were examined to determine the level of chromatin condensation. Representative regions of the chromatin were reconstructed for every stage and examined for our ability to trace the underlying chromatin fibers. Again, 150-250 Å fibers dominated the architecture of the large scale fibers.. The zygotene and pachytene stages were too condensed for analyzing the pathways of the fibers only 500 Å could be traced before ambiguity in connectivity were encountered. Leptotene looked the most promising with most of its chromatin still in a decondensed stage. However at this level of decondensation, the chromatin was difficult to discern from the high background of the nucleoplasm. In the end, it was not possible to analyze the folding even in a naturally decondensed state with the current techniques at my disposal. However, in the future if any chromatin specific stains for the electron microscope are developed, the leptotene chromatin configuration should be examined first.

Experimental Approach For Contrast Enhancement

Contrast in the transmission electron microscope for biological specimens is generated by the heavy metal stains applied to the sample. Previous reconstructions used a combination of uranyl acetate, lead citrate, and osmium tetroxide to stain the chromosomes. Although these stains were not chromosome specific, occasionally non-specific staining was reduced by detergent extraction of background material. Another approach was to develop a chromosome specific label which led to preliminary experiments to determine if undecagold (Safer et al., 1986) can be used to provide a chromatin specific stain. Undecagold is 8.2 Å in diameter, has a molecular weight of approximately 5000, and can be attached to sulfhydryl groups through a maleimide linkage. One idea that we wanted to explore was whether we could attach undecagold directly to histones which would incorporate into chromosomes during replication directly locating the stain to the chromatin. A similar approach using fluorescent labels showed that histones can be routinely labeled with fluorescent probes and injected into *Drosophila* embryos to be incorporated into chromosomes. Once incorporated, these fluorescent histones act as a chromatin specific dye in the optical microscope. This type of labeling was attempted for undecagold to see if by attaching it to histones, we could image Drosophila chromsomes in the same way but in the electron microscope. Through exhaustive attempts at getting undecagold to work as a chromatin stain, we found that undecagold was not suitable for this purpose mainly because the undecagold did not provide sufficient contrast or incorporate at high enough density to be used as a stain.

Discussion

The original aim of my proposal was to determine the organization of the 1300 Å fiber in the HeLa telophase nuclei by the use of EM tomography. Because of difficulties with fiber compactness, several methods were employed to aid in revealing the continous pathways of fibers in the large scale structure. Attempts were made to find a chromatin

specific stain, use improved data collection, reconstruction and image processing techniques and use less condensed chromatin preparations to improve methods towards characterizing the folding. Even with these improvements, it was still quite difficult to resolve individual fiber traces. In the end, although much was learned in the process of trying to assess the levels of chromatin organization, a final answer to the question will require more powerful reconstruction and image processing methods to be developed.

References

Belmont, A., Sedat, J.W., and Agard, D.A. (1987). A three-dimensional approach to mitotic chromosome structure: evidence for a complex hierarchical organization. J. Cell Biol. *105*, 77-92.

Belmont, A.S., Sedat, J.W., and Agard, D.A. (1989). Large-scale chromatin structural domains within mitotic and interphase chromosomes in vivo and in vitro. Chromosoma *98*, 129-143.

Dahl, R. and Staehelin, L. A. (1989). High-Pressure Freezing For The Preservation Of Biological Structure - Theory And Practice. Journal Of Electron Microscopy Technique *13*, 165-174.

Frank, J. (1992). Electron tomography : three-dimensional imaging with the transmission electron microscope. (New York: Plenum Press).

Han, K. F., Sedat, J. W. and Agard, D. A. (1995). Mechanism Of Image Formation For Thick Biological Specimens - Exit Wavefront Reconstruction And Electron Energy-Loss Spectroscopic Imaging. Journal Of Microscopy-Oxford *178*, 107-119.

Kak, A.C., and Slaney, M. (1988). In Principles of Computerized Tomographic Imaging. p.57.

Langmore, J.P., and Paulson, J.R. (1983). Low angle x-ray diffraction studies of chromatin structure in vivo and in isolated nuclei and metaphase chromosomes. *J.* Cell Biol. *96*, 1120-1131

Marsden, M.P.F. and Laemmli, U.K. (1979). Metaphase chromosome structure: evidence for a radial loop model. Cell *17:8*, 49-858.

Mcdonald, K. and Morphew, M. K. (1993). Improved Preservation Of Ultrastructure In Difficult-To-Fix Organisms By High Pressure Freezing And Freeze Substitution .1. Drosophila-Melanogaster And Strongylocentrotus-Purpuratus Embryos. Microscopy Research And Technique *24*, 465-473.

Olins, A.E., and Olins, D.E. (1974) Spheroid chromatin units (v bodies) Science *183*, 330-332.

Richmond, T.J., Finch, J.T., Rushton, B., Rhodes, D. and Klug, A. (1984). Structure of a nucleosome core particle at 7 Å resolution. Nature *311*, 532-537.

Safer, D., Bolinger, L., and Leigh, J. (1986). Undecagold clusters for site-specific labeling of biological macromolecules: simplified preparation and model applications. Journal of Inorg. Biochem. *26*, 77-91.

Sedat, J.W., and Manuelidis, L. (1978). A direct approach to the structure of the eukaryotic chromosomes. Cold Spring Harbor Symp. Quant. Biol. *42*, 331-350.

van Holde, K.E. 1989. In Chromatin. p.219-305.

Widom, J., and Klug, A. (1985). Structure of the 300 Å chromatin filament: x-ray diffraction from oriented samples. Cell *43*, 207-213.

Wray, W., Mace, M., Daskal, Y., and Stubblefield, E. (1978). Metaphase chromosome architecture. Cold Spring Harbor Symp. Quant. Biol. *42*, 361-365.

Youla, D.C., and Webb, H. (1982). Image restoration by method of convex projections: Part 1-Theory. *I*EEE Transaction on Medical Imaging *MI-1*, 81-94.

Chapter 4 :

Automation of Electron Tomographic Data Collection

Summary

Electron tomography is a powerful tool in elucidating the three-dimensional architecture of large biological complexes and subcellular organelles. Its use can be expanded through the simplification of the tomographic procedure by automation of its tasks. In this chapter, we describe our EMACT/EMCAT system which automates both tomographic data collection and reconstruction.

Introduction

In 1968, the bacteriophage T4 tail was first reconstructed demonstrating that tomography, a method which constructs a three-dimensional (3-D) object from its projections, could be used for analyzing macromolecular and supramolecular structures.(Klug, 1968) The introduction of intermediate voltage electron microscopes further extended the technique by providing the means to examine very large and non-symmetrical subcellular organelles, at resolutions beyond what would be possible using light microscopy. Recent studies using electron tomography on a variety cellular organelles and assemblies such as centrosomes (Moritz et al., 1995), kinetochores (McEwen et al., 1993) and chromatin (Woodcock et al., 1994), have clearly demonstrated the power of this technique for obtaining 3-D structural information on non-symmetric cell components. When combined with biochemical and molecular observations, these 3-D reconstructions have provided significant new insights into biological function.

Although the information that tomography provides is unique, its use as a general tool in the biological community has been sparse. Perhaps the most important drawback has been the requirement for an intimate knowledge of the entire tomographic process from data collection to the reconstruction. Tomographic data collection requires the collection of a large number of tilted views of the same sample (typically > 100) at fine tilt intervals (< 1.5°) covering an angular range in excess of ± 60°. Because it is impossible the make the sample perfectly eucentric, specimen tilting results in both an X-

Y translation and an alteration in focus. Thus each image has to be re-centered and re-focused. In addition, the images must be converted to digital form and precisely aligned with one another before the reconstruction can be calculated. Not surprisingly, this is an extremely exacting and labor-intensive procedure.

Recently, efforts have been made to simplify parts of tomography through the development of automated data collection systems (Dierksen et al., 1992; Koster et al.,1993). These systems automate the tilting, translating, focusing and picture-taking steps that make up a typical data collection. If done manually, this process is both time-consuming due to the large number of images needed to be collected and also, suboptimal because of the high dose to which the sample is exposed during the execution of these actions. With an automated data collection a marked reduction in both time and dose is achieved (Braunfeld et al., 1994; Koster et al., 1992) improving the quality of the data collected.

Our approach to simplifying and integrating the entire process has been to combine all aspects of a tomographic study: data collection, reconstruction, and image interpretation within one system. With our system, both data collection and reconstruction are automated to make tomography more approachable to the average user. Ease, reliability and speed have been emphasized. In this paper we describe our automated EMACT/EMCAT system for data collection and reconstruction. The EMACT/EMCAT system was developed using the IVE image visualization environment (Chen et al., 1996) which also makes up our image interpretation system .

EMACT (Electron Microscopic Automated Computerized Tomography)

The ability to automate tomographic data collection has depended on the development of autotuning methods (Erasmus and Smith, 1982; Saxton et al., 1983) which allow for automatic measurement and setting of image parameters for the

transmission electron microscope (TEM). Through the autotuning process, deviations from ideality in these parameters reveal themselves as image displacements which can be accurately measured through cross-correlation approaches. Over the years, refinements were made to incorporate beam-tilt induced shift measurements (van der Mast, 1984; Nomura and Isamozwa, 1987; Koster et al., 1987) which are now a standard part of today's automated tomography systems (Dierksen et al., 1992; Koster et al., 1992,1993). To a large extent, the reliability of autotuning depends on the accurate calibration of the microscope controls. Typically, calibration matrices are determined for beam shift, image shift and focus and take into account all linear relationships between the controls and the TEM parameters values. Of equal importance is the use of digital recording devices such as a CCD camera which possess the linearity, dynamic range, and sensitivity needed to collect images from objects that are low in contrast and demand minimal beam irradiation.

For EMACT, the autotuning methods along with other generalized functions are an integral part of the tomography package and will discussed before the actual design and implementation of the tomographic collection is described. Much of what will be presented for the software environment will also apply as well to the general platform upon which our reconstruction system, EMCAT, is built.

Instrumentation The system is built around a Phillips EM430 intermediate voltage TEM (300 kv/ LaB6) with a Phillips C400 microscope/computer interface unit providing a link to all the TEM's functions. Images are acquired through a prototype12 bits/pixel cooled (-35^0 C) slow scan CCD camera attached to a Photometrics controller (Thompson CCD chip 1024^2 pixels and 19 x19 um) with a readout rate of 2×10^6 pixels/s. Imaging control, display and processing were built around a Personal IRIS 4D35 (Silicon Graphics, Sunnyvale) workstation. For fast image acquisition and cross-correlation calculations, we use a 4 processor Shamrock array processor providing 320 Mflops (SKY Computers Inc.).

II. General Software Design

File Management Since a reconstruction data set can range from 50 to 200 Mbytes of data, it is important to give careful consideration to the file format chosen to manage the data. The most essential criteria are 1) that there exists a single header that is a part of the same file as the data, and 2) that the 3-D data set itself is entirely contained in one file. The MRC-variable length extended header format satisfies these requirements. The 1024 byte header contains most of the geometric and physical contents of the file. This is followed by an extended header which for tomography contains specialized information associated with each image section such as tilt and image shifts values. Extended header information is useful both for the later processing steps and for the automated data collection where the ability to restore the data collection conditions of the previously collected section is needed. The end of the extended header marks the beginning of the data storage space. Each data section representing a 2D image is stored consecutively within the file "stack". Random access to the each section, some sections or part of a given section is available through interpretation of the stored header.

Image Visualization Environment Fig. 1 illustrates the typical data collection layout created with the IVE. Four windows are each assigned a unique role in the data collection process. Window(W) 1 displays only images written out to the data file. Because of the adjustable depth size assigned to W1, each image in the data stack can be viewed by scrolling through sections stored in this window. Automation of data collection makes this feature necessary in order to provide a history of collected images for the operator who is not always present . In contrast, W2 is primarily devoted to images that are acquired but not written to disk. Typically, images taken for use in the automatic determination of both focus and tracking are directed to this window. The process of cross-correlating two images plays an integral role in the automation of tomography. Both W3 and W4 were designed take part in this process; whereas W3 accepts images from W1 or W2 as references for cross-correlation, W4 displays a

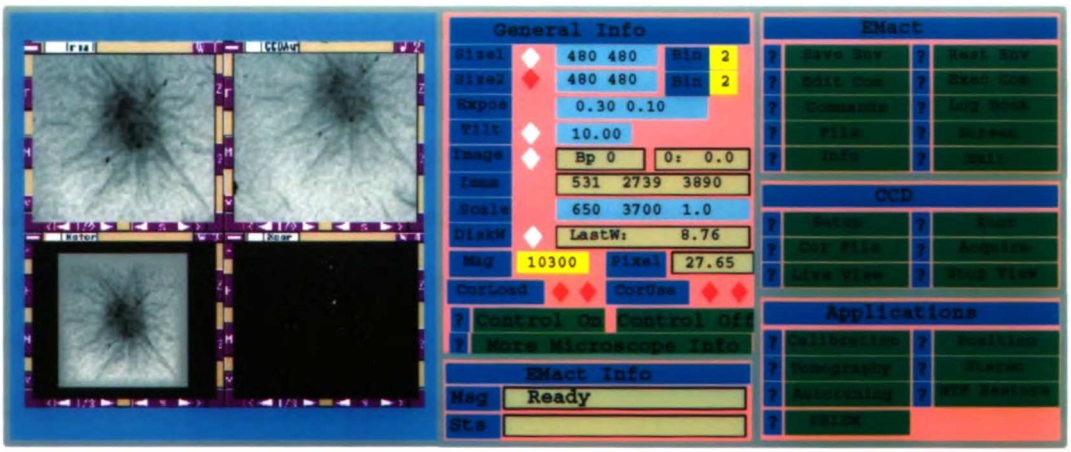

Figure 4.1 EMact window and menu layout for a typical data collection. The upper left window displays the lasted saved image. The upper right window, W2, shows that the sample has drifted from the center of the image. W3, bottom left window, holds the reference image which will be used for cross-correlation purposes during the automated tracking steps. In W4, bottom right, the peak obtained from cross-correlating images in W2 and W3 is depicted indicating the amount of image shift/drift to be corrected. Shown to the right of the windows are the menus containing most of the data collection functions. For clarity these text windows which would normally run down the righthand side of the screen have been signficantly enlarged.

pictorial representation of the cross-correlation peak. In addition to allow for easy operation of the data collection program, a menu based format was developed for all functions. This type of format provides a way to group functions in a simple and clearcut fashion for the user. Selection of functions in the menu are made convenient through interactions with a mouse or a button box. In addition, color cues are used to indicate the particular status of the different elements in the menu. Whether an element contains help information, can be edited, used for updating the general status, or toggled on or off, are all indicated by the color assigned to the element. Default values are provided for all possible inputs meanwhile customized environments specifying individual parameters, current filenames, and window and menu placement can also be saved and restored at any time.

III. Autotuning and Generalized Functions

Correction and Calibration Files Within EMACT, applications were created for the easy correction of CCD camera inhomogeneities as well as for the straightforward calibration of the TEM parameters for beam shift, image shift and defocus. Since the method for CCD corrections and TEM parameter calibrations have been well reviewed in previous work (Koster, 1992) only a brief discussion about the method will ensue. Simply stated, the gain and offset, of each pixel is determined and stored in a "correction" file. The gain of each pixel is obtained by determining its intensity over a series of exposure times whereas the offset is calculated from the mean of a series of dark current readings. Abnormally responding pixels are identified and corrections for all pixels are applied as the data is acquired. The second file, termed the "calibration" file, is created by measuring the image displacements induced by changing each of the TEM parameters by a known quantity. These measurements are used in the creation of the calibration matrices which determine the amount of "counts" applied to a TEM parameter to correct a measured image displacement.

Image Positioning and Focusing Once the appropriate calibration and correction files have been obtained, automatic adjustment of image positions and focus are made possible. By simply using a cursor to select first the current position of a feature in an image and then the position on the image where it is to be moved, the image will be translated to the new spot through adjustments in the beam shift and image shift coils determined by the distance between the two positions and the conversion from the calibration file. Note that the beam shift adjustments are not required for the actual image shifting but instead are needed to ensure that the illumination remains centered on the image after the shift. Another way to adjust image position is through cross-correlation of one image to another. This has proven to be a excellent way to align images automatically and thus is the method used for image tracking in the data collection. Focusing information can also be obtained using the cross-correlation of images. A method similar to many TEM's wobbler function can be used to determine the amount of defocus. Basically, the amount of image shift measured between a pair of images recorded with opposite signs of induced beam tilt is dependent on defocus. At perfect focus the image shift is zero between the beam tilted images. From this information and the focus calibration file, the defocus can be determined and adjusted accordingly.

More GeneralFunctions For a tomography system to be complete, additional functions which permit ease in scanning and aid in image analysis are needed. We have incorporated a stereo viewing function to automatically acquire stereo pairs of an image. To aid in recording larger areas than permitted by the limitations of the CCD field, a montage function has also been added. The montage function takes a series of partially overlapping views in order to construct a larger combined image. This can be done automatically by specifying either the required image shifts or the desired combined size. Later, a cross-correlation method is used to merge the overlapping images. The processing options that are available in EMACT include all those from Prism (Chen,

1995); FFT, fast fourier transforms and a MTF function which corrects the modulation transfer function of the CCD camera.

IV. Automated Data Collection

Much consideration was given to the design of the automated tomography system. One concern was to make the system accessible to the general biological community so that within one training session, it would be possible for novice users to collect a reconstruction set virtually without supervision. At the same time, the design should include enough flexibility for more knowledgeable users to explore less standard approaches to data collection. Keeping all this in mind, a dedicated tomography application was created to handle most standard single-axis tomography collection schemes. For more complicated data collection protocols, a macro or script execution file can be written using the available microscope command language to customize the collection scheme to a user's individual specification.

Dedicated Tomography Collection As can be seen in in Fig 2A., data collection consists of a series actions that are repeated for each tilt. The series begins with setting the angle by a given increment which is then followed by two focusing actions. Induced beam tilts are used to deduce the level of defocus. Focus is then set to the value indicated in the tomographic setup options. The focus action is repeated twice to attain an accuracy of 1% of the requested value. Normally, a sample is made as eucentric as possible so focusing can be performed before tracking of the image shift is needed. However, since perfect eucentricity cannot be attained due to specimen drift and the mechanical limits of the goniometer, tracking actions are required after a tilt is made to align the new image to the previous saved image. For this reason, two tracking steps are needed after focusing. As stated, cross-correlation is used for tracking the images in the tomography data collection, however since the images are obtained at different tilts, a stretching factor is applied to the appropriate image to reduce the broadening of the correlation peak due to the difference in tilt angle. To maximize dynamic range, the optimal exposure for the

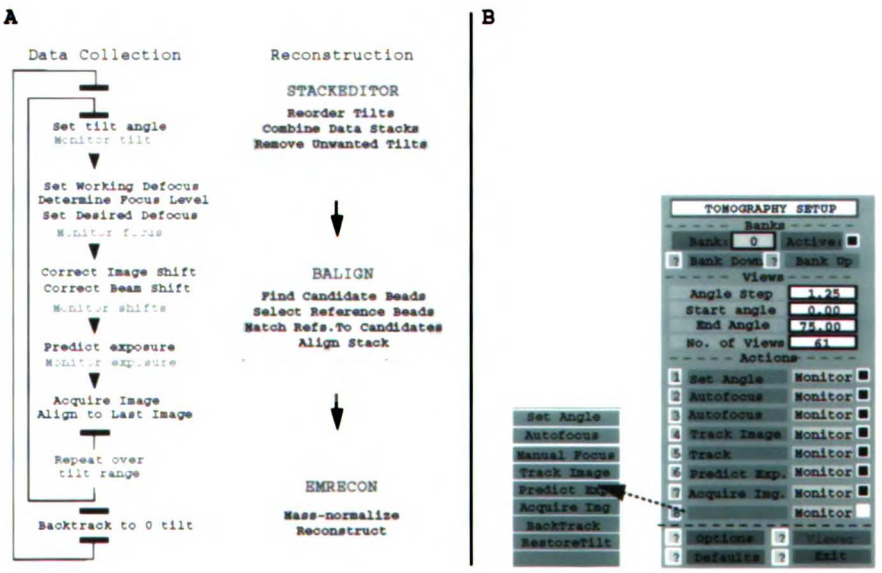

Figure 4.2 (A) Outline of the sequence of steps for the data collection and reconstruction. (B) Tomography Data Collection Bank. Each bank in the data collection specifies a series of actions to be taken within a given tilt range. The bank setup allows the user to rapidly select the order of actions from a menu pulldown indicated by the arrow. Whether the actions are monitored to look for potential errors is determined by the toggle buttons next to the selected action. Up to 10 banks can be specified.

final is predicted based on information from a previously measured tracking image. Finally the image is taken by two successive exposures which are compared to correct for random X-ray events and combined to minimize noise. Before writing out, one last cross-correlation of the image to the previously saved image is performed.

Functions to monitor the behavior of the data collection are embedded in the all of the collection routines. Values such as tilt, maximum or minimum intensity, and image shift displacements are all checked to make sure each of the values falls within an expected range, otherwise, an error message is sent and the data collection is paused until further operator instructions. The pause is arranged so that an action finishes before the data collection is temporarily stopped. This arrangement prevents leaving the microscope settings in a difficult to recover state. A log is provided to display all actions as they happen so that the operator can ascertain the reason for an error and take steps to rectify the problem. Problems can be dealt with either by using a function to resume the next action, in cases where the problem can be ignored, or by using a function which goes back to previous sections in order to redo their collection. The "Redo" function works by restoring the microscope conditions of the last "good" saved section by retrieving the pertinent information from the data file's extended header; this includes restoring the reference image used for tracking. Microscope and computer failures which can completely halt the data collection do happen occasionally. For such situations, a recovery function was installed to restore the reference section and all environment conditions to the last saved image.

Another action available within the tomography data collection procedure is a back-tracking function. Normally the data collection sequence is set up so that the collection proceeds sequentially towards either the positive or negative tilt direction, starting with the 0 degree tilt. Once the highest tilt in one direction has been reached, data from the other direction, starting again at low tilt needs to be obtained. The back-tracking function quickly tracks an image from high tilts to low in relatively large tilt

increments so that before further collection the image will start out well-aligned with the original 0 degree tilt. This routine drives the sample to a specified tilt, restores the image having the closest tilt and its corresponding microscope settings from the disk file. This is then used as the reference for determining the image alignment parameters. A focusing action is taken to determine the defocus adjustment parameters. These parameters are later added to the next tilt's recovered microscope settings before tracking and focusing parameters are again calculated.

How all these actions are arranged under one data collection scheme is shown by Fig. 2B where a "bank" organization is implemented. Each bank contains all the actions to be used in a collection for a specified tilt range. Depending on the sample, different tilt ranges may require different sets of actions to be carried out. Also within each bank, the monitoring functions for each action can be individually specified. The order of the banks starting from the lowest numbered bank sets the sequence in which the banks are invoked during data collection. Various options such as the ranges for the monitoring functions, target intensities, and preferred defocus are all set in the tomography options panel in the bank menu.

EMCAT (Electron Microscopic Computed Axial Tomography)

Once a data stack is collected, the tilt projection views making up the stack are processed to ensure that their alignment and mass density distribution are consistent with the 3-D object from which they were derived. Only then can the entire set of tilt projection views be used to reconstruct a 3-D model of the specimen. The EMCAT system was developed to consolidate, under one integrated environment, all processing steps necessary for the transformation of the original data stack into its reconstructed form. To maximize the automation of the processing steps, a pipeline was installed so that parameters and files created or modified in one module are automatically updated as input to the next module. Furthermore, each module was optimized so that the number of

input parameters and files entered by the user are kept to a minimum. In the best case, only the name of the data stack, the approximate size and number of the beads used for alignment, and the reconstruction volume are strictly required. Options to switch to an interactive mode are also provided for in each module.

Three subsystems form the main body of EMCAT. STACKEDITOR manipulates data stack organization. EMBALIGN determines projection alignment parameters using fiducial markers. EMRECON calculates the parameters for mass density conversion, applies the parameters and runs the reconstructions.

I. STACKEDITOR

The STACKEDITOR function is designed for easy reorganization of the data file. Generally, data stacks are arranged sequentially by tilt angle and any undesired sections are removed from inclusion in the stack before the reconstruction processing begins. By specifying only tilt ranges, data stack names and individual sections, the STACKEDITOR application will reorder tilt views, combine separate files, and removed unwanted sections to produce a single assembled file ready for the reconstruction process.

II. BALIGN

Gold beads placed on the surface of the specimen act as fiducial markers for calculating the alignment of the projection views. The general scheme of our alignment process is to 1) segment out all features in the entire data stack that possibly represent beads, 2) determine a set of bead locations in a reference tilted view; 3) locate bead-like features in the remaining views that correspond to the set of bead positions in the reference view; and to 4) use the locations of the beads to perform a least squares analysis of the alignment parameters for xy translation, magnification, and in plane rotation of the tilt axis. For those cases where beads are distinctly visualized throughout all tilts and are evenly but not too densely distributed, a complete automation of the alignment using the above scheme has been achieved. On the other hand, for situations where bead conditions are less than optimal, a clear, simple, interactive approach is

needed. The BALIGN subsystem accommodates the requirements of both scenarios by using the IVE to create an direct interplay between the tilt projection images and the graphical parameter representations. There are four modules: BEAD_FINDER, BEAD_MATCHER, BEAD_CHASER, and BEAD_ALIGN, plus a bead position editor PEdit that make up BALIGN subsystem. Some examples of how these modules operate are demonstrated in Fig. 3 where a data set of an isolated Drosophila centrosome is used to illustrate a module's function.

BEAD_FINDER The purpose of this module is to locate the center of mass positions for all beads throughout the entire set of tilt projection views. The procedure for identifying beads involves first an assignment of a local contrast value for each pixel in the tilt projections (Fig. 3B). Next a subset of pixels with high local contrast values are used to create a binary image (Fig. 3C). The threshold for acceptance into the subset is based on an estimate of the percentage of bead to non-bead area in the projection image. A border-walking segmentation algorithm is then employed to group contiguous pixels into objects. Each object is then evaluated for whether it meets area and shape criteria for distinguishing a bead. If an object satisfies all criteria, a potential bead is considered to be found and the center of mass position is calculated and stored.

BEAD_MATCHER Once a large pool of candidate bead positions are identified, a sorting process begins to match individual beads with their positions throughout the data stack. To accomplish this task, BEAD_MATCHER uses a reference bead list, a set of bead positions found on one tilt section, and matches it, in all views, to corresponding positions found by BEAD_FINDER. The reference bead list can be created automatically from BEAD_FINDER's output of candidate bead positions for a single view, or interactively using the PEdit utility to directly select a group of beads from a display of a single projection view. With the knowledge of the previous view's bead positions, a prediction for the pattern of positions in the next view is obtained. Displacement vectors from the predicted positions are calculated from measurements

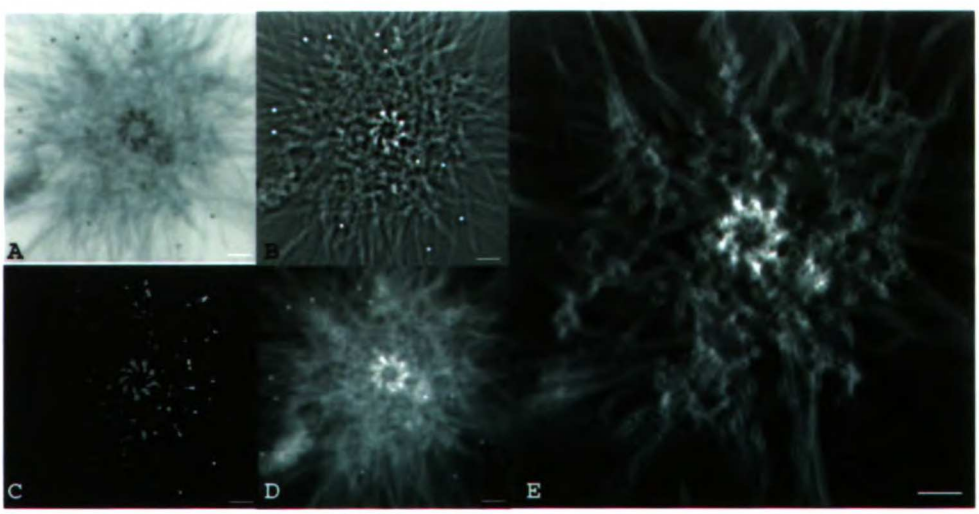

Figure 4.3 Demonstration of some of the steps in reconstructing an isolated centrosome. (A) One tilt view from a data stack collected using the autmoated tomography. The small round structures are the gold beads which are used as fiducial markers. (B) The same tilt view displayed after local contrast processing for bead searching. (C) An image of the view where all features have been classified into objects; diferent objects are identified by their relative intensity. (D) The view after mass normalization and alignment. (E) One slice from the EWBP reconstruction. Scale bar, 50 nm.

between each predicted position and all other predicted positions. These vectors are then compared to vectors obtained from the candidate positions found by the BEAD_FINDER application for that view. If a candidate position matches a predicted position, a minimum residual should result from a squared difference vector comparison. By this method, all potential positions corresponding to actual bead positions can be found. Boundary conditions are also applied to reduce any false matching. The only requirements for this method are that the translational alignments between adjacent projections are small and that a rough estimate of the location of the tilt axis is known. The data collected under the automated system normally satisfies both these requirements.

BEAD_CHASER Usually after BEAD_MATCHER, enough beads positions are found throughout the entire data stack so that the alignment process in BEAD_ALIGN can begin. However, there are cases in which not enough bead positions are found to align every view in the stack; for example when BEAD_FINDER missed some bead positions or BEAD_MATCHER failed to match a position. In these situations, BEAD_CHASER is employed to vigorously search out the bead positions. The method again involves using a previous section's bead position to predict the corresponding bead position in the adjacent view. This time, however, a local search within a given radius of the predicted position is made for the bead, using either a cross-correlation peak method where a ideal bead image is used as a match filter or an adaptive amplitude threshold method of the type employed by BEAD_FINDER but with more lenient size and shape criteria.

BEAD_ALIGN The alignment algorithm in BEAD_ALIGN was originally based on the ALIGN program of Lawrence (1983,1992). A least-squares minimization of the bead positions using a conjugate gradient method is employed to obtain the parameters necessary to align the data stack. The algorithm does not require that each bead has its corresponding bead position located in every projection view; only that there is some

overlap in bead positions in consecutive views and that at least five bead positions per view are available for the fitting. In the automated mode, the bead positions are directly obtained from the output of BEAD_MATCHER. However, if improvement in the fitting is required, refinement of the bead positions through an interactive mode is available as well. The interactive mode uses tools provided by the IVE to couple a graphic representation of the fit for each bead position of every section to actual and theoretical located positions on the image display of the view. The graphical display indicates the residual fitting error for each bead and its coupled image display. If poorly fit positions are selected in the graphics, the image is immediately updated to the view of the position and the position is indicated by a circle. The bead position can then be adjusted by moving the position marker, a cross, to a new place with the mouse. With the new positions, the alignment is refined again until the difference between the theoretical and actual positions is within a satisfactory threshold. The alignment parameters are written out to a parameter file and are not applied until all parameters used in the reconstruction are obtained.

III. EMRECON

The next step is to obtain the parameters to perform a mass normalization of the data i.e. to convert the image intensity to a measure of mass density. Once calculated, these parameters along with the alignment parameters, are applied to the original data stack before the actual reconstruction begins. One reconstruction method or a combination of methods is then chosen as a means to construct our 3-D density map from the collected tilt data. EMRECON is the subsystem responsible for overseeing all these functions and a description of the modules that form EMRECON are detailed below.

MASSNORM Mass normalization is essential for relating the observed image intensities to the object mass densities. A proper treatment for the conversion of mass density requires a clear understanding of the mechanism of image formation in the TEM for the relatively thick specimens used in tomography (Han et al, 1995). Currently, we

have assumed, to a first approximation, an absorption model for image formation, although in the future exit wave front reconstructions will be used as a means to properly treat the phase component for image formation. (Han et al., 1996) Within this module, it is also important to correct for any beam intensity fluctuations that occurred during data collection as well as ensuring positivity of the projections for reconstruction methods where a positivity constraint is used.

APPL_PRM This function applies the parameters obtained from the alignment and mass normalization calculations. Because parameters are stored, rather than applied immediately, a collection of intermediate files are not built up therefore saving disk space and processing time.

RECON The reconstructions are now computed from the mass normalized and aligned data stack. We have two reconstruction algorithms: EWBP (Elliptical Weighted Back-Projection) which is a linear method, and TAPIR (Tomographic Alternating Projection Iterative Reconstruction) which is non-linear and iterative. EWBP computes the weighted back-projection (WBP) reconstruction. Besides the conventional r-weighting function, EWBP contains an elliptical-square weighting function to allow for arbitrary projection tilting geometry and proper reconstruction scale (i.e., the scale of the reconstruction corresponds to that of the projections). The other reconstruction algorithm TAPIR uses an iterative method to compare the reconstruction with the original data while incorporating some boundary conditions. Simply, TAPIR tries to minimize the difference between the reconstruction and the projections with constraints such as positivity and Z-boundedness. Positivity and boundedness provide strong constraints for removing reconstruction artifacts due to the missing wedge (finite tilt range). TAPIR also attempts to minimize the limited detector problem which arises when the specimen area is larger than the detector. Fig. 3E shows an example of one slice of the reconstructed volume of an isolated centrosome reconstructed using the EWBP elliptical-square weighting function.

DISCUSSION

In this paper, we have demonstrated that full automation of the tomographic process has essentially been attained. Convenient methods have been developed to make the automated tomography as straightforward and useful as possible. Much of the development depended on combining the entire process within a single software platform, the Image Visualization Environment. Through automation, tomography can now become a viable approach for the cell biologist to study subcellular structure at high resolution and in three-dimensions. The convenience and speed of the automated system, now a one day event, increases the number of reconstructions that can be done, thus allowing the investigator the freedom to try many experiments which would otherwise be too time-consuming. The increase in number of reconstructions means also that statistically significant number of structures can be obtained adding to the validity of the data interpretation.

Further improvements to increase ease of use and to attain higher quality images for the reconstructions are in progress. One plan is to incorporate individual script files as a selection for the tomography banks in order to provide even more flexibility in the dedicated data collection schemes. An attempt will be made to use exit wave reconstructions to correct images for aberrations that affect image formation. To expand the reconstruction methods, a beadless alignment (W. Liu, unpublished) scheme is in development.

References

Braunfeld, M. B., Koster, A. J., Sedat, J. W., and Agard, D. A. (1994) *J. Microscopy* **174** , 75-84.

Chen, H., Swedlow, J. R., Grote, M., Sedat, J. W., and Agard, D. A. (1995) *in* Pawley, J. B. (Ed.), Handbook of Biological Confocal Microscopy, 2nd. ed., pp. 197-209, Plenum Press, New York.

Dierksen, K., Typke, D., Hegerl, R., Koster, A. J., AND Baumeister, W. (1992) *Ultramicroscopy* **40**, 71-87.

Erasmus, S. J., and Smith, K. C. A. (1982) *J. Microscopy* **127,** 185-199.

Han, K.F., Gubbens, A.J., Sedat, J. W., and Agard, D. A. (1995) *J. Microscopy,* **183,** 124-132.

Horowitz, R. A., Agard, D. A., Sedat, J. W., and Woodcock, C. L. (1994) *J. Cell Biol.* **125,** 1-10.

Koster, A. J., Chen, H., Sedat, J. W., and Agard, D. A. (1992) *Ultramicroscopy* **46,** 207-227.

Koster, A. J., Braunfeld, M. B., Fung, J. C., Abbey, C. K., Han, K. F., Liu W., Chen, H., Sedat, J. W., and Agard, D.A. (1993) *MSA Bulletin* **23**(2), 176-188.

Koster, A. J., van den Bos, A., and van der Mast, K. D. (1987) *Ultramicroscopy* **21,** 209-222.

Koster, A. J., de Ruijter, W. J., van den Bos, A., and van der Mast, (1989) *Ultramicroscopy* **27,** 251-272.

Lawrence, M.C. (1983) *Electron Microsc. Soc. South Afr. Proc.* **13**,19-20.

Lawrence, M.C. (1992) in Frank, J. (Ed.), Electron Tomography, pp. 197-204, Plenum Press, New York.

McEwen, B. F., Arena, J. J., Frank, J., and Rieder, C. L. (1993) *J. Cell Biol.* **120,** 301-312.

Moritz, M., Braunfeld, M. B., Fung, J. C., Sedat, J. W., Alberts, B. M, and Agard, D. A. (1995) *J. Cell Biol.*, in press.

Nomura, S., and Isamozwa, S. (1987) *J. Microscopy* **36**, 157-.

Saxton, W. O., Smith, D. J., O'Keefe, M. A., Wood, G. J., and Stobbs, W. M. (1983) *J. Microscopy* **130,** 187-.

van der Mast, K. D. (1984) *in* Proc. 8th Eur. Congr. on Electron Microscopy, Budapest, Vol1. pp. 3.

Chapter 5 :

Automatic Bead Alignment for Electron Tomographic Reconstruction

Summary

Electron tomography is a powerful tool in the analysis of non-crystalline macromolecular structures. However, its popularity as a more wide-spread technique to analyze cellular structures has been limited, in part, by the difficulty of the reconstruction process. To make electron tomographic reconstruction more accessible, the BALIGN package was developed to automate all the steps for the tilt projection alignment. Based on aligning gold fiducial markers, the algorithms of the BALIGN package, automatically find, sort, and align these fiducial markers to generate an fully aligned tomographic data set.

Introduction

The principle of tomography, which reconstructs a three-dimensional (3-D) structure of an object from its two dimensional (2-D) projections obtained at different view angles has found application in many disciplines (Radon,1917; Herman, 1979; Deans, 1983; Frank 1992). The most well known example is the CAT scan (computerized axial tomography) in which a 3-D image of the body is generated using X-rays, by rotating the X-ray source around the body and acquiring a series of projection images, which are then merged into a 3D image. Likewise, a 3-D image can be generated in the electron microscope by rotating the sample and acquiring a series of projections at different angles. Early development of electron microscopic (EM) tomography has focused mainly on ordered biological structures, such as viruses and 2-D crystals (DeRosier & Klug, 1968; Crowther et al., 1970). Recently, however, there has been increasing interest in EM tomographic studies of variable structures, i.e., structures for which, due to their size and complexity, are not structurally identical, such as the cilia (McEwen et al., 1986), the kinetochore (McEwen et al., 1993) and the 30 nm fiber of chromatin (Woodcock, 1992).

Despite compelling reasons for its usefulness, namely, the need to obtain 3-D structural information and the lack of any other alternative 3-D imaging technique to compete in its resolution range, EM tomography has been applied only sporadically over the last ten

years. Its general lack of popularity can be attributed to the overall tediousness of the entire process starting from the data collection and extending to the reconstruction. Because of the difficulty of doing even a single reconstruction, it has generally not been feasible to reconstruct the large numbers of samples needed in a typical biological experiment. In order to speed up electron tomography, as well as increase its popularity as a routine structural technique, an effort has been made to automate all aspects of the tomographic process. There are two parts to EM tomography, both of which require automation: data collection and image reconstruction. In the past, both have been time-consuming processes requiring constant effort by the user. Initial work on automation focused on the data collection process itself. Automated data collection was made possible by the introduction of the CCD (charge couple device) camera to the transmission electron microscope (TEM) which provided the digital information necessary for computerized automated tomography (Dierksen, 1992; Koster et al., 1993). With the successful automation of tomographic data collection completed (Fung et al., 1996), we now focus on automation of the 3D reconstruction process.

To this end, we have developed an EM tomographic reconstruction software system which we have named EMCAT (Electron Microscopic Computerized Axial Tomography). EMCAT is designed to produce a 3-D reconstruction of an object from its projections, typically a series of single axis tilt images collected from the electron microscope (Fig. 1). Currently, EMCAT is composed of two subsystems: 1) BALIGN which involves the alignment of the projections from fiducial markers and 2) EMRECON which reconstructs the 3-D object from the aligned and mass-normalized projection set. In this paper we will center our discussion on the EMCAT subsystem, BALIGN.

In the EM reconstruction process, the mutual alignment between projections of different view angles is a crucial step. Because the mechanical precision of the electron microscope stage is much worse than the resolution of the microscope, the exact tilt angle for a given projection is not known a priori. In addition, stage drift and other effects also lead to

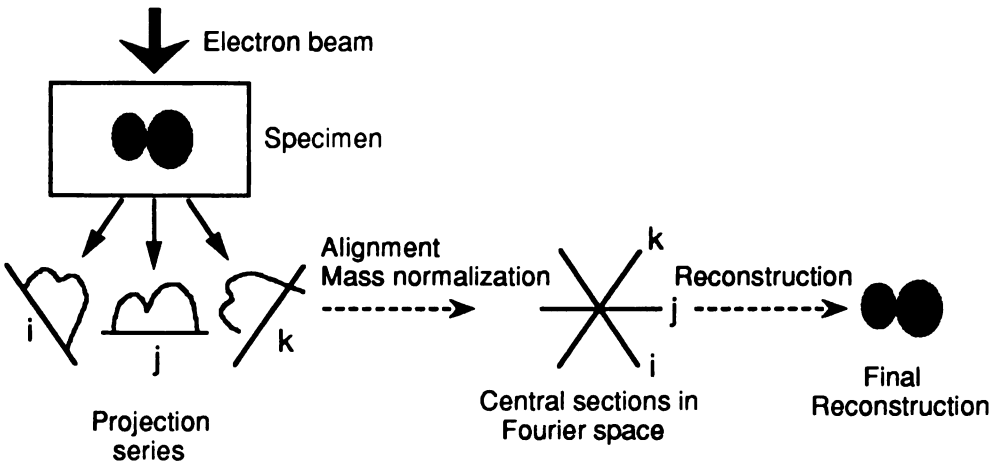

Figure 5.1 Principle of single-axis electron microscopic tomography.
The raw images consist of a series of projections of the specimen collected when the specimen is being tilted around a single tilt axis. The alignment registers projections of different tilts to the imaginary 3-D object. Mass normalization converts the electron counts in the raw data to the mass density of the object. Finally, reconstruction provides the 3-D structure of the object from the aligned and mass normalized projection data set.

displacement of each projection away from its ideal location. Thus, in order to align the different projections to each other, we cannot rely on the mechanical tolerances of the microscope, but rather the alignment must be done after the fact. The standard alignment method is based on gold-bead fiducial markers (Lawrence, 1992). A single-axis tilt projection series is collected after scattering gold particles onto the specimen; the positions of the high density gold beads on the projections are found, and the relationship between the specimen and the digital projection coordinate systems is determined from least-square fitting these bead positions. There are typically four parameters that must be determined for each projection: two translational shifts, one in in-plane rotation, and one in magnification. In order to find these alignment parameters, we must determine the location of a set of gold-bead fiducial markers in every single projection. For 3-D studies of subcellular biological structures, we routinely collect data sets of 110-140 projections in the tilt range of ±75° with our automated EM set-up (Koster et al., 1993, Fung et al., 1996). Normally around 10 bead positions are used on each projection to achieve the alignment. Thus, bead alignment requires over 1000 determinations of bead positions (10 beads per projeciton * 100 projections). Normally, each of these 1000 bead positions needs to be hand-picked for each data set, which is a huge burden on the user and the rate-limiting step in 3D reconstruciton. Thus, if we could automate, as much as possible, the bead detection and aligment step, a dramatic increase would result in ease and speed of use. Here we report the development of an automatic/interactive bead alignment system: BALIGN.

Description of Bead Alignment

There are four different coordinate systems in EM tomography: those pertaining to the microscope, the specimen, the raw images and the aligned images (see Fig. 2). The Y axis of the 3-D specimen coordinate is chosen to be parallel to the goniometer tilt axis, while the x and y axis of the aligned image coordinate can be regarded as the projection of the X and

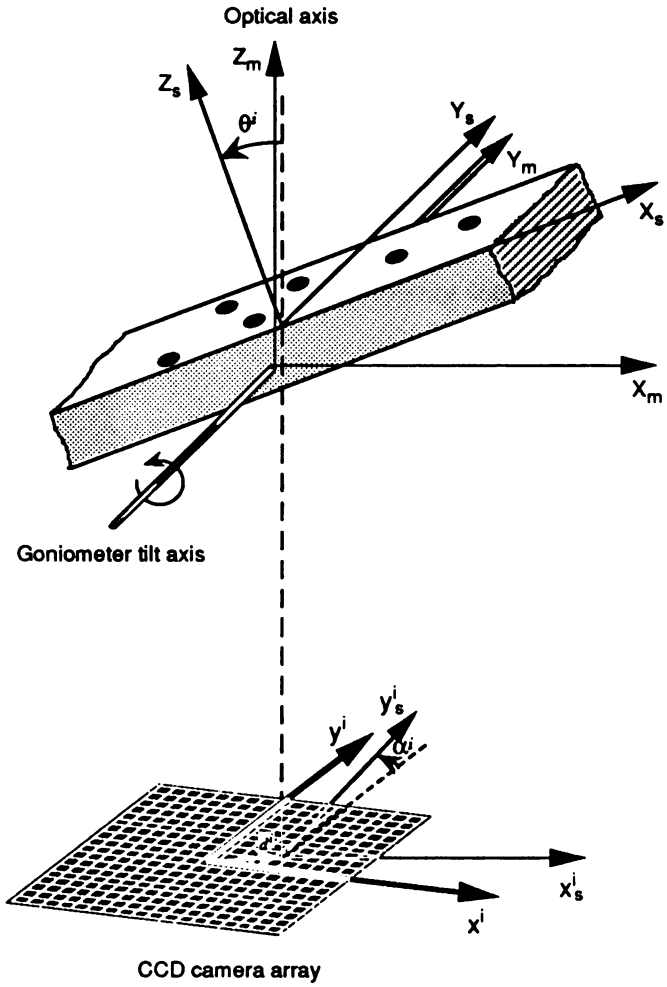

Figure 5.2 Definition of coordinate systems.
The microscope is *Xm - Ym - Zm*. The axis of *Ym* and *Zm* are chosen to be parallel to the goniometer tilt axis and the microscope optical axis respectively. *Xs-Ys-Zs* is for the object, the axis of *Ys* and *Zs* are chosen to be parallel to the goniometer tilt axis and the norm of the specimen section plane respectively. *xi - yi* is for the raw image frame (or CCD frame) of projection *i*, with the axis following the orientation of the CCD camara array. And *xsi - ysi* is for the aligned image frame of projection *i*, with *ysi* axis defined as the projection of *Ys* axis and the frame origin defined as the projection of *Xs-Ys-Zs* frame. The task of alignment is to find out the transformation from *xi - yi* frame to *xsi - ysi* frame for all projections, such that projections in *xsi - ysi* frames will be correctly registered to the specimen in *Xs-Ys-Zs* frame. The in-plane rotation αi can be defined as the angle between the projection line of 3-D goniometer tilt axis and the column lines of CCD array . The shift *di* can be defined as the vector between the projected point of the specimen frame origin and the center of CCD array.

Y axis of the 3-D specimen coordinate. The task of alignment is to obtain the transformation matrix from the raw image coordinate system to the aligned image coordinate system for all projections, so that the transformed projections would be in proper register to the specimen.

For bead j on projection i, its location in the raw image frame r_j^i and the 3-D location of this bead in the specimen frame R_j has the following relationship (Lawrence, 1992):

$$r_j^i = S^i P A^i M^i R_j + d^i \qquad (2.1)$$

where

M^i is a 3*3 diagonal matrix that represents the uniform specimen dimensional changes and/or the variation of the microscope magnification during data collection:

$$M^i = \begin{pmatrix} m_X^i & 0 & 0 \\ 0 & m_Y^i & 0 \\ 0 & 0 & m_Z^i \end{pmatrix} \qquad (2.2)$$

A^i is a 3*3 diagonal matrix describing the specimen tilt operation. For our definition of coordinate systems, the tilt is around Y axis:

$$A^i = \begin{pmatrix} \cos\theta^i & 0 & -\sin\theta^i \\ 0 & 1 & 0 \\ \sin\theta^i & 0 & \cos\theta^i \end{pmatrix}$$

P is a 2*3 matrix describing the projection action down Z axis,

$$P = \begin{pmatrix} 1 & 0 & 0 \\ 0 & 1 & 0 \end{pmatrix}$$

S^i is a 2*2 rotation matrices describing the rotation of raw image frame relative to the aligned image frame,

$$S^i = \begin{pmatrix} \cos\alpha^i & -\sin\alpha^i \\ \sin\alpha^i & \cos\alpha^i \end{pmatrix}$$

The parameters that describe the registration of a raw image to the 3-D object are given below:

Tilting angle θ^i.

Magnification m^i.

In-plane rotation α^i.

Shifts $d^i = \begin{pmatrix} x^i \\ y^i \end{pmatrix}$.

Specimen shrinkage t^i.

If the shrinkage in X and Y directions are regarded the same, Eq. (2.2) will become

$$M^i = m^i \begin{pmatrix} 1 & 0 & 0 \\ 0 & 1 & 0 \\ 0 & 0 & t^i \end{pmatrix}$$

where t^i is the Z shrinkage relative to that of X and Y, and m^i is, in fact, the combined contribution of X, Y and Z shrinkage and the magnification change.

With enough bead positions provided, Eq. (2.1) can be solved to give projection alignment parameters and the 3-D bead locations. The least-square (LS) solution can be obtained via minimizing the residual of f as a function of alignment parameters and 3-D bead locations, with

$$f = \sum_{i,j} \left\| r_j^i - (S^i P A^i M^i R_j + d^i) \right\|^2 \qquad (2.3)$$

The summation in Eq. (2.3) is defined to be over all available bead positions.

The number of equations in (2.1) is twice the total number of available bead positions, which should be no less than the number of degrees of freedom (NDF) in Eq. (2.3) for determining the alignment parameters. In practice, around 10 bead positions on each image is recommended to ensure accuracy.

The Algorithms

We have described how the alignment parameters are calculated from the provided bead positions. But it is obtaining the bead positions that consumes most of the time needed for bead alignment. Thus most of our effort to automate bead alignment is to automate the searching of bead positions. To obtain bead positions for alignment, individual bead positions on each projection should first be found. Then the positions need to be correctly indexed to determine their correspondence to the beads on the specimen. Our automatic bead alignment system contains four basic data processing modules: 1) BEAD_FINDER tries to identify any bead-like features on each projection; 2) BEAD_MATCHER indexes the bead positions by tracing individual beads through all projections; 3) BEAD_CHASER chases bead positions missed by the previous modules; and 4) BEAD_ALIGN provides the alignment parameters through LS fitting the bead positions.

The projections in the raw data set are sorted according to their tilt angles. So in the ensuing discussions, neighboring projections refers to the proximity of their tilt angles.

Module 1. BEAD_FINDER

In this module, bead-like features for each projection of the data set are found, using size, shape and prominence as criteria.

Step 1.1: Computation of mass density image

During data collection, due to the changes of effective specimen thickness as the function of specimen tilt angle, the range of intensity and contrast between projections in a raw data set can be very different. For the subsequent segmentation analysis, it is desirable to convert the values of electron counts in the raw data into quantities that are tilt independent. The suitable candidate is the specimen mass density. Since the low-resolution image formation in the TEM follows the absorption model, the mass density of the structural component is given as

$$\rho^i(\vec{r}) = -\{\log[e^i(\vec{r})] - \log[b^i(\vec{r})]\}$$
$$= -\log[1 + \frac{e^i(\vec{r}) - b^i(\vec{r})}{b^i(\vec{r})}]$$
$$\approx \frac{e^i(\vec{r})}{b^i(\vec{r})} - 1 \qquad (3.1)$$

where local background $b^i(\vec{r})$ takes the mean value of a box region around $\vec{r}$ in the raw image $e^i(\vec{r})$.

Step 1.2: Getting the binary image

For further segmentation to identify individual features, the pixels of the mass density image are evaluated and the corresponding binary image is generated. The binary label is 1 for foreground, and 0 for background. The binary pixel value is 1 if the value of the corresponding pixel and at least two of its neighbor pixels are above the density threshold T^i.

The density threshold value T^i varies with projections, and should be determined from parameters that are projection-invariant. In our implementation, the radius of the "ideal" bead r_0 and the maximum number of expected beads $N_{b\max}$ found in a projection are used as inputs. They determine the percentage of pixels in the image that should be in the binary foreground:

$$\eta = w_h * S_0 * N_{b\max} / A \qquad (3.2)$$

where $S_0 = \pi r_0^2$ is the area of the "ideal" bead, A is the area of the image, and w_h is the foreground factor. w_h takes into account that not all features in the binary image represent beads, hence percentage threshold value higher than the total bead area allows should be selected via choosing $w_h > 1$.

The density threshold T^i can now be given from the histogram of the mass density image, as the value that corresponds to the upper percentage of η in the histogram.

Step 1.3: Segmentation of binary image

All the isolated features in the binary image are found via image segmentation. The

value of a pixel in the segmented image represents the feature to which this pixel belongs to.

Step 1.4: Selection of bead-like features

First, a list of features in the segmented image are identified to be within the area and shape criteria: a) its size S_b is within the multiple range of (γ_l, γ_u) of the "ideal" bead size, and b) its shape factor f_{sh} is above the shape factor threshold f_0. The shape factor is defined by

$$f_{sh} = 4\pi S_b / C_b^2$$

where C_b is the circumference of the feature. Note that the shape factor of a circle is 1.

The qualified features are ranked twice, based on the distances of their sizes and shape factors from the values of the ideal feature, correspondingly. Each feature is scored by linearly combining its two rankings. Then features with top scores are selected as candidates for subsequent bead matching.

Module 2. BEAD_MATCHER

This module identifies all available positions in the bead-like feature list that corresponds to any given bead.

Step 2.1: Hand-picking of seeding beads on reference section(s)

There are three possible scenarios that arise from the bead-like feature list produced by BEAD_FINDER: true, false and missing. A bead-like feature can correspond to a true bead or a false one (i.e., non-bead feature). A desired bead position can be found or missed for some projections. The corresponding potential complications in bead matching is much avoided by hand-picking desired beads as seeds on one or several reference projections.

Step 2.2: Calculation of rough alignment parameters

For our EM setup, the in-plane rotation parameters can be predicted to an accuracy of within 1-2 degrees, while the magnification change is within one percent due to the specimen shrinkage and the objective current change. Normally, for bead matching purpose, the cross-correlation alignment between adjacent projections during the data collection gives good enough rough translational alignment, so that the centers of adjacent projections are regarded as aligned in calculating the rough shift parameters.

Step 2.3: Matching of bead-like feature pattern with predicted pattern

Using chosen reference beads on the first reference section and starting from this reference section, the bead positions are matched through consecutive sections. For any given section, the bead positions on the current section are predicted from the positions of matched bead positions on previous sections and the knowledge of rough alignment parameters. Then, the predicted bead pattern (t pattern) is used as the template to match with the pattern of the bead-like features (p pattern) (see Fig. 3).

We now go through these two steps in more detail. Let's represent the bead-like feature list as p_k^i, the matched bead list from the first reference section as m_{1j}^i, and the predicted pattern on section i as t_j^i. The task of matching can now be rephrased as to find out an corresponding p_k^i with the correct index k for each bead j on projection i. The predicted positions are calculated as follows:

Estimate the shift alignment parameters of section i -1 using common beads between i -1 and previously matched sections.

Estimate missing bead positions in the matched list on section i -1.

Let $m_{1j}^{'i-1}$ represent the matched list on projection i -1 with the predicted bead positions incorporated. Suppose the position of bead j is missing on i -1 and the closest section on which bead j exists is i_2, e.g., $m_{1j}^{i_2}$ exists. Then $m_{1j}^{'i-1}$ can be predicted from $m_{1j}^{i_2}$ by using rough alignment parameters. If bead i does not exist

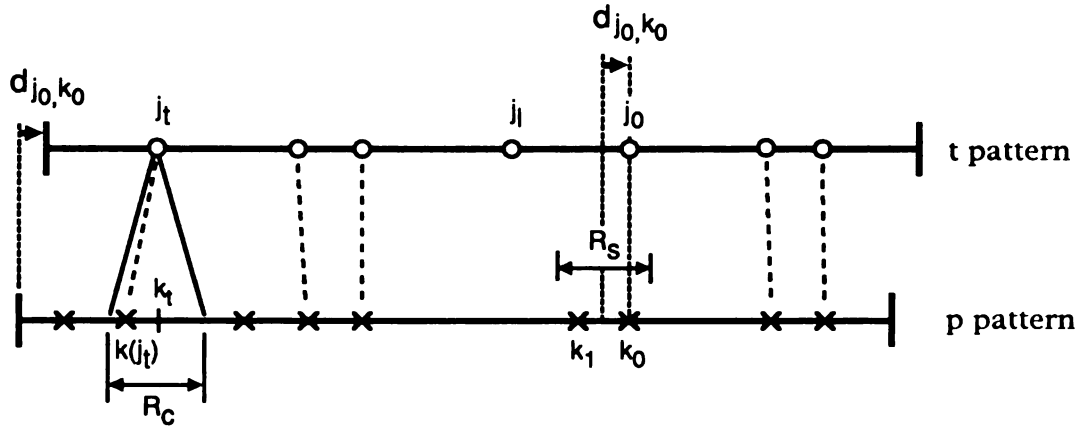

Figure 5.3 Pattern matching in BEAD_MATCHER (1-D representation)
The p pattern represented by crosses is from the bead-like features on the current matching projection, while the t pattern is represented by circles is predicted from the matched bead positions on the previous projection. In this representative example, bead j_0 searches in the p pattern within the radius of R_s. Two features (k_0 and k) are found for its matching trials. Here the matching trial between bead j_0 in the t pattern and feature k_0 in the p pattern (which is the correct match) is illustrated. The t pattern is shifted by $d_{j0,k0i}$ such that j_0 and k_0 overlap. Each bead in the t pattern searches for the closest feature in the p pattern within the radius of R_c : All beads find partners except j_l whose true matching feature is missing. But the partner of j_t is a wrong match, which results from the situation that the true match is missing and there is the feature $k_{(jt)}$ within the radius of R_c.

in the matched list within a defined projection range, further matching for this bead on the remaining sections will be stopped.

Estimate bead positions on section i from $m_{1j}^{'i-1}$, by using rough alignment parameters

The relative shifts between section i and i-1 are estimated using hand-picked single features (if available) or center of image frame as common features .

There are two types of inaccuracy regarding to how close the estimated bead positions in t_j^i are to the positions of corresponding beads in the bead-like feature list p_k^i: type I) the relative shift between the two patterns, with the accuracy determined by the that of shift parameter predictions in step c; type II) the degree of matching of corresponding bead positions in the two patterns, with the accuracy determined by the fitness of the co-planar assumption of beads in the specimen, relative to the angular distances between the involved neighbor projection pairs when predicting missing bead positions. These uncertainties are overcome by evaluating many match trials and choose the match with the smallest residual:

Let's assume that the upper limit of shift prediction accuracy in step c is R_s. We now shift the c pattern by a distance of $d_{j_0,k_0}^i = p_{k_0}^i - t_{j_0}^i$ which is within the range of R_s, so that the position of a given starter bead j_0 in the c list overlaps that of an given feature k_0 in the p pattern. Then, each other bead j in the shifted c pattern attempts to find the nearest point $k(j)$ as its partner in the p pattern within the defined range of R_c. Note that j does not have to find a $k(j)$ because the corresponding position might be missing in p_k^i (this is represented by I_j which is 1 if found, and 0 otherwise).The residue of this matching trial is

$$S_{j_0,k_0}^i = \frac{\sum_j I_j \left\| t_j^i - p_{k(j)}^i - d_{j_0,k_0}^i \right\|}{\sum_j I_j}$$

By going through all allowed combinations of j_0 and k_0, the matching trial that gives the smallest residue is accepted as the correct match, and the corresponding positions in the p list are assigned to the matched list for section i.

There are normally several trials in which j_0 and k_0 are true partners (up to the number of beads in the t pattern). But the residues of these trials are different due to the different type II error in their starter beads j_0. Such error introduces mis-registration between the rest of the beads in the t pattern and the p pattern, which can cause mismatching in the pairing-up of bead j and feature $k(j)$. The selected matching trial that has the smallest residue normally has the smallest type II error in its starter bead; this in turn introduces the smallest chance of mismatching.

Since mismatching of partners can happen even in the selected trial that gives the best overall match (an instance is illustrated in Fig 3. with the mismatch between j_t and $k(j_t)$). To minimize the chance of such mismatches, a final check of the selected positions in the p list is carried out before assigning to the matched list: a position: $k(j)$ is excluded if its distance from its matching partner j has $\left|c_j^i - p_{k(j)}^i - d_{j_0,k_0}^i\right| < d_f$ (with d_f being the pre-defined matching distance threshold).

It is evident at this point that as a rule of thumb, for our matching approach, the above two types of inaccuracies should be smaller than the average distance between neighboring features in the p list, a condition which is normally attainable.

Step 2.4: Merge of matched lists from different reference sections

As the matching process continues from one projection to the next, gradually bead matches will be lost, so that after matching beads across many different projections, the number of matched beads will become small. Typically the first reference section has a tilt angle close to 0°, and the number of beads that can be matched with this untilted projection will decline as the tilt angle increases. To overcome this problem we use more than one reference section across the tilting range of the data set. The matching from each reference section is independently executed as described by Steps 2.3. The resultant matched bead lists are merged to provide the final matched bead list .

The merging of a matched list m_k to the merged list M_{k-1} (which is the result of

merging previous k-1 matched lists) proceeds as follows: For a given bead of index j_m in the matched list, where at least one of its positions overlap with the position of certain bead of index j_M in the merged list, j_m can be regarded to correspond to the same bead as j_M. Subsequently the positions of this bead which are available in m_k but not in M_{k-1}, will be copied into M_{k-1}. Otherwise, if there is no such overlap with any bead position in M_{k-1}, the bead with index j_m will be regarded as a new bead and all its positions will be added to M_{k-1}.

Module 3. BEAD_CHASER

In the matched list from BEAD_MATCHER, there are typically gaps of missing bead positions (see Fig. 4). Since the missing bead positions can be accurately predicted from the available common bead positions in the matched list, and only the local areas around the predicted locations need to be searched, more sophisticated approaches can be employed to chase the missing bead positions.

Step 3.1: Estimation of rough alignment parameters

The in-plane rotations and magnifications are estimated as described in step 2.2. For any projection i, the shift parameters are calculated by finding common bead positions in the matched bead list between projection i and its closest possible neighbor within the defined searching range of N_s. Once the rough alignment parameters are available for the whole data stack, starting from a section with tilt angle close to 0°, missing bead positions can be chased through consecutive projections:

Step 3.2: Prediction of missing bead positions

Given the information of the rough alignment parameters, a missing bead position on the current section is predicted from the position of the corresponding bead existing in the

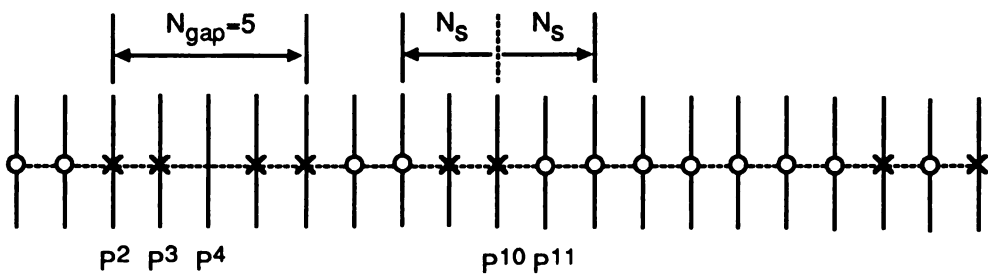

Figure 5.4 Prediction for the missing positions of a bead in BEAD_CHASER

Vertical lines represents the projections (as represented by P^i). Circles represent the old positions, e.g., positions identified by BEAD_MATCHER. Crosses represent the new positions, e.g., positions that are predicted from the old positions and the initial alignment parameters. The searching range is N_S =2 in this illustration. The prediction on P^{10} is from the available old position on its neighbor P^{11}. The position on P^4 can not be predicted from the old positions because they are not available in its neighborhood of the searching range N_S , though this position can be predicted from the new position on P^3 or P^5.

matched list which is on the closest neighbor within the defined searching range of N_s.

Step 3.3: Local search and selection of best feature

We then search for a missing bead position within the given radius of R_c around its predicted position using a cross-correlation peak searching method: the cross-correlation map is calculated from the local region of the raw image and a bead image. The cross-correlation peaks in this region are evaluated with peak heights, and sizes and shapes of the half-height area as criteria. The peak with best score is selected with the ranking and scoring methods as described in BEAD_FINDER.

Module 4. BEAD_ALIGN

Once a sufficient number of matched bead positions becomes available, we can proceed to obtain the alignment parameters by least-square fitting the bead positions.

Step 4.1: Estimation of initial alignment parameters

Reasonable initial estimates of alignment parameters are required before the minimization. The initial rotations and magnifications are estimated as in Step 2.2.

Step 4.2: Least-squares fitting

The conjugate gradients method is used in the LS minimization.

Step 4.3: Interactive editing of bead positions

The fitting results for individual bead positions are graphically displayed. The distances between the fitted and found bead position pairs are shown in the interactive diagnostics window. These fitted and found position pairs are also overlaid on to the corresponding projection images in the image window, from which those badly fitted bead positions can be inspected and graphically edited (correct/add/delete) (see Fig. 5 for detail).

A

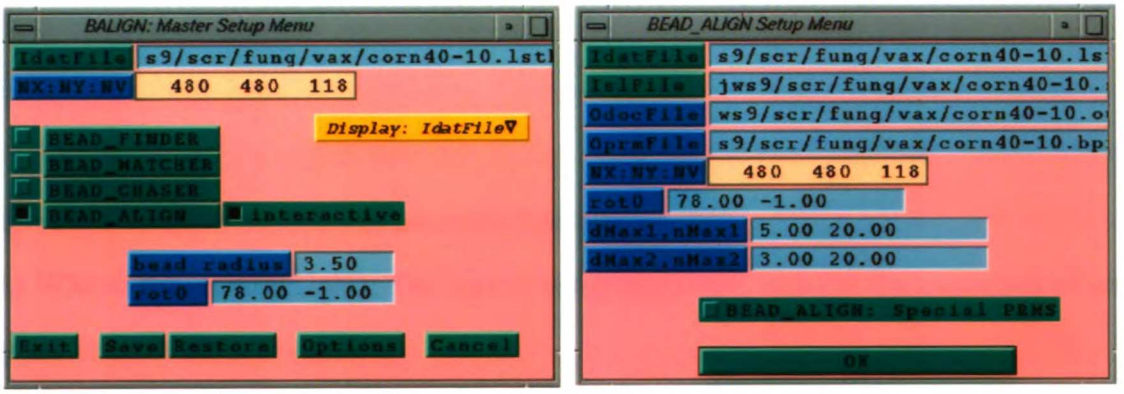
BALIGN: Master Setup Menu
IdatFile
s9/scr/fung/vax/corn40-10.lst
NX:NY:NV
480 480 118
Display: IdatFile
BEAD_FINDER
BEAD_MATCHER
BEAD_CHASER
BEAD_ALIGN
interactive
bead radius
3.50
rot0
78.00 -1.00
Exit
Save
Restore
Options
Cancel
BEAD_ALIGN Setup Menu
IdatFile
s9/scr/fung/vax/corn40-10.ls
IelFile
jws9/scr/fung/vax/corn40-10.
OdocFile
ws9/scr/fung/vax/corn40-10.o
OprmFile
s9/scr/fung/vax/corn40-10.bp
NX:NY:NV
480 480 118
rot0
78.00 -1.00
dMax1,nMax1
5.00 20.00
dMax2,nMax2
3.00 20.00
BEAD_ALIGN: Special PRMS
OK

B

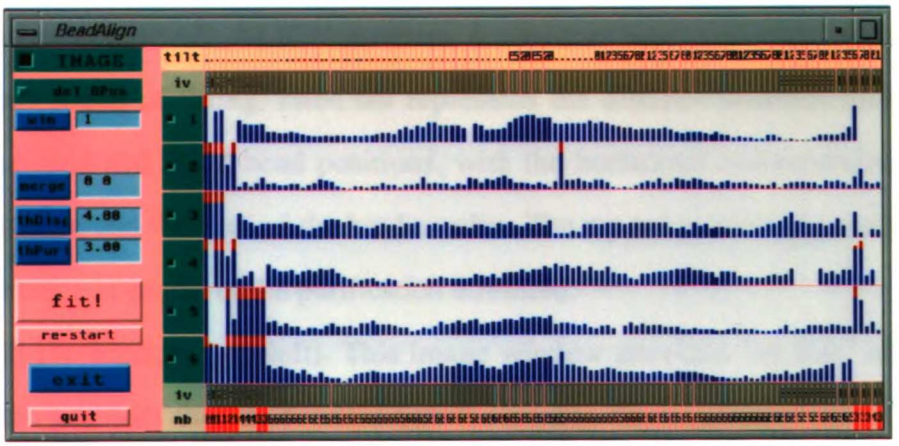
BeadAlign
IMAGE
tilt
iv
win
1
merge
0 0
4.00
3.00
fit!
re-start
exit
quit
iv
nb

C

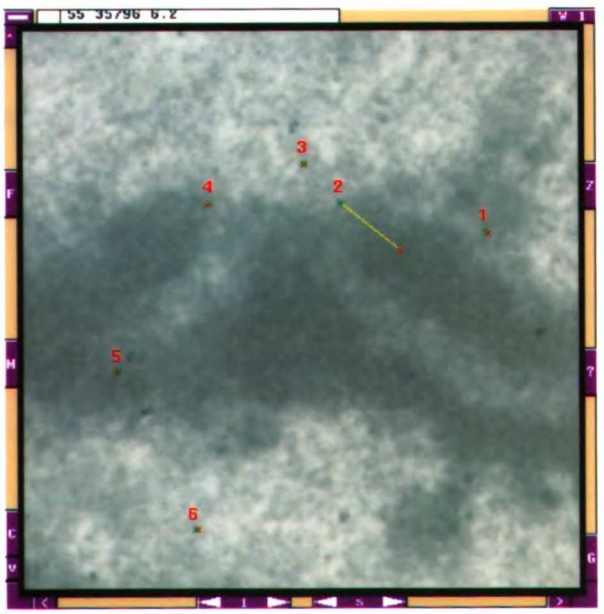
1
2
3
4
5
6

Figure 5.5 Graphic windows of interactive BEAD_ALIGN:

(A) WM-windows (top-right): The master setup menu can activate the execution of any combination of the four modules.

(B) ID-window (lower). This interactive diagnostics window is created in running the interactive BEAD_ALIGN program. It monitors how well each bead position is fitted in each round of fitting. Each bar represents the distance between corresponding pairs of matched and fitted bead positions, with the horizontal corresponding to the projection number, and the vertical the bead number. The top red portion of a bar represent the part of distance in excess of the purification threshold.

(C) IW-window (top-left). This image window provides "on line" editing of individual bead positions that are overlaid onto the images. Corresponding pair of matched and fitted bead positions are connected by a line.

The practical data set of synaptonemal complex with 112 projections and 10 beads is used here for illustration (see Section 5).

Step 4.4: Exclusion of badly fitted bead positions and re-fitting

The initial fitting result is always non-optimal, since there are always relatively badly fitted bead positions that can be somehow treated for improvement. Instead of the interactive editing to make corrections, these positions can simply be excluded in the next round of fitting, provided that there are enough bead positions left for fitting. The exclusion threshold in automatic mode is pre-defined, while in interactive mode it is provided "on line" by inspecting the fitting result of previous round of fitting.

Step 4.3 and 4.4 are repeated until a good fitting which indicates a good alignment is achieved.

4. Application Example

We now illustrate the bead alignment process on a typical biological data set. The structure under study is the synaptonemal complex (SC), an organelle that plays a role in the synapsis of paired chromosome during meiosis. 0.3 um semi-thick sections containing the SC within its chromosome environment are cut and stained from a fixed and embedded maize meiocyte. 15 nm gold beads are applied to the top surface of the section. A tomographic data set of 112 projections (Fig. 6) is collected in the tilt range of -68° to +75° using a 300 keV Phillips 430 intermediate EM. The images 480*480 pixels in size are recorded directly by a cooled slow scan CCD camera with a two-fold binning under the magnification of 7,500 (this results in a sampling rate of 39 Å/pixel).

An inspection of images from the raw data gives an average bead radius of around 2.5 pixels. The in-plane rotation at magnification of 7,500 is known to be approximately 75°. These two numbers are used as inputs for the ideal bead radius and the initial estimates of the in-plane rotations.

In BEAD_FINDER, we first choose the parameters by testing 5 projections across the tilt range. In our case, the optimal parameters are attained where the maximum expected number of beads $N_{b\max} = 50$ (default), the foreground factor $w_h = 3$ (default), and the

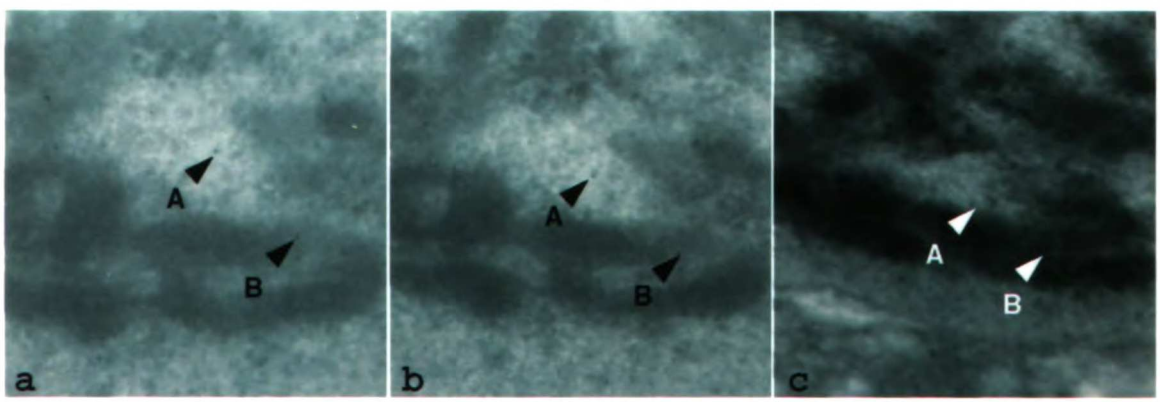

Figure 5.6 Representation of projections of different tilts in the raw data set. (a) 0^{o} (b) -40^{o} (c) -70^{o}. Arrow heads point to beads A and B as seen in the different tilts.

saturation factor f_s = 0.8 (default = 1). With approximately 10 beads in each projection, the choice of $N_{b\max}$ =50 allows the appropriate amount of bead-like features to be selected for subsequent bead matching: wrong matching might result from the congregation of too many candidates of bead-like features, while the true bead-positions might be missed from the selection of too few bead-like features. The threshold for creating the binary image is determined from the desired total bead area which is a function of $N_{b\max}$ and f_s as show in Eq. (3.5). The choice of such threshold affects the amount, shapes and sizes of features in the binary image. In this data set, most bead positions overlap with the specimen of interest, a saturation factor of 0.8 (instead of the default 1) would enhance the features in the structure, hence promoting the chance of finding those bead positions on the structure. Fig. 5 illustrates the procedure of BEAD_FINDER with an exemplary projection.

For BEAD_MATCHER, 12 seed bead positions are hand-picked on a reference projection of close to 0° tilt (section #60).

After the sequential tracing of the corresponding positions for the reference beads, only the projections with the highest tilts cannot be matched (section #0-6 with tilt 63.8-57.5°, and section #101-111 with tilt 62.5-75°). The reason is BEAD_FINDER missed too many true bead positions at these ranges, due to 1) low contrast between the bead feature and the overlaying structure as a result of increasing length of electron path through the specimen towards higher tilts, and 2) the blurring image of high tilts (see Fig. 6). So for the projections of high tilt, we use PEdit to interactively add bead positions to the bead-like feature list. A subsequent run of BEAD_MATCHER matches throughout all projections, resulting in 10 matched beads (Out of 12 seeds, 2 beads are excluded because fewer than two total positions are matched for them).

BEAD_CHASER goes through projections and pursues the missing bead positions using default input parameters: the searching projection range for predicting a missing bead position N_s=10. The searching radius around a predicted bead position $R_c = 3r_0 = 7.5$ pixels.

With the matched bead list in hand, we now go through interactive BEAD_ALIGN to obtain the alignment parameters by least-squares fitting the bead positions.

1. After the initial round of fitting the interactive diagnostics window is popped up. The standard deviation = 4.5 pixels, indicates a poor fit (see Fig. 7), which is the consequence of 2-3 incorrectly found bead positions on some projections of high tilts.
2. The badly fitted bead positions are interactively edited (corrected or removed) in the image window, with the found and fitted bead positions overlaying onto the corresponding projections. The subsequent re-fitting (without purification) gives a standard deviation = 1.2 pixels.
3. Now, we exclude the less-well fitted bead positions for the next round of fitting, with a threshold thPuri=2. pixels. The resultant standard deviation = 0.70 pixel.
4. Another round of fitting with the purification threshold thPuri = 1.5 pixel gives a final standard deviation = 0.63 pixel (see Fig. 8).

6 Conclusion

We have described BALIGN, which is a sub-system of our electron tomographic image processing software EMCAT. BALIGN has attempted to maximize the degree of automation and at the same time maintains the flexibility to solve any potential problems a user might encounter. Automating this particularly tedious process in the reconstruction procedure reduces the complexity of general tomographic methods and can aid in allowing larger numbers of reconstructions to be processed.

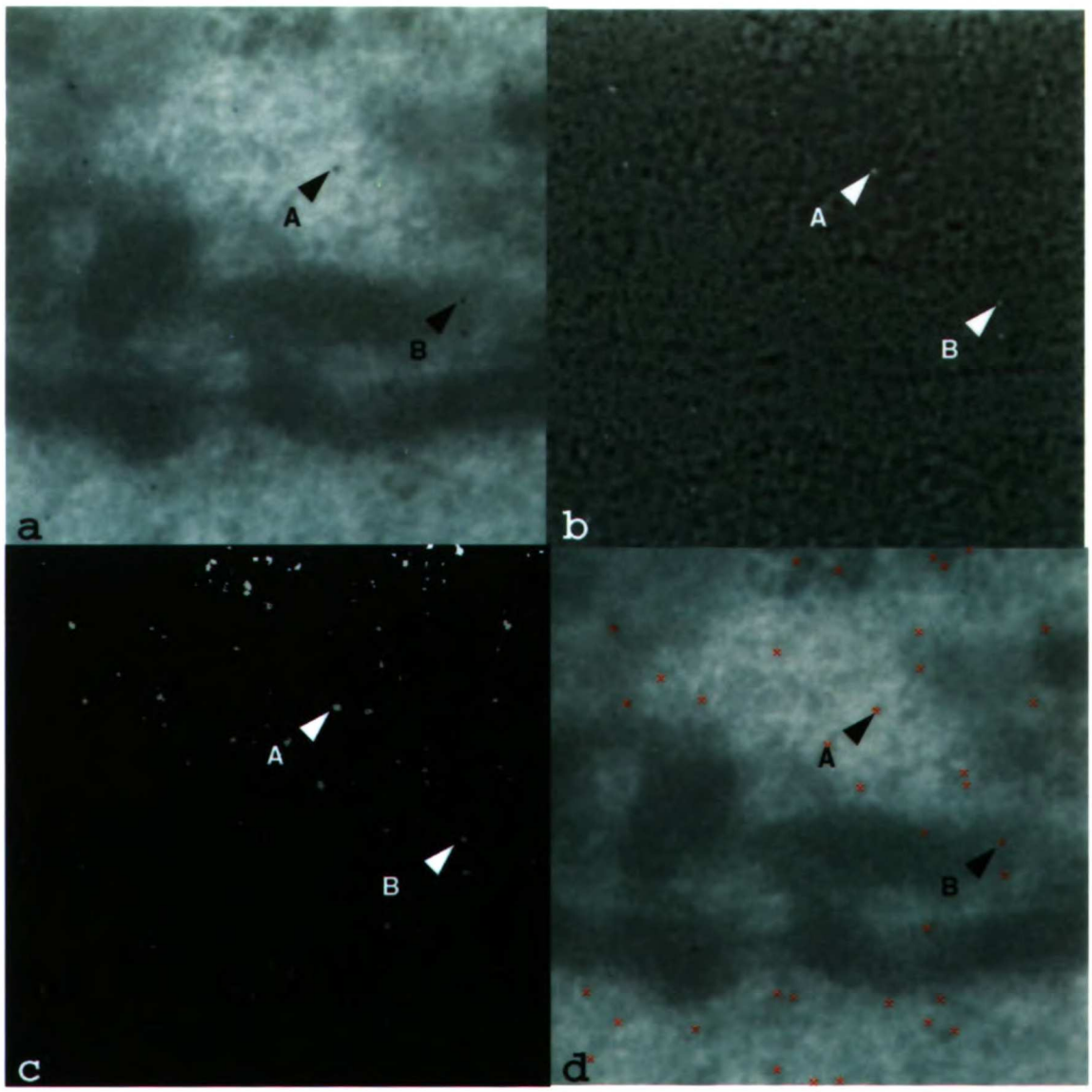

Figure 5.7 BEAD_FINDER finding bead-like features on a typical projection. (a) one zero degree tilt projection (b) mass density image (c) segmented image, with the value of each pixel representing the feature to which it belongs. (d) Selected bead-like features overlayed on the 0 degree tilt projection.

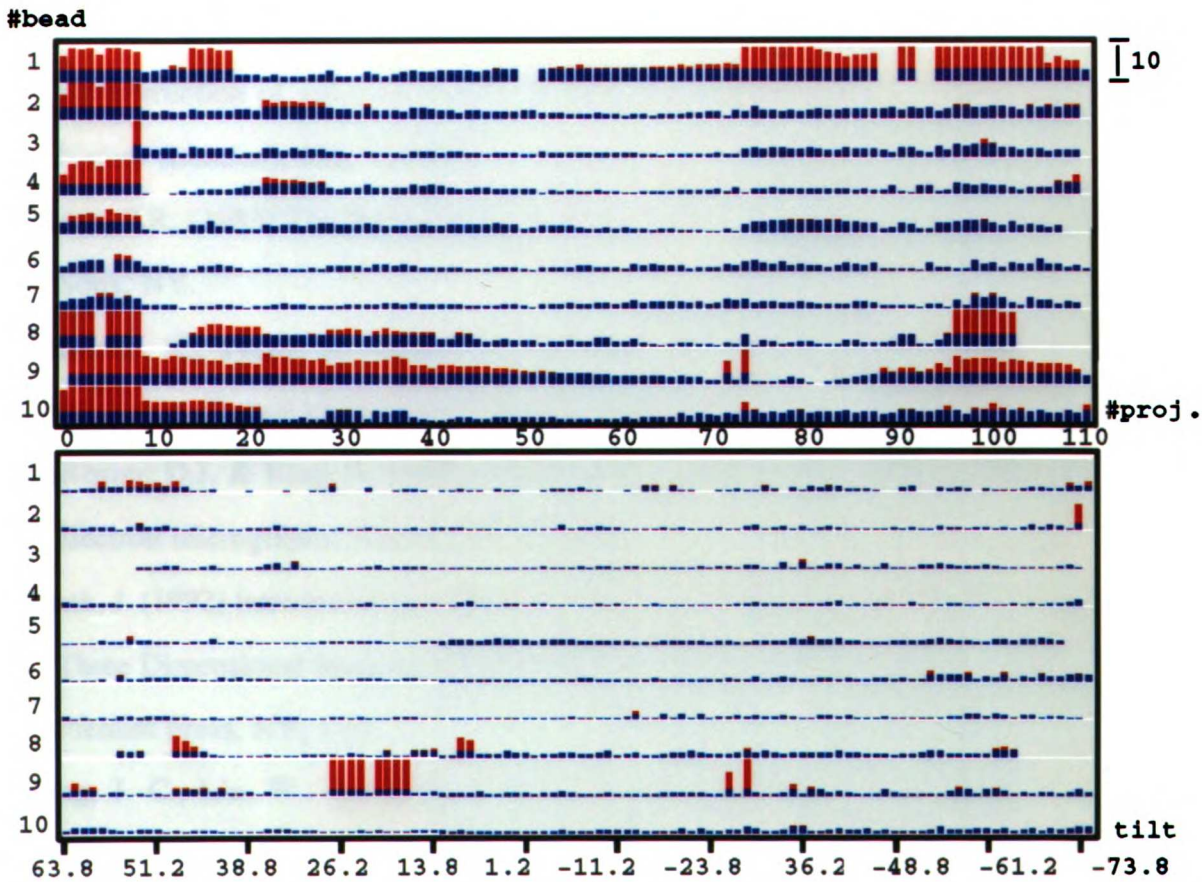

Figure 5.8 Interactive BEAD_ALIGN:LS fitting diagnostics.
(Top) Fitting diagnostics after the initial round of fitting (thDisp=10 pixels, thPuri = 3.0 pixels, and fitting standard deviation = 4.2 pixels. (Bottom) Final fitting diagnostics (thDisp =10 pixels, thPuri-1.5 pixels, and fitting standard deviation = 0.61 pixels). The length of the bar represents the distance betweeen the fitted position and the corresponding bead position. The top red portion of bar represents the part of distance in excess of the purification threshold. Note that in the initial round, the fits for projections #0-8 (with tilts 63.8-53.8o) are especially bad as the consequence of 2-3 wrongly found bead positions (bead 8,9, and 10). In the final round of fitting, the poorly fitted bead positions that correspond to the bars greatly in excess of the purification threshold are excluded from the fitting.

References

Crowther, R.A., Amos, L.A., Finch, J.T. & Klug, A. (1970) Three-dimensional reconstruction of spherical viruses by Fourier synthesis from electron micrographs. Nature (London), **226**, 421-425.

Deans, S.R. (1983) The Radon Transform and Some of Its Applications. John Wiley & Sons, NY.

Dierksen, K., Typke, D., Hegerl, R., Koster, A.J. & Baumeister, W. (1992) Towards automatic electron tomography. Ultramicroscopy, **40**, 71-87.

DeRosier, D.J. & Klug, A. (1968) Reconstruction of three-dimensional structures from electron micrographs. Nature, **217**, 130-134.

Frank, J. (1992) Introduction:principles of electron tomography. In: Electron Tomography: Three Dimensional Imaging with the Transmission Electron Microscope (Ed. J. Frank). Plenum Press, NY, 1-13.

Fung, J. C., Liu, W., de, Ruijter. W. J., Chen, H., Abbey, C. K., Sedat, J. W. and Agard, D. A. (1996). Toward fully automated high-resolution electron tomography. Journal of Structural Biology **116**, 181-9.

Herman, G. T., ed. (1979) Image Reconstruction from Projections. Springer-Verlag, Berlin.

Koster, A.J., Braunfeld, M.B., Fung, J.C., Abbey, C.K., Han, K.F., Liu, W, Chen, H., Sedat, J.W. & Agard, D.A. (1993) Towards automatic three dimensional imaging of large biological structures using intermediate voltage electron microscopy. Mic. Soc. of America Bulletin, **23**, 176-188.

Lawrence M.C. (1992) Least-squares method of alignment using markers. in: Electron Tomography: Three Dimensional Imaging with the Transmission Electron Microscope (Ed. J. Frank). Plenum Press, NY, 197-204.

McEwen, B.F., Radermacher, M., Rieder, C.L., & Frank, J. (1986) Tomographic three-

dimensional reconstruction of cilia ultrastructure from thick sections. Proc. Natl. Acad. Sci. USA, **83**, 9040-9044.

McEwen, B.F., Arena, J.T., Frank, J. & Rieder, C.L.(1993) Structure of the colcemid-treated PtK1 kinetochore outer plate as determined by high voltage electron microscopic tomography. J. Cell Biol., **120**(2), 301-312.

Radon, J (1917) On the determination of functions from their integrals along certain manifolds (in German). Ber. Verh. K. Sachs. Ges. Wiss. Leipzig, Math.-Phys. KL. **69**, 262-277. (For an English translation, see Deans, 1983).

Woodcock, C.L. (1992) The organization of chromosomes and chromatin. In: Electron Tomography: Three Dimensional Imaging with the Transmission Electron Microscope (Ed. J. Frank). Plenum Press, NY, 313-357.

Appendix 1:

Phase Behavior of Ordered Diblock Copolymer Blends: Effects of Compositional Heterogeneity

Phase Behavior of Ordered Diblock Copolymer Blends: Effect of Compositional Heterogeneity

Richard J. Spontak,*,† Jennifer C. Fung,‡ Michael B. Braunfeld,§ John W. Sedat,§ David A. Agard,§ Lisaleigh Kane,‡ Steven D. Smith,*,⊥ Michael M. Satkowski,‖ Arman Ashraf,⊥ Damian A. Hajduk,*,▼ and Sol M. Gruner‡

Department of Materials Science and Engineering, North Carolina State University, Raleigh, North Carolina 27695, Graduate Group in Biophysics, University of California, San Francisco, California 94143, Department of Biochemistry and Biophysics and the Howard Hughes Medical Institute, University of California, San Francisco, California 94143, Corporate Research Division, The Procter & Gamble Company, Cincinnati, Ohio 45239, and Department of Physics, Princeton University, Princeton, New Jersey 08544

Received October 24, 1995; Revised Manuscript Received January 17, 1996[⊗]

ABSTRACT: Diblock copolymers order into a variety of periodic morphologies when the constituent blocks are sufficiently incompatible. Previous studies have demonstrated that classical dispersion (spherical and cylindrical) and lamellar morphologies, as well as complex morphologies (*e.g.*, gyroid*, lamellar catenoid, and hexagonally perforated lamellae), can be selectively accessed through either tailored molecular synthesis or copolymer/homopolymer blends. In the present work, control over ultimate morphology is achieved through the use of binary copolymer blends composed of two strongly-segregated poly(styrene-*b*-isoprene) (SI) diblock copolymers of equal molecular weights but different compositions (one 50 wt % S and the other 85 wt % S). Blend morphologies are examined by electron microscopy (including three-dimensional imaging) and small-angle X-ray scattering, and a theoretical framework is proposed to describe strongly-segregated copolymer blends exhibiting the lamellar morphology. Results obtained here indicate that diblock copolymer blends of a given bulk composition may exhibit coexisting morphologies but in general behave as single-phase diblock copolymers of equal molecular composition, suggesting that such blends offer an alternative, and attractive, route by which to generate a desired morphology.

Introduction

Neat AB diblock copolymers undergo self-organization when the contiguous A and B monomer sequences are sufficiently incompatible, that is, when $\chi N \rightarrow (\chi N)_{ODT}$, where χ is the Flory–Huggins interaction parameter, N is the number of statistical units along the backbone, and the subscript denotes the order–disorder transition (ODT).[1] For $\chi N > (\chi N)_{ODT}$, the copolymer orders into a variety of periodic morphologies, depending on factors such as thermodynamic incompatibility (χN), molecular composition (f), and statistical segment length asymmetry.[2-4] Classical diblock copolymer morphologies include spheres of A (or B) arranged on a body-centered cubic (bcc) lattice in a matrix of B (or A), hexagonally packed cylinders of A (or B) in a matrix of B (or A), and alternating lamellae of A and B. More complex morphologies, such as the lamellar-catenoid/hexagonally perforated lamellar (LC/HPL)[5-7] and gyroid* (G*)[7-9] morphologies, have also been observed in neat diblock copolymers[10] and, more recently, in linear multiblock copolymers.[11] These "nonclassical" bicontinuous morphologies appear over narrow composition ranges separating the lamellar and cylindrical morphologies.

Efforts designed to establish molecule-morphology relationships in diblock copolymers have traditionally relied on model materials with highly tailored compositions and molecular weights. Synthesis of neat copolymers possessing particular compositions for morphological studies or morphology-specific applications is, however, laborious and, in many cases, not commercially viable. Several studies[12-16] have successfully shown that a desired morphology can be more readily generated by blending a diblock copolymer with a parent homopolymer. Blends of a lamellar poly(styrene-*b*-isoprene) (SI) copolymer and homopolystyrene (hS) have, for instance, yielded lamellae, a cubic bicontinuous morphology,[10] ordered cylinders/spheres, and disordered micelles, depending on blend composition. More recent studies have shown that additional nonclassical morphologies, such as the LC[16-18] and G*,[8] can be produced in the same fashion.

In essence, blending facilitates control over ultimate morphology by permitting continuous alteration of the minority component volume fraction. However, in copolymer/homopolymer blends, the mobility of the homopolymer residing within microdomains of the chemically identical block requires that homopolymer localization must also be considered. Theoretical frameworks[19-21] predict that the distribution of homopolymer A (hA) within an AB diblock lamellar morphology reaches a maximum near the center of each A microdomain, with the extent of localization depending on the molecular weight of hA relative to that of the host A block. Similar restrictions are believed to occur in nonlamellar morphologies, in which hA partitions into regions of the unit cell to relieve the stress associated with A-block stretching.[8] Although direct experimental confirmation of such localization has not been achieved in block copolymer melts, it has been observed[22] in nonlamellar morphologies of certain phospholipid–water systems.

* To whom correspondence should be addressed.
† North Carolina State University.
‡ Graduate Group in Biophysics, University of California.
§ Department of Biochemistry and Biophysics and the Howard Hughes Medical Institute, University of California.
⊥ The Procter & Gamble Co.
‖ Princeton University.
▼ Present address: Department of Chemical Engineering and Materials Science, University of Minnesota, Minneapolis, MN 55455.
⊗ Abstract published in *Advance ACS Abstracts*, April 15, 1996.

S0024-9297(95)01568-3 CCC: $12.00

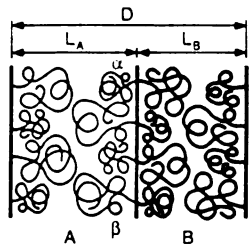

Figure 1. Schematic depiction of the lamellar morphology illustrating the chain placement and packing of a miscible copolymer/copolymer blend in which the constituent AB diblock copolymers possess different compositions but identical chain lengths ($N_\alpha = N_\beta$). By arbitrary convention, the A block of the α copolymer is shorter than that of the β copolymer (i.e., $f_{A\alpha} < f_{A\beta}$). Also shown here are the microdomain thickness (L_i, i = A or B) and periodicity (D).

Replacement of hA by a second strongly-segregated diblock copolymer forces one of the "homopolymer" chain ends in each A microdomain to locate in the AB interfacial region (see Figure 1) and introduces a similarly restricted B block into each B microdomain. Due to variations about the mean A and B block lengths in their respective microdomains, the ultimate morphology in such copolymer/copolymer blends is anticipated to be highly sensitive to chain packing and, hence, to the distribution of chain lengths within the blend. Since all of the copolymer molecules in such blends are anchored during microphase ordering, the morphologies generated in copolymer/copolymer blends are expected[23] to be more representative of those found in neat copolymers (of equal bulk composition) than those obtained in binary copolymer/homopolymer blends.

In this work, we examine the phase behavior of a series of copolymer/copolymer blends and explore the possibility of using blending[24] to tailor ultimate morphology. The blend morphologies produced here are characterized by transmission electron microscopy (TEM), intermediate voltage electron microscopic tomography (IVEM-T), and small-angle X-ray scattering (SAXS). We also describe a strong-segregation theoretical framework which addresses the microdomain characteristics of lamellar copolymer blends.

Experimental Section

Two SI diblock copolymers were synthesized *via* living anionic polymerization in cyclohexane at 60 °C. The initiator in each case was *sec*-butyllithium. According to proton nuclear magnetic resonance (^{1}H NMR), one of the copolymers (α) was symmetric (50 wt % S), while the other (β) was asymmetric (85 wt % S). Both copolymers possessed number-average molecular weights of 80 000 and polydispersities of approximately 1.04, as discerned by gel permeation chromatography (GPC). The mass of the S block in each copolymer was first measured by GPC upon consumption of all styrene monomer, and the mass of each I block was then determined from a combination of the overall $\bar{M}_n$ (GPC) and the molecular composition (^{1}H NMR). Physical blends were prepared in increments of 10 wt % α, ranging from pure α to pure β, and are designated hereafter by X/(100 − X) α/β, where X denotes the wt % of α. Films of the two copolymers and their blends were prepared from 5% (wt/v) solutions in toluene according to an earlier protocol for copolymer/homopolymer blends.[16] Upon slow solvent removal over the course of 3 weeks at ambient temperature and extensive annealing for 1 week at *ca.* 160 °C (which is well above the upper, styrenic, glass transition temperature in each parent copolymer), the films, measuring about 2 mm thick, were presumed to be near-equilibrium.

Electron-transparent specimens for TEM were obtained by sectioning the center of each film normal to the film surface at −100 °C in a Reichert-Jung Ultracut-S cryoultramicrotome. The resulting specimens were stained for 90 min with OsO_4 vapor from a 2% aqueous solution and examined using Zeiss EM902, Philips 430, and JEOL 200CX electron microscopes, operated at 80, 200, and 120 kV, respectively. Correlation maxima corresponding to reciprocal microdomain periods were measured from digitized electron micrographs upon Fourier transformation with Digitalmicrograph software (Gatan Inc., Pleasanton, CA). Three-dimensional reconstructions from IVEM-T data were obtained using a combination of customized and commercial software running on Silicon Graphics workstations (described later). Small-angle X-ray scattering was performed at Procter & Gamble with Cu Kα radiation (λ = 0.154 nm) generated from a Rigaku RU-300 rotating anode X-ray diffractometer operated at 40 kV and 200 mA with Kratky optics. Resulting patterns were not desmeared. Analogous measurements performed at Princeton University employed a Rigaku RU-200BH rotating anode instrument equipped with a 0.2 × 0.2 mm^2 microfocus cathode and Franks mirror optics. Samples were mounted inside an evacuated sample chamber and maintained at the temperature of interest by a set of thermoelectric devices with a temperature range of 0−185 °C and stability about the setpoint of ±0.05 °C. Two-dimensional diffraction images were collected with an image-intensified area detector designed around a Thompson CCD chip. After collection, images were digitized, corrected for detector response characteristics, and written to magnetic tape. Images were collapsed into a one-dimensional format by integrating azimuthally along an arc ±15° from the horizontal axis.

Results and Discussion

I. Neat Copolymer Phase Behavior. According to mean-field considerations,[1] the position of neat SI diblock copolymers in phase space is determined by thermodynamic incompatibility (χN) and volume-fraction composition (f_S). In SI block copolymer blends, the bulk volume fraction of S ($\langle f_S \rangle$) provides a measure of the sample composition,[14,15] which can be calculated from the known composition of the blend components, the concentration (X) of each in the blend, and the densities of polystyrene (ρ_S) and polyisoprene (ρ_I). We evaluate f_S and $\langle f_S \rangle$ at ambient temperature (ρ_S = 1.05 g/cm^3 and ρ_I = 0.91 g/cm^3) and at the polystyrene glass transition temperature (ρ_S = 1.00 g/cm^3,[25] and ρ_I = 0.84 g/cm^3,[26] at 100 °C). Corresponding values of f_S for the parent copolymers (denoted α and β, f_S = 0.46 for α and 0.83 for β) suggest that these materials possess lamellar and spherical morphologies, respectively.

Since χ and N are not expected to differ substantially for the two parent copolymers, the thermodynamic incompatibility can, for all practical purposes, be considered nearly constant throughout the present blend series. Due to uncertainty associated with the *a priori* calculation of χN, the degree of block copolymer segregation (i.e., weak, intermediate and strong) can be more generally described[27,28] in terms of the scaling behavior of microstructural dimensions (e.g., the microdomain periodicity) with respect to molecular weight, rather than by χN. Since the α and β copolymers employed here possess identical molecular weights, however, such analysis is not of value in the present study. Thus, on the basis of the molecular weights of the polymers, we expect that the neat α and β copolymers, as well as their blends, reside within either the intermediate- or strong-segregation regimes.

II. Blends Possessing the Lamellar Morphology. A. Experimental Observations. Figure 2 is a series of four SAXS profiles obtained from the 100/0, 90/10, 80/20, and 70/30 (SI)$_\alpha$/(SI)$_\beta$ blends in which Iq^2 is plotted against q, where I is scattering intensity and q denotes scattering vector. All of these profiles reveal that (i)

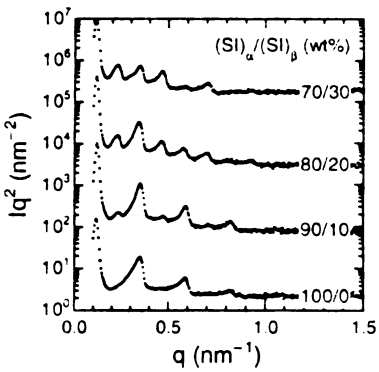

Figure 2. Small-angle X-ray scattering profiles (Iq^2 *vs* q, where I denotes scattering intensity and q is the scattering vector) collected from α/β blends ranging in X from 100% (bottom) to 70% (top) in 10% increments. From the peak spacing ratios, these α-rich blends exhibit the lamellar morphology. As in subsequent figures, the blend profiles are shifted vertically to facilitate peak discrimination.

the blends possess the lamellar morphology, since the peaks are equally spaced, and (ii) the lamellar microdomains possess reasonable long-range order, as evidenced by up to 7 orders of reflections. Note that the position of the first (maximum) scattering peak (q^*) is relatively close to the beamstop, near the left edge of each profile (at approximately 0.12 nm^{-1}). Since q^* provides a measure of the microdomain periodicity ($D = 2\pi/q^*$, by Bragg's law), it is interesting to note that q^* remains virtually invariant in this series of blends, a feature which is consistent with the predicted[29,30] composition independence of D for neat lamellar copolymers. In the α copolymer, only the odd reflections are visible due to the compositional symmetry of the molecule.[31] As β copolymer is added, the even reflections are observed to increase gradually in scattering intensity as (f_S) deviates from 0.5. The peak intensities and spacings appear to be well-behaved to 80/20 α/β. In the profile corresponding to the 70/30 blend, however, the fifth reflection is not very pronounced, even though the sixth reflection clearly remains.

Electron micrographs of the four blends used to produce Figure 2 are displayed in Figure 3 and reveal that classical morphologies are present in only some of these blends. Alternating lamellae constitute the single microstructure observed in the pure α copolymer (Figure 3a) and the 90/10 blend (Figure 3b). While lamellar microdomains (verified through tilting) are predominant in the 80/20 blend (Figure 3c), Figure 3d reveals that small patches of dispersed isoprenic cylinders are also evident. The absence of diffraction characteristic of cylinders from the data in Figure 2 suggests that these cylinders occupy only a small fraction of the sample volume. The demarcation from lamellar to cylindrical microstructure appears to be gradual and is reminiscent of the lamellar → cylindrical order–order transition reported by Hajduk *et al.*[32] Note that the cylinders possess a noticeably larger cross-section than the isoprenic lamellae, which is consistent with the equilibrium coexistence of two dissimilar morphologies.

According to Matsen and Bates,[23] relatively broad morphology coexistence regions are stable between the lamellar and hexagonal morphologies in binary blends of diblock copolymers of equal N and different compositions. Unlike typical micrographs of macrophase-separated diblock copolymer blends,[33] though, the regions of cylindrical microstructure in Figure 3 tend to be small, sometimes consisting of less than 10 microdomains along a lamellar row (see Figure 3d). In some cases, single cylindrical microdomains residing in a lamellar matrix have been observed. Assuming narrow interfacial regions,[29] calculation of (f_S) from these micrographs ($\langle f_S \rangle = L_S/D$, where L_S denotes the width of the styrenic lamellae) yields styrenic volume fractions (±0.04) of 0.51 (100/0), 0.55 (90/10), and 0.58 (80/20). Corresponding estimates of (f_S) obtained from the bulk composition of the blend are in reasonably good agreement with these values (0.46, 0.50, and 0.53, respectively). It should be noted, however, that the S lamellae in close proximity to regions comprised of cylindrical microdomains appear broader than those that are representative of the blends.

In the 70/30 blend (Figure 3e,f), lamellar and cylindrical morphologies coexist. At this composition, the grains of dispersed cylinders (see Figure 3e) appear larger than those seen in the 80/20 blend (Figure 3d). Existence of dispersed cylinders in the 80/20 and 70/30 blends is unexpected and, indeed, somewhat surprising, since the lamellar and cylindrical morphologies are presumed to be separated by an ordered bicontinuous morphology of intermediate interfacial curvature and interfacial packing density.[8,14-16] Some features of the 70/30 blend morphology do, however, suggest that the morphology exhibits characteristics of both coexisting phases. For example, the micrograph presented in Figure 3f demonstrates that the microstructure present in this blend is capable of producing a relatively large $s = +1/2$ disclination, which is commonly seen in lamellar copolymers and copolymer blends. Upon close examination of Figure 3f, it is immediately clear that the microstructural elements responsible for this disclination are neither lamellar nor cylindrical, but belong to an intermediate (and, as of yet, unidentified) morphology. Another possibility is that the morphologies produced in the 80/20 and 70/30 blends are not representative of a narrow thermodynamically-driven coexistence region, but instead reflect kinetically trapped nonequilibrium microstructures. In the absence of a thermotropic phase transition in a given material, it is difficult to discern conclusively whether a given morphology is representative of equilibrium. Alternatively, if the coexisting microstructures are, in fact, at local equilibrium, the slightly different ratios of the two copolymer species which they would therefore contain might reflect imperfect mixing of the α and β copolymers during sample preparation, rather than thermodynamically-driven macrophase separation. Once microphase separation has occurred, redistribution of the α and β copolymers to eliminate inhomogeneities in concentration might be extremely slow in nonlamellar morphologies due to the transport of minority component blocks through the majority component domains. The structures observed in this case might then be in equilibrium as far as the *local* concentration of both diblock species is concerned; they would, however, be nonequilibrium in nature when the *global* free energy of the system is considered. We believe that, based on the well-developed long-range order exhibited by other blends in this series, the thorough mixing, solvent removal, and extensive annealing protocol employed during sample preparation results in near-equilibrium copolymer and blend morphologies. However, we recognize that we are unable to *prove* that this is indeed the case, and so we refrain from claiming at this time that we have identified biphasic regions in these binary diblock blends.[34]

B. Theoretical Considerations. Several theoretical formalisms capable of predicting the equilibrium

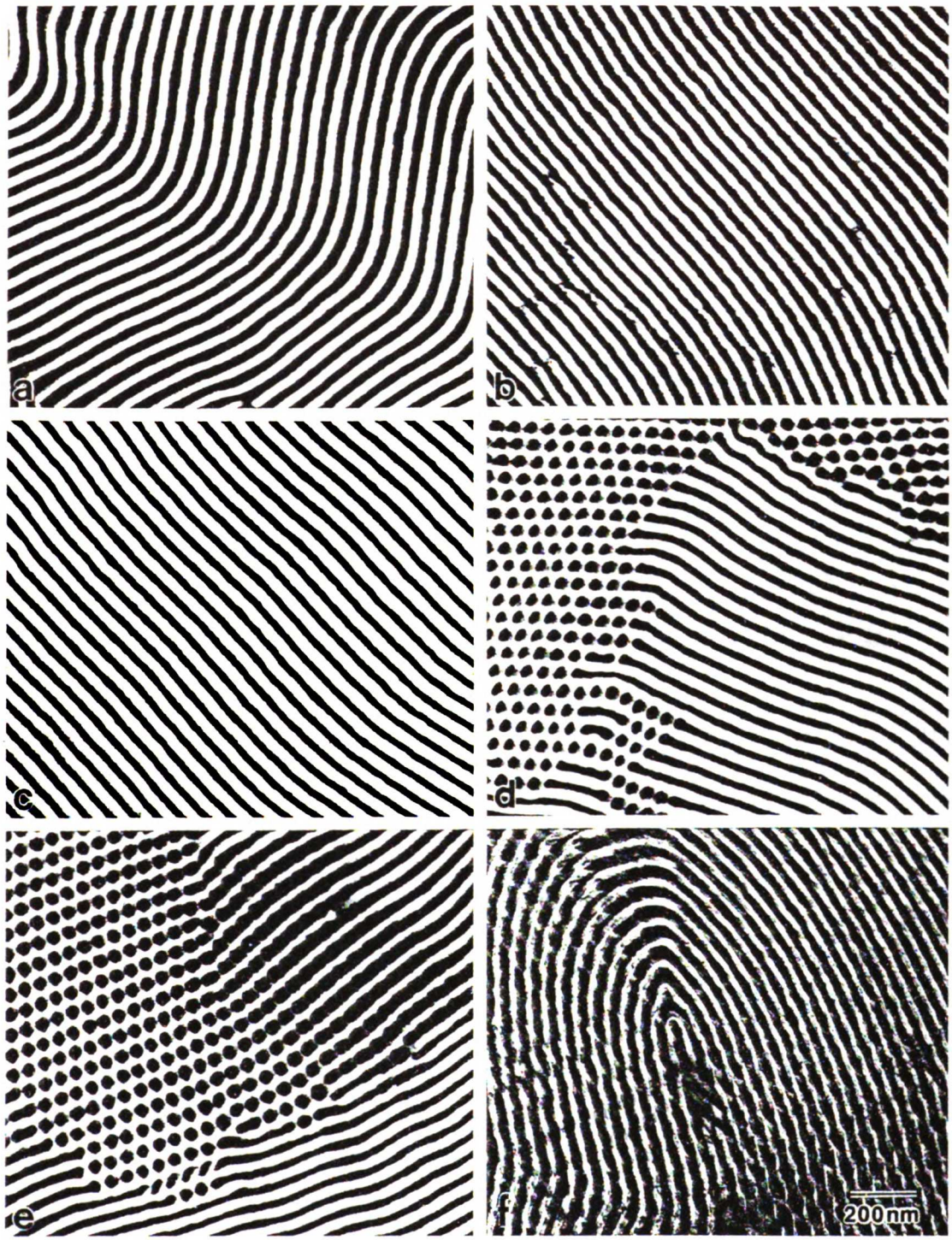

Figure 3. Series of transmission electron micrographs obtained from the same α-rich blends described in Figure 2. The 100/0 and 90/10 blends (a and b, respectively) clearly possess the lamellar morphology, while the 80/20 (c and d) and 70/30 (e and f) blends consist of lamellae and discrete grains of isoprenic cylinders. In (f), the 70/30 blend exhibits a relatively large $s = +1/2$ disclination. The isoprenic microdomains appear dark due to selective OsO_4 staining.

microdomain characteristics of copolymer/copolymer blend morphologies have recently been proposed.[35-39] One[37] of these extends the previous strong-segregation theories developed for neat diblock[40] and triblock[40,41] copolymers to include binary blends composed of lamellar diblock copolymers with equal (but not necessarily symmetric) compositions. A comparable formalism, as well as a self-consistent field (SCF) framework to

account for intermediate segregation in lamellar diblock copolymer blends, has also been presented by Matsen.[39] In this section, a strong-segregation framework is developed to address lamellar blends in which the constituent copolymers differ in composition, such as the ones presently examined and those investigated by Vilesov *et al.*,[12] so that predictions may assist in explaining the data in Figures 2 and 3.

In this framework, each lamellar microdomain is comprised of both α and β A (or B) monomers. Using the entropic expression suggested by Matsen[39] to describe stretching of the mixed α and β blocks along the lamellar normal and the narrow interphase approximation[29] to account for interfacial repulsion in the strong-segregation limit (while neglecting the entropy change due to *intra*lamellar mixing), the free energy per area (F) can be written as

$$\frac{F}{kT} = \frac{\pi^2}{4b^2}\left(\frac{H_A{}^3\psi'_A}{N_{A,\beta}{}^2} + \frac{H_B{}^3\psi'_B}{N_{B,\alpha}{}^2}\right) + 2b\left(\frac{\chi}{6}\right)^{1/2} \quad (1)$$

where k is the Boltzmann constant, T denotes absolute temperature, b is the monomer length (assuming $b_A = b_B$), H_i is the half-width of the ith lamella ($L_i = 2H_i$ in Figure 1), and $N_{i,j}$ is the number of monomers in the ith block (i = A or B) of the jth copolymer (j = α or β). Note that the $N_{i,j}$ are expressed in terms of the dominant block in the A and B microdomains. The factors ψ'_A and ψ'_B are given by

$$\psi'_A = \frac{R_A + (1 - R_A)(1 - x)^3}{[R_A + (1 - R_A)(1 - x)]^3} \quad (2a)$$

$$\psi'_B = \frac{R_B + (1 - R_B)x^3}{[R_B + (1 - R_B)x]^3} \quad (2b)$$

where $R_A = f_{A,\alpha}/f_{A,\beta}$ and $R_B = f_{B,\beta}/f_{B,\alpha}$, $f_{i,j}$ is the monomer (volume) fraction of i monomers in the jth copolymer ($f_{A,j} + f_{B,j} = 1$), and x is the mole fraction of α copolymer. In the specific case of constant chain length (i.e., $N_\alpha = N_\beta = N$), the mole fraction of α is equal to the mass fraction of α, and the total number of i monomers (i = A or B) occupying H_i is $N_i = \bar{f}_i N_\alpha$, where $\bar{f}_i = xf_{i,\alpha} + (1 - x)f_{i,\beta}$. From volume-filling considerations, it readily follows that $H_B = H_A\bar{f}_B/\bar{f}_A$ and $D = 2H_A/\bar{f}_A$.

Substitution of these relationships into eq 1, followed by algebraic manipulation, yields the free-energy density ($\mathcal{F}$), *viz.*,

$$\frac{\mathcal{F}}{kT} = \frac{\pi^2 D^2 \Psi}{32b^2 N^2} + \frac{2b}{D}\left(\frac{\chi}{6}\right)^{1/2} \quad (3)$$

where $\Psi = \psi'_A\bar{f}_A{}^3/f_{A,\beta}{}^2 + \psi'_B\bar{f}_B{}^3/f_{B,\alpha}{}^2$. Evaluation of $d\mathcal{F}/dD = 0$ provides the equilibrium lamellar period ($D_{\alpha\beta}$) as a function of both blend (x) and molecular ($f_{i,j}$) compositions:

$$D_{\alpha\beta} = \frac{4}{\sqrt{6}}\left(\frac{3}{\pi^2}\right)^{1/3} bN^{2/3}\chi^{1/6}\Psi^{-1/3} \quad (4)$$

Equation 4 closely resembles the expression derived[30] for the equilibrium period of either α or β lamellar copolymer ($D_\alpha = D_\beta$), in which case D_r for a blend of lamellar copolymers with equal N can be defined as $D_{\alpha\beta}/D_\alpha$ (or $D_{\alpha\beta}/D_\beta$) so that $D_r = \Psi^{-1/3}$. Note that as $x \to 0$ or $x \to 1$, $\Psi \to 1$ and $D_r \to 1$, which is consistent with the result[29,30] that D is independent of molecular composition for neat lamellar diblock copolymers in the strong-segregation regime. Since D from volume and mass conservation is equal to $2H_A/\bar{f}_A$, an analogous expression for the thickness of an A lamella in the blend, relative to that of the neat α copolymer, can be written as $L_{A,r} = \bar{f}_A D_r/f_{A,\alpha}$.

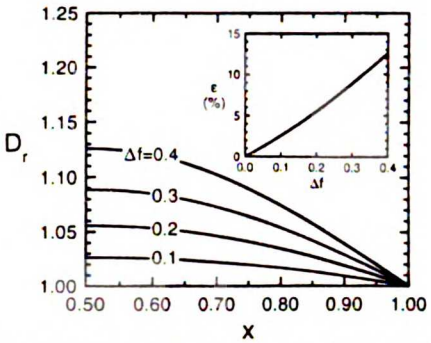

Figure 4. Predicted dependence of the reduced blend periodicity (D_r) on blend composition (x) for different copolymer asymmetries ($\Delta f = f_{A,\beta} - f_{A,\alpha}$, where, by convention, $f_{A,\alpha} < f_{A,\beta}$) in the strong-segregation limit. Maxima in D_r at $x = 0.5$ (ϵ) are presented as a function of Δf in the inset.

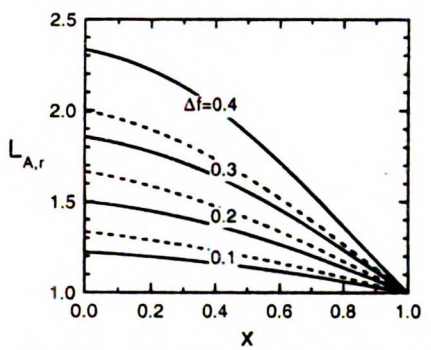

Figure 5. Predicted $L_{A,r}(x)$ for the two case examples described in the text. Type (i) blends (with $f_{A,\alpha} + f_{A,\beta} = 1$) are shown as solid lines, while type (ii) blends (with $f_{A,\alpha} = 0.3$) are displayed as dashed lines, for the same Δf.

Predicted D_r and $L_{A,r}$ are displayed as functions of blend composition (x) in Figures 4 and 5 for two case examples: (i) blends in which $f_{A,\alpha} + f_{A,\beta} = 1$ and (ii) blends with $f_{A,\alpha}$ held constant at 0.3. To facilitate comparison of these cases, blends are classified according to Δf, where $\Delta f = f_{A,\beta} - f_{A,\alpha}$ (recall from Figure 1 that, by convention, $f_{A,\alpha} < f_{A,\beta}$), and $\bar{f}_A$ is restricted to lie between 0.3 and 0.7. Since $D_r(x)$ is symmetric about $x = 0.5$, only half of the blend composition range is shown in Figure 4 to demonstrate that, as Δf increases from zero (the abscissa), D_r increases as x deviates from unity (or zero). The magnitude of the maximum in D_r at $x = 0.5$ [ϵ, where $\epsilon = (D_r - 1) \times 100\%$] is presented as a function of Δf in the inset of Figure 4 and is seen to increase nonlinearly from 0.0 (at $\Delta f = 0.0$) to ≈12.5% (at $\Delta f = 0.4$). An important point regarding these predictions is that they correspond to *both* of the cases described above. That is, $D_r(x)$ is only dependent on Δf, the difference between $f_{A,\alpha}$ and $f_{A,\beta}$, and not on $f_{A,\alpha}$ and $f_{A,\beta}$ individually, in the strong-segregation regime.

The same is not true, however, for $L_{A,r}$, provided as a function of x in Figure 5. As seen in this figure, predicted $L_{A,r}$ are sensitive to the characteristics of the two case examples examined here, with the (ii) blends ($f_{A,\alpha} = 0.3$) exhibiting larger $L_{A,r}$ than the (i) blends ($f_{A,\alpha} + f_{A,\beta} = 1$) of identical Δf. Another apparent difference between the predictions for $D_r(x)$ in Figure 4 and $L_{A,r}(x)$ in Figure 5 is that, for $\Delta f > 0$, predicted $L_{A,r}$ increase

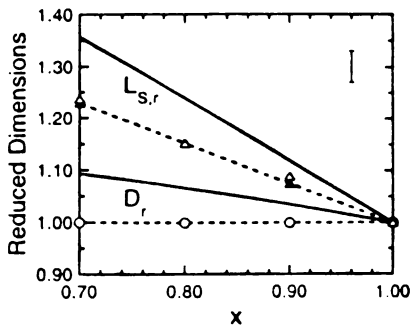

Figure 6. Comparison of experimental data ($f_{A,\alpha}$ = 0.46, $f_{A,\beta}$ = 0.83, and Δf = 0.37) and theoretical predictions for D_r and $L_{S,r}$. Experimental data points, D_r (circles) and $L_{S,r}$ (triangles), are derived from SAXS (open symbols) and TEM (filled symbols) measurements, whereas corresponding predictions from the strong-segregation formalism developed here are displayed as solid lines. The error bar (upper right corner) provides a measure of uncertainty in the SAXS data.

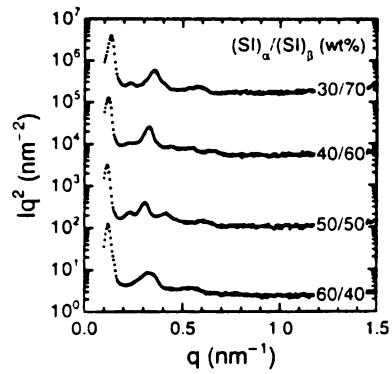

Figure 7. Series of SAXS profiles corresponding to (from bottom to top) the 60/40, 50/50, 40/60, and 30/70 α/β blends. As X decreases (and $\langle f_S \rangle$ increases), the blends undergo a transition from a bicontinuous morphology (60/40) to hexagonal morphologies (50/50 to 30/70).

monotonically from unity with decreasing x. That is, while $D_r(x)$ curves are symmetric about, and display a maximum at, x = 0.5, each $L_{A,r}(x)$ curve reaches a maximum at x = 0.0. This behavior is consistent with the arbitrary convention established in Figure 1, namely, $f_{A,\alpha} < f_{A,\beta}$, in which case the neat α copolymer possesses a shorter A block than the β copolymer. Addition of β copolymer to the α copolymer results in an increase in the width of the A lamellae due to an increase in the number of resident A monomers. The maximum in $L_{A,r}(x)$ must therefore occur when $\bar{f}_A = f_{A,\beta}$, in the limit of pure β (x = 0.0).

In Figure 6, A is taken to correspond to S so that experimental and predicted values of D_r and $L_{S,r}$ can be compared for the lamellar α/β blends ($0.7 \le x \le 1.0$) examined in this study. Since only the neat α copolymer is lamellar, the microstructural dimensions of interest must be normalized with respect to those of the α copolymer; i.e., $D_r = D_{\alpha\beta}/D_\alpha$ and $L_{S,r} = L_{S,\alpha\beta}/L_{S,\alpha}$, where $L_{S,\alpha\beta} = \langle f_S \rangle D_{\alpha\beta}$ from SAXS measurements. Recall from section I that $f_{S,\alpha}$ and $f_{S,\beta}$ (needed for evaluation of Ψ and $\bar{f}_S$, and consequently D_r and $L_{S,r}$) are about 0.46 and 0.83, respectively, in which case Δf = 0.37. As is evident from Figure 6, D_r and $L_{S,r}$ obtained from the strong-segregation formalism developed here clearly overpredict the reduced SAXS data (by as much as 10% at x = 0.7). Three important points must be remembered at this juncture. The first is that the uncertainty in the SAXS data is about 3%, while that in the TEM data is as much as ≈4%. While such uncertainty does not solely account for the difference between theoretical predictions and experimental data, it must be considered in this comparison. The second is that, while N_α and N_β are comparable in magnitude in the present study, they are not identical, as required in the theoretical formalism proposed here.

Thirdly, the framework presented in this work assumes strong-segregation behavior in the limit as $\chi N \to \infty$. With molecular weights of 80 000 each, the α and β copolymers (and, hence, their blends) possess finite χN values and reside in either the intermediate- or strong-segregation regime, which is more accurately described by SCF theory. Due to the assumption of a single chain trajectory along the lamellar normal in strongly-segregated block copolymers,[20,37,39-41] lateral microstructural dimensions (e.g., D) predicted from strong-segregation formalisms tend to be larger than those obtained from SCF frameworks. Matsen,[39] for instance, reports that predicted D for symmetric copolymer blends (Δf = 0 and $N_\alpha > N_\beta$) in the strong-segregation approximation consistently exceed those obtained from SCF analysis (by as much as about 10% when N_β/N_α = 0.25). An interesting feature of Figure 6 is that D_r from SAXS measurements are invariant with respect to x, while predicted D_r in the strong-segregation limit increase monotonically (over $0.7 \le x \le 1.0$) as x decreases from unity.

III. Blends Possessing Nonlamellar Morphologies. A. Conventional SAXS/TEM Analyses. A series of SAXS profiles obtained from the 60/40, 50/50, 40/60, and 30/70 blends is shown in Figure 7 and, unlike the profiles seen in Figure 2, reveals an evolution in morphology as the blends go from being α-rich to β-rich. Corresponding changes in morphology with blend composition are likewise evident in the electron micrographs presented in Figure 8. The SAXS profile corresponding to the 60/40 blend, for instance, is weakly similar to profiles previously reported for ordered bicontinuous morphologies, such as the G*.[8,43] One of the scattering characteristics of this cubic bicontinuous morphology is the existence of peaks at spacing ratios of $\sqrt{3}$:$\sqrt{4}$, typically appearing as an intense peak immediately followed by a secondary peak or discrete shoulder, depending on instrument resolution. A high-resolution SAXS profile obtained from the 60/40 blend is presented in Figure 9a. A shoulder appears on the outside of the principal reflection at an approximate position ratio of $\sqrt{8}/6$ with respect to the lowest diffraction order, consistent with the cubic microstructural assignment. The incoherent signal extending from q = 0.24 to 0.36 nm^{-1} obscures any coherent scattering in this range, although poorly resolved reflections might be present in the vicinity of q = 0.24 nm^{-1}; this would correspond to peaks at position ratios between $\sqrt{20}$ and $\sqrt{28}$, if the principal reflection is assigned $\sqrt{6}$. A strong reflection appears at a position ratio of $\sqrt{54}$, or 3 times the spacing of the principal reflection. As such a strong peak is not normally seen at this position in diffraction from the G* morphology, this feature might indicate the coexistence of a poorly ordered cubic phase with a layered structure of some sort.

Unambiguous identification of the microstructure of this blend is not possible due to the limited number of poorly resolved diffraction orders. An electron micrograph of the 60/40 blend in Figure 8a reveals that the blend morphology is bicontinuous and strikingly

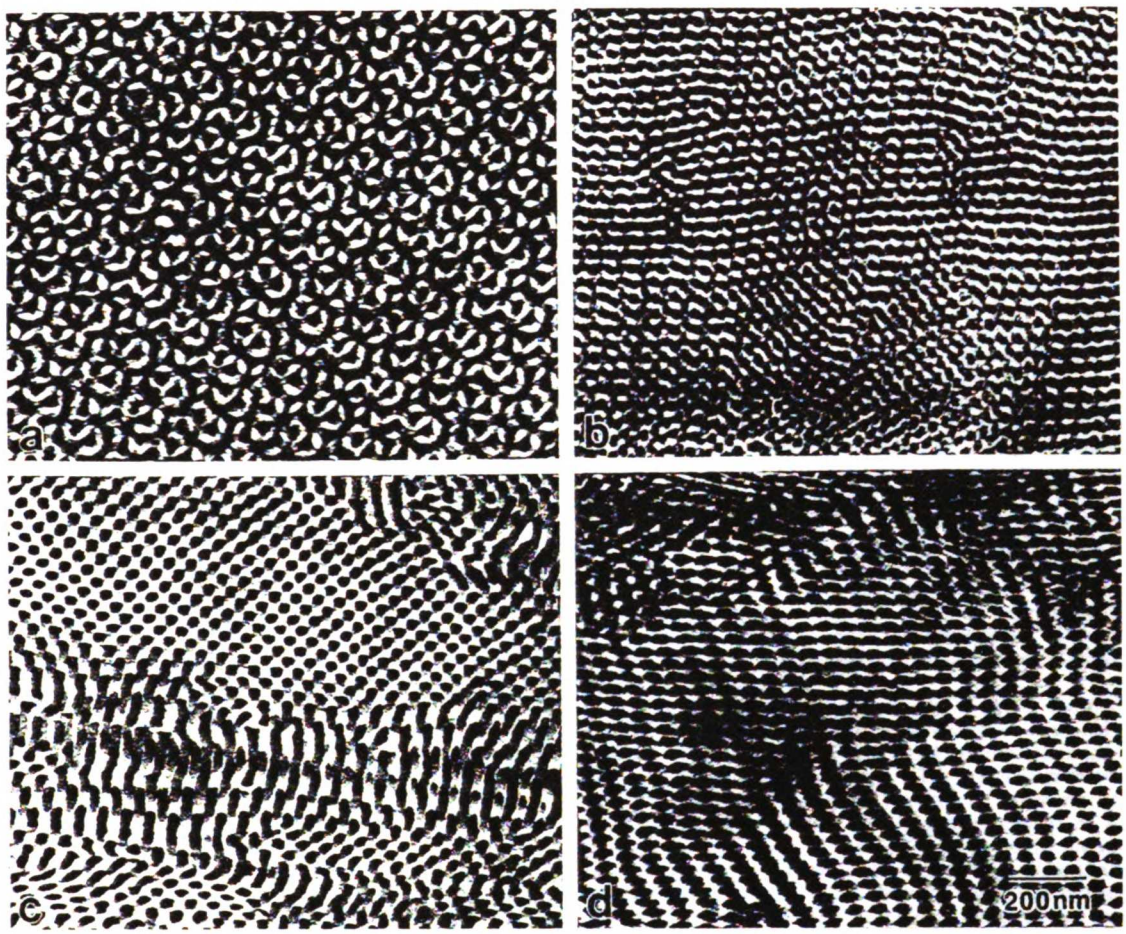

Figure 8. Electron micrographs of the four blends described in Figure 7. A projection from the bicontinuous morphology produced in the 60/40 blend is shown along the [111] axis[44,60] in (a), whereas the morphology found in the 50/50 blend is displayed in (b). The cylindrical morphology is clearly evident in the 40/60 (c) and 30/70 (d) blends.

reminiscent of the double-diamond and G″ morphologies in projection along the [111] axis[44,60] (Figure 8a). This blend exhibits two important characteristics: (i) the morphology seen in Figure 8a is the only one present and (ii) the morphology is highly oriented, even in the absence of shear-induced alignment.[45] These features both suggest that the α and β copolymers are miscible at the molecular level, at least at this composition (61 vol % S, which coincides with the appearance of cubic bicontinuous morphologies in neat starblock copolymers[43,46]). Similar observations have been reported by Schwark,[47] who found that a blend of a lamellar copolymer and a copolymer possessing the cylindrical morphology could yield a bicontinuous morphology. While the thermodynamic stability of bicontinuous morphologies has recently become the subject of immense theoretical interest,[48,49] no attempt is made here to extend the framework proposed in the previous section to blends displaying nonlamellar morphologies.

According to the SAXS profile displayed in Figure 7, the 50/50 blend consists of the cylindrical morphology, as evidenced by the appearance of peaks at spacing ratios of $1:\sqrt{3}:\sqrt{4}$. This is confirmed in the high-resolution profile shown in Figure 9b, although the broad peaks evident in this figure are suggestive of a distorted lattice with relatively little long-range order. In contrast, the corresponding electron micrograph in Figure 8b suggests that this blend consists of coexisting morphologies, one interconnected, possibly bicontinuous, and the other cylindrical. Localized regions of discrete cylindrical microdomains are, for instance, evident in Figure 8b. The absence of a diffraction signature characteristic of a bicontinuous structure despite the highly ordered nature of that phase as seen in the micrographs suggests that this morphology occupies a very small fraction of the sample volume. These data differ from those corresponding to the 40/60 and 30/70 blends, which, according to the SAXS profiles in Figure 7 and the electron micrographs in Figure 8c,d, respectively, consist solely of hexagonally-packed isoprenic cylinders. Comparison of Figure 8c,d to those presented in Figure 3c–f reveals that the cylindrical microdomains in the 40/60 and 30/70 blends are much smaller than those observed in the 80/20 and 70/30 blends. According to measurements obtained from these and similar micrographs, values of $\langle f_S \rangle$ are estimated (±0.02) from the cylindrical (not lamellar) microdomains to be about 0.73 (80/20), 0.65 (70/30), 0.68 (40/60), and 0.70 (30/70), and corresponding values of $\langle f_S \rangle$ calculated from the blend composition are 0.53, 0.57, 0.68, and 0.71, respectively. Thus, the cylindrical morphologies evident in the I-rich (one-phase) blends are consistent with the blend compositions and full α/β miscibility, whereas those in the S-rich (two-phase) blends are β-rich and conse-

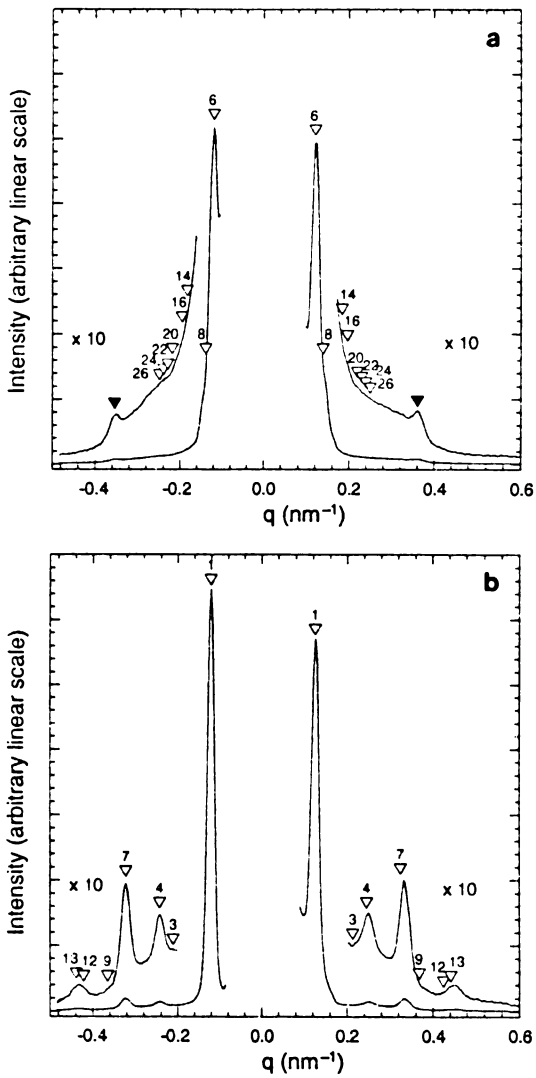

Figure 9. High-resolution SAXS profiles obtained from the (a) 60/40 and (b) 50/50 blends. Inverted triangles in (a) indicate expected peak position ratios for the first few orders of the G* morphology; they do not indicate locations where peaks are actually observed. The reflection marked with the unlabeled filled symbol appears at 3× the spacing ratio of the principal diffraction order. Inverted triangles in (b) indicate similar positions for the hexagonally packed cylindrical morphology. The label on each triangle gives the square of the peak position ratio (modulus).

quently reflect a spatially inhomogeneous distribution of copolymers. Again, we note that we are unable to determine whether these spatial inhomogeneities are equilibrium in nature.

B. Electron Tomographic Analysis. To reconcile the apparent contradiction between SAXS and TEM concerning the 50/50 blend, as well as examine the cubic bicontinuous morphology in the 60/40 blend, electron tomography has been performed to more carefully scrutinize the three-dimensional microstructures of these blends.

Electron microscopic tomography allows the complete three-dimensional internal structure of an object to be reconstructed from a set of tilted views, without imposing any *a priori* assumptions or requirements regarding the symmetry of the object. This powerful approach has been proven to be extremely valuable in the analysis of complex biological structures such as chromosomes,[50] centrosomes,[51] kinetochores,[52] and cilia.[53] Detailed descriptions of the filtered (*r*-weighted) back-projection imaging technique are available elsewhere,[54-58] and only the general approach and pertinent operating parameters are included here. A series of 49 480 × 480 pixel images of an area of interest from a single TEM section were digitally collected at a resolution of 2.1 nm/pixel using 2× binning on a Thompson 1024 × 1024 CCD chip fiber-optically coupled to a single crystal scintillator. Data were collected at tilt angles ranging from +60° to −60° in 2.5° increments. Examples of the images at six different tilt angles are shown in Figure 10. To minimize radiation damage, specimen exposure to the electron beam was limited to image acquisition and focusing using recently developed automated data collection methods that dynamically track changes in sample position and focus during tilting.[57] The images were first converted to mass density (mass-normalization) and then aligned with respect to fiducial markers (30 nm colloidal gold beads) using a least-squares minimization algorithm.[54] Using the EMCAT reconstruction software package,[58] the 3-D volume was reconstructed from the collected projections. Image display and analysis was conducted using the PRIISM image graphics package.[59]

Two reconstructions were performed, one of the 60/40 blend (with the bicontinuous, probably G*, morphology) and the other of the 50/50 blend (with the hexagonal, cylindrical-like morphology). The mean alignment error (σ), averaged over all of the fiducial markers (at least 8) used in aligning the images, is shown as a function of tilt angle for the 60/40 and 50/50 blend reconstructions in Figure 11a,b, respectively. Note that the overall mean error is less than the resolution of the collected images. Lateral sample shrinkage, due to electron radiation damage, is estimated to be about 2.7 and 2.1%, respectively, as discerned from the relative positions of the fiducial markers immediately before and after acquisition of the tilt series. Alignment errors (Figure 11) and lateral shrinkage measurements provide a quantitative assessment of radiation-induced specimen damage. The extent of beam damage can also be qualitatively discerned by comparing the morphological features of images collected at 0° tilt before and after the tilt sequence. In this work, such image pairs are virtually indistinguishable. Solid renderings of the reconstructed 60/40 blend morphology are displayed at different orientations from −20° to +200° rotation (in 20° increments) in Figure 12. The bicontinuous cubic morphology in this figure consists of a network of *ca.* 20 nm channels which closely resemble the constant mean-curvature surfaces often employed[8,43,44,60] to simulate two-dimensional (TEM) projections of complex cubic morphologies. Note, however, that the morphology seen in Figure 12 cannot be readily described by a surface with precise symmetry (and mathematical properties) due to microstructural imperfections. Since the morphology is discerned experimentally, it is representative of a physically real structure, incorporating all of the naturally occurring (and potentially property-limiting) defects associated with microphase ordering.

Even with the irregularities present, it is clear from the reconstructed images displayed in Figure 12 that the 60/40 blend is bicontinuous, although its symmetry group ($Pn\bar{3}m$ for double-diamond *vs* $Ia\bar{3}d$ for G*) cannot be clearly identified. Since these morphologies differ

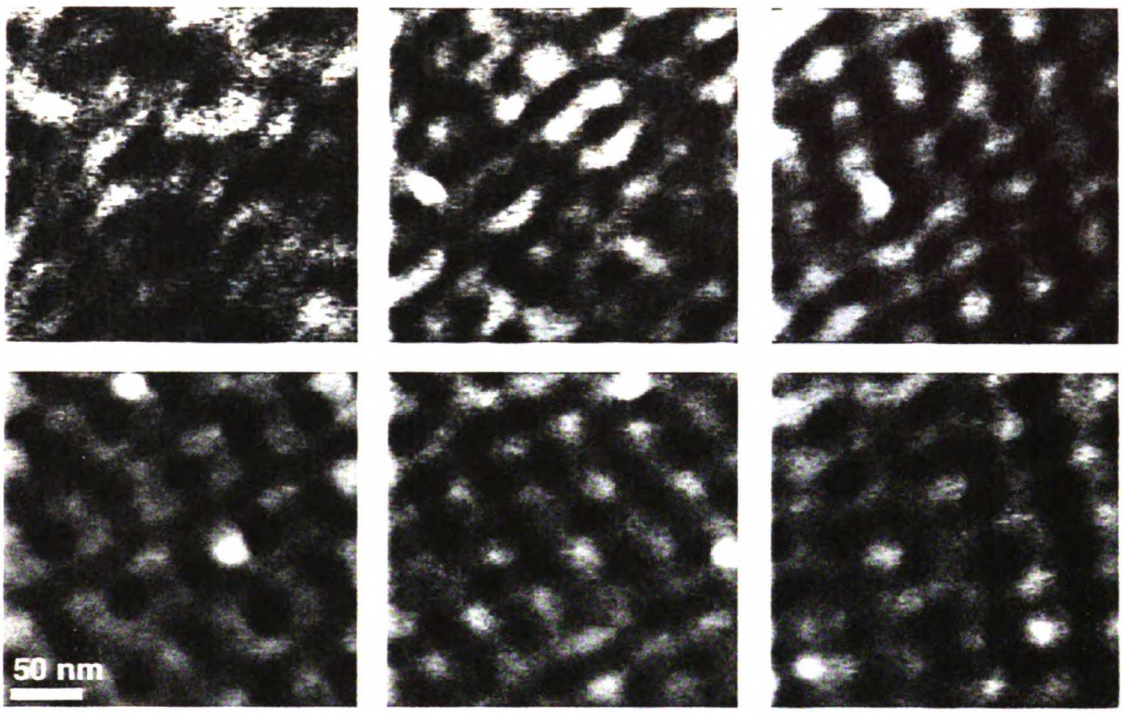

Figure 10. Digital electron micrographs of the 60/40 blend collected at six different tilt angles ranging from −45° to +30° in 15° increments from left to right and top to bottom. These images are contrast-reversed, in which case the S and I microphases appear dark and light, respectively.

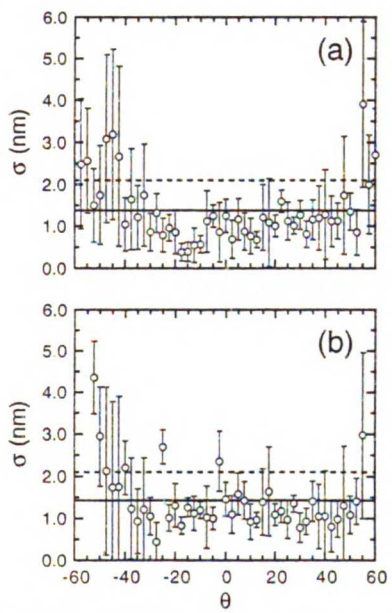

Figure 11. Mean error in fiducial marker position (σ) incurred during alignment of tilt projections for 3-D reconstructions of the (a) 60/40 and (b) 50/50 blends. The vertical lines denote standard deviations in the data, while the solid and dashed lines correspond to the angle-averaged overall error and image resolution (per pixel), respectively.

in the coordination of the minority component channels—the double-diamond network is built from four-connected tetrahedral elements, while the G* structure is based on three-connected channels—differentiation of these phases can be achieved by counting the number of minority component "tubes" which join at a vertex of the reconstructed morphology. From images such as those presented in Figure 12, the number of connected channels intersecting at each vertex is 3. In a related work,[11] the G* morphology has been unambiguously identified by both SAXS and TEM. Figure 13 is a series of two-dimensional images sliced from the reconstructed volume element of the 60/40 blend morphology along two different directions: normal to the electron beam path (small images) and parallel to the electron beam path (large image). If z is perpendicular to the specimen surface, each small image in Figure 13 consists of projected information from an incremental specimen thickness Δz, where $\Delta z \approx 21$ nm. [Since cryoultramicrotomy routinely produces specimens ranging from 60 to 100 nm in thickness, acquisition of a complete set of comparable images from conventional TEM free of sectioning distortions would be an impossible task.] The large image in Figure 13 shows the TEM specimen in cross-section, with the vertical axis corresponding to the z-axis. Upon comparison of the images shown in Figures 12 and 13 to the model surfaces provided in ref 8, the morphology produced in the 60/40 blend is probably G*.

Reconstructed images similar to those provided for the 60/40 blend in Figure 12 are presented in Figure 14 for the 50/50 blend and reveal that this blend consists of hexagonally packed cylinders which appear elliptical, rather than circular, in cross-section (in agreement with the SAXS data presented in Figure 9b). The major and minor elliptical axes measure about 50 and 30 nm, respectively, across. As is evident from the cross-sectional view, some of the cylinders also appear to be connected laterally, suggesting that the morphology may

Figure 12. Three-dimensional images of the 60/40 blend obtained through electron tomography. Solid renderings are displayed here at rotation angles ranging from −20° to +200° (in 20° increments from left to right and top to bottom) to facilitate visualization of the bicontinuous channel network comprising this morphology. Note that three channels intersect at each vertex.

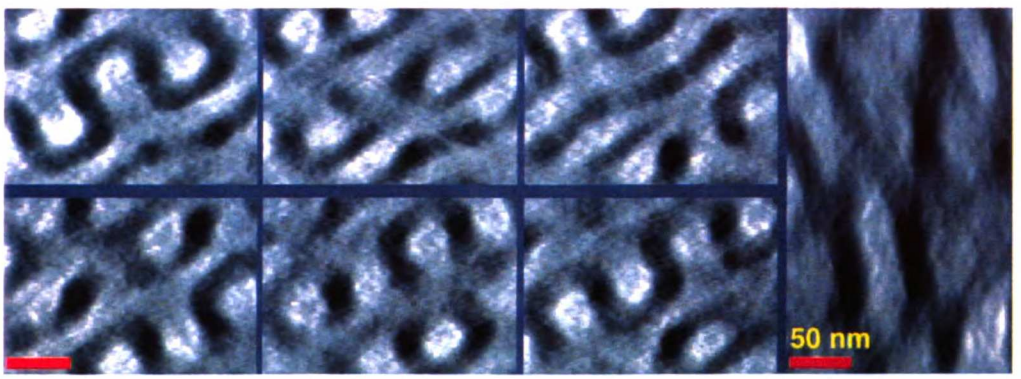

Figure 13. Two-dimensional images sliced from the reconstructed morphology presented in Figure 12. The thickness of each contrast-reversed "slice" in the six small images (sequential from left to right and top to bottom) is about 21 nm along the electron beam axis, whereas the large single image is a cross-section of the TEM specimen.

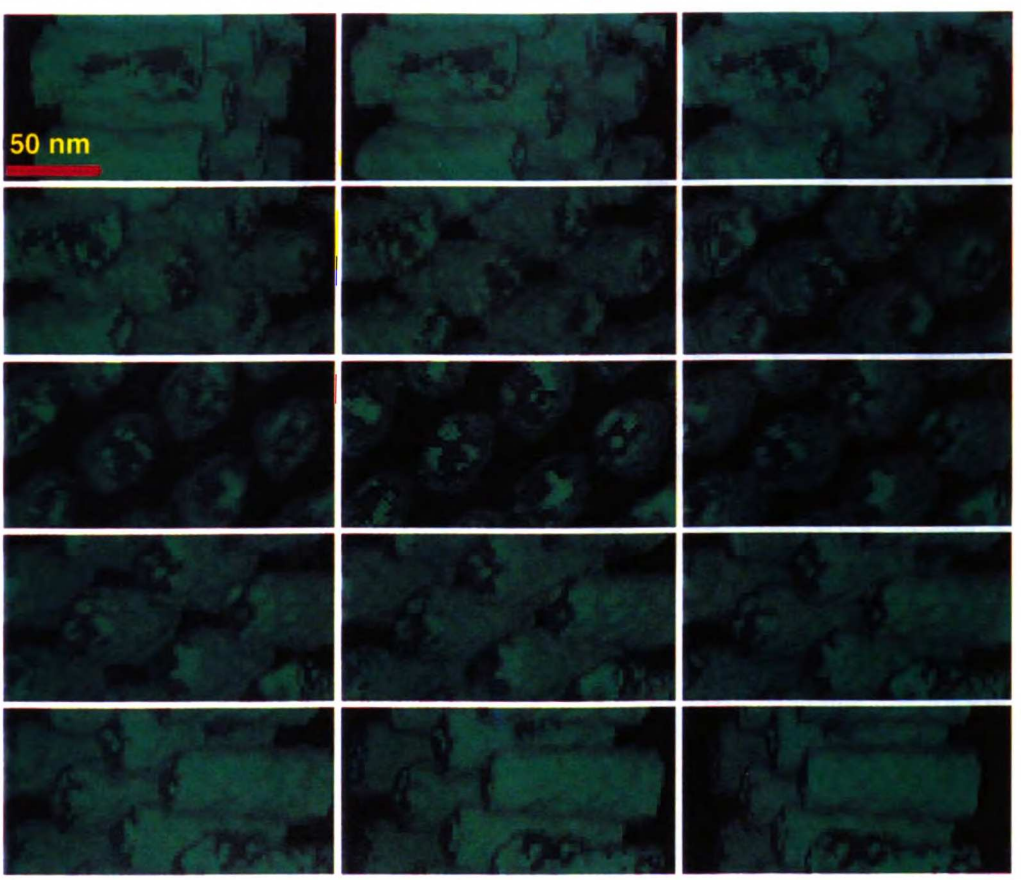

Figure 14. Three-dimensional reconstructions of the 50/50 α/β blend demonstrating that the morphology consists of hexagonally packed cylindrical microdomains which appear elliptical in cross-section. The images are rotated from $-70°$ to $+70°$ in $10°$ increments (left to right and top to bottom). Some of the cylinders are laterally connected, suggesting that this morphology may be related to the hexagonal "channel" morphologies recently reported.[6]

be related to one of the "channel" morphologies proposed by Hamley *et al.*[6] To ensure that the images in Figures 12 and 14 are representative of the microstructure in the 60/40 (Figure 12) and 50/50 (Figure 14) blends, the pixel levels in these solid reconstructions have been thresholded so that $\langle f_S \rangle$ lies between 0.50 and 0.65

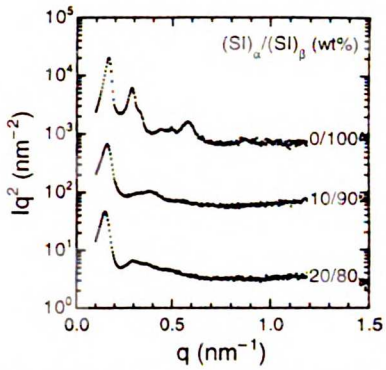

Figure 15. Scattering profiles obtained from the 20/80 (bottom), 10/90 (middle), and 0/100 (top) blends. Patterns corresponding to the two β-rich blends indicate the absence of higher-order scattering maxima, suggesting that the morphologies do not possess long-range order. The β copolymer exhibits a spherical morphology according to the SAXS profile shown here.

(values of $\langle f_S \rangle$ estimated from the known blend composition are 0.61 and 0.64, respectively). A notable feature of the microstructure in Figure 14 is the highly aligned nature of the major axes of the ellipses. Such alignment is unlikely to be microstructural in origin, considering the 6-fold rotational degeneracy of the underlying hexagonal lattice. Instead, it may have been induced by the sample preparation process. However, we note that the hexagonal lattice does not appear highly distorted (as it would upon mechanical deformation during microtomy) and that the microstructural elements are best described as elliptical in cross-section.

IV. Styrene-Rich Blends Possessing Cubic Morphologies. Further reduction in the isoprene concentration induces a transition from the cylindrical morphology to an irregular (possibly bicontinuous) morphology, as seen in the SAXS profiles provided in Figure 15 and the electron micrographs in Figure 16. This morphology, apparent in the 20/80 and 10/90 blends, is characterized by the absence of well-defined higher-order scattering reflections (Figure 15) and by the presence of highly interconnected isoprenic microdomains (see Figures 16a,b). It is similar in appearance to the "mesh" (or "strut") morphology reported by Hashimoto *et al.*,[61] and can be envisioned as an intermediate morphology comprised of randomly oriented, short stubby cylinders. Such morphologies have been observed[62] in aqueous surfactant systems at compositions between those yielding the cylindrical (hexagonal) and spherical (cubic) morphologies. The neat β copolymer (0/100) consists principally of dispersed isoprenic spheres on a body-centered cubic (BCC) lattice, as identified by the scattering reflections at $1:\sqrt{3}:\sqrt{4}:\sqrt{7}:\sqrt{12}$ in Figure 15 and the micrograph in Figure 16c.

As this study has demonstrated, blends comprised of two ordered diblock copolymers with dissimilar compositions (and morphologies) can be used to alter, and ultimately control, copolymer morphology and microstructural dimensions (see Table 1). As noted earlier, D from the lamellar and bicontinuous (intermediate) morphologies remains nearly constant, and then decreases by as much as 28% when X drops below 50% α (and the blends become isoprene-rich). In contrast, L_S increases with decreasing X, reflecting the existence of swollen S lamellae in asymmetric lamellar α/β blends. Note that the blend composition corresponding to the bicontinuous morphology ($\langle f_S \rangle \approx 0.61$) is in excellent

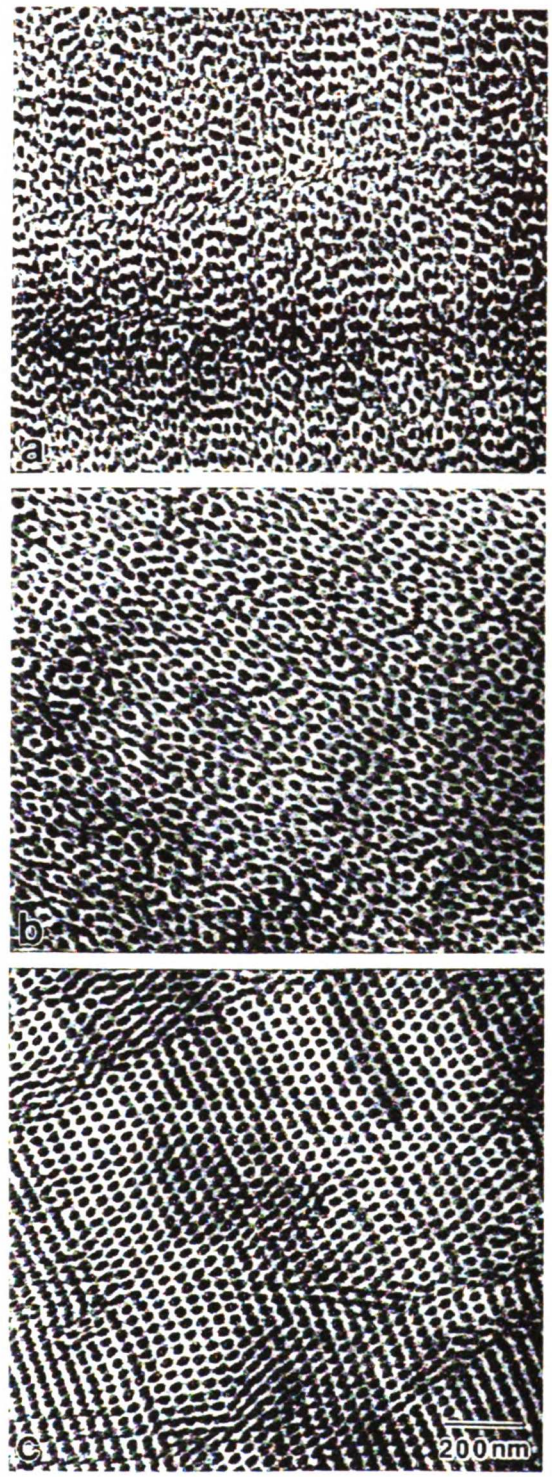

Figure 16. Series of electron micrographs imaged from the blends described in Figure 15. As expected from the corresponding SAXS profiles, the (a) 20/80 and (b) 10/90 blends exhibit an irregular morphology which, from these projections, consists of dispersions and an interconnected network, whereas the neat β copolymer (c) is comprised principally of dispersed isoprenic spheres.

Table 1. Microstructural Dimensions and Morphologies of the $(SI)_\alpha/(SI)_\beta$ Blends Examined Here

X	W_S	$\langle f_S \rangle^a$	D^b (nm)	D^c (nm)	$L_S{}^d$ (nm)	$L_S{}^e$ (nm)	morphology
100	0.50	0.46	53.2	48.5	24.5	24.7	lamellar
90	0.53	0.50 (0.49)	53.2	48.5	26.7 (26.1)	26.6	lamellar
80	0.57	0.53	53.2	48.5	28.2	28.4	lamellar/cylindrical
70	0.61	0.57 (0.56)	53.2	48.5	30.3 (29.8)	30.3	lamellar/cylindrical
60	0.64	0.61 (0.60)	53.2				bicontinuous (G*)
50	0.68	0.64	53.2				(elliptical) cylindrical
40	0.71	0.68 (0.67)	50.3				cylindrical
30	0.75	0.72 (0.71)	47.6				cylindrical
20	0.78	0.75	43.1				(irregular) mesh
10	0.82	0.79	39.3				(irregular) mesh
0	0.85	0.83	37.7				spherical

[a] Calculated at 25 °C (100 °C) using the densities given in the text. [b] Determined from the principal peak position in SAXS patterns (±3% for lamellae). [c] Measured from 2-D Fourier-transformed TEM images (±3%). [d] Calculated from $\langle f_S \rangle D$ at 25 °C (100 °C). [e] Measured from digital TEM images in Digital Micrograph (±4%).

agreement with that yielding the G* morphology in neat starblock copolymers.[43,46] This comparison suggests that binary copolymer blends behave more like neat copolymers than do copolymer/homopolymer blends,[14-16] in which microphase bicontinuity arises when $\langle f_S \rangle$ lies between 0.65 and 0.67. As X is increased further, the bicontinuous morphology gives way first to isoprenic cylinders and then to a (mesh-like) morphology lacking long-range periodic order. As $X \rightarrow 0$, the spherical morphology characteristic of the β copolymer is recovered. Such physical, rather than chemical, synthesis[24] provides an ideal opportunity to study the conformational properties of mixtures of bimodal distributions of grafted polymer chains confined to nanoscale microstructures with and without curvature.[63]

Conclusions

While previous efforts have focused on controlling block copolymer morphology through the addition of a parent homopolymer, the SAXS and TEM results presented here indicate that blends of two strongly segregated copolymers possessing dissimilar morphologies can effectively be used to produce intermediate morphologies which are more representative of neat copolymers of equivalent bulk composition. Addition of an asymmetric β copolymer exhibiting isoprenic dispersions to a symmetric α copolymer initially induces swelling of the styrenic lamellae, the extent of which can be reasonably well-predicted by a strong-segregation formalism proposed here for compositionally heterogeneous lamellar copolymer blends. As the concentration of β is increased further, coexisting grains of cylinders are observed to form within a lamellar matrix, suggesting that macrophase separation occurs between the α and β copolymers even though the molecular weights of the constituent copolymers are comparable. If the coexisting morphologies are equilibrium in nature, developing from an initially isotropic distribution of the blend components, this phase separation arises as a consequence of this coexistence. In some cases, the cylindrical grains are extremely small, consisting of only a few (<10) microdomains. Upon further addition of β, a well-oriented bicontinuous morphology develops, followed by a hexagonal intermediate morphology comprised of elliptical (and sometimes connected) cylinders. Electron microscopic tomography has been employed here to provide the first three-dimensional images of these morphologies at high spatial resolution. Observed morphologies in β-rich blends include the classical cylindrical morphology and a disordered bicontinuous morphology. These results demonstrate that binary block copolymer blends can be used to generate intermediate morphologies, without resorting to tailored chemical synthesis, and provide valuable insight into the molecular mixing of spatially confined chains grafted to a repulsive interface.

Acknowledgment. This study has been supported by the Petroleum Research Fund, administered by the American Chemical Society, the National Science Foundation (CMS-941-2361), and the Director, Office of Energy Research, Office of Basic Energy Sciences, Materials Science Division of the U.S. Department of Energy under contract DE-AC03-76SF00098. R.J.S. thanks the National Center for Electron Microscopy for a Visiting Scientist Fellowship and Drs. K. M. Krishnan and U. Dahmen for valuable discussions. Work at Princeton University was supported by the U.S. Department of Energy under contract DE-FG02-87ER60522 and the National Science Foundation (DMR-922-3966). Funding for D.A.A., J.W.S., M.B.B., and J.C.F. was provided by the Howard Hughes Medical Institute and the National Institute of Health (GM31627, D.A.A.; GM25101, J.W.S.). We are grateful to Mr. H. Chen (UCSF), Mr. J. T. Grothaus (P&G), and Mr. M. A. Burchfield (P&G) for technical assistance.

References and Notes

(1) Leibler, L. *Macromolecules* **1980**, *13*, 1602.
(2) Fredrickson, G. H.; Bates, F. S. *Annu. Rev. Phys. Chem.* **1990**, *41*, 525.
(3) Hamley, I. W.; Gehlsen, M. D.; Khandpur, A. K.; Koppi, K. A.; Rosedale, J. H.; Schulz, M. F.; Bates, F. S.; Almdal, K.; Mortensen, K. *J. Phys. II* **1994**, *4*, 2161.
(4) Gehlsen, M. D.; Bates, F. S. *Macromolecules* **1994**, *27*, 3611.
(5) Thomas, E. L.; Anderson, D. M.; Henkee, C. S.; Hoffman, D. *Nature* **1988**, *334*, 598.
(6) Hamley, I. W.; Koppi, K. A.; Rosedale, J. H.; Bates, F. S.; Almdal, K.; Mortensen, K. *Macromolecules* **1993**, *26*, 5959.
(7) Förster, S.; Khandpur, A. K.; Zhao, J.; Bates, F. S.; Hamley, I. W.; Ryan, A. T.; Bras, W. *Macromolecules* **1994**, *27*, 6922.
(8) Hajduk, D. A.; Harper, P. E.; Gruner, S. M.; Honeker, C. C.; Kim, G.; Thomas, E. L.; Fetters, L. J. *Macromolecules* **1994**, *27*, 4063.
(9) Schulz, M. F.; Bates, F. S.; Almdal, K.; Mortensen, K. *Phys. Rev. Lett.* **1994**, *73*, 86.
(10) While existence of the ordered bicontinuous double-diamond (OBDD) morphology has been reported, recent data re-evaluation[40] suggests that such morphologies observed are in fact G*.
(11) Laurer, J. H.; Fung, J. C.; Hajduk, D. A.; Sedat, J. W.; Agard, D. A.; Smith, S. D.; Gruner, S. M.; Spontak, R. J. Manuscript in preparation.
(12) Winey, K. I.; Thomas, E. L.; Fetters, L. J. *Macromolecules* **1991**, *24*, 6182.
(13) Hashimoto, T.; Tanaka, H.; Hasegawa, H. *Macromolecules* **1990**, *23*, 4378. Tanaka, H.; Hasegawa, H.; Hashimoto, T. *Macromolecules* **1991**, *24*, 240.
(14) Winey, K. I.; Thomas, E. L.; Fetters, L. J. *J. Chem. Phys.* **1991**, *95*, 9367.
(15) Winey, K. I.; Thomas, E. L.; Fetters, L. J. *Macromolecules* **1992**, *25*, 422, 2645.
(16) Spontak, R. J.; Smith, S. D.; Ashraf, A. *Macromolecules* **1993**, *26*, 956.

(17) Disko, M. M.; Liang, K. S.; Behal, S. K.; Roe, R.-J.; Jeon, K. J. *Macromolecules* **1993**, *26*, 2983.
(18) Spontak, R. J.; Smith, S. D.; Ashraf, A. *Polymer* **1993**, *34*, 2233.
(19) Shull, K. R.; Winey, K. I. *Macromolecules* **1992**, *25*, 2637.
(20) Banaszak, M.; Whitmore, M. D. *Macromolecules* **1992**, *25*, 2757.
(21) Matsen, M. W. *Phys. Rev. Lett.* **1995**, *74*, 4225; *Macromolecules* **1995**, *28*, 5765.
(22) Turner, D. C.; Gruner, S. M.; Huang, J. S. *Biochemistry* **1992**, *31*, 1356.
(23) Matsen, M. W.; Bates, F. S. *Macromolecules* **1995**, *28*, 7298.
(24) Zhao, J.; Majumdar, B.; Schulz, M. F.; Bates, F. S.; Almdal, K.; Mortensen, K.; Hajduk, D. A.; Gruner, S. M. *Macromolecules* **1996**, *29*, 1204.
(25) Boothroyd, A.; Rennie, A.; Wignall, G. D. *J. Chem. Phys.* **1993**, *91*, 9135.
(26) Fetters, L. J.; Lohse, D. J.; Richter, D.; Witten, T. A.; Zirkel, A. *Macromolecules* **1994**, *27*, 4639.
(27) Melenkevitz, J.; Muthukumar, M. *Macromolecules* **1991**, *24*, 4199. Lescanec, R. L.; Muthukumar, M. *Macromolecules* **1993**, *26*, 3908.
(28) Almdal, K.; Rosedale, J. H.; Bates, F. S.; Wignall, G. D.; Fredrickson, G. H. *Phys. Rev. Lett.* **1990**, *65*, 1112.
(29) Helfand, E.; Wasserman, Z. R. *Macromolecules* **1976**, *9*, 879. See also: Fredrickson, G. H. In *Physics of Polymer Surfaces and Interfaces*; Sanchez, I. C., Ed.; Butterworth-Heinemann: Boston, 1992.
(30) Semenov, A. N. *Soc. Phys. JETP (Engl. Transl.)* **1985**, *61*, 731.
(31) See, for example: Hashimoto, T.; Shibayama, M.; Kawai, H. *Macromolecules* **1980**, *13*, 1237.
(32) Hajduk, D. A.; Gruner, S. M.; Rangarajan, P.; Register, R. A.; Fetters, L. J.; Honeker, C.; Albalak, R. J.; Thomas, E. L. *Macromolecules* **1994**, *27*, 490.
(33) Hashimoto, T.; Yamasaki, K.; Koizumi, S.; Hasegawa, H. *Macromolecules* **1993**, *26*, 2895.
(34) While nonequilibrium artifacts could be avoided with parent SI copolymers of low molecular weight, the resultant blends would be of less practical interest due to reductions in χN and bulk strength.
(35) Shi, A. C.; Noolandi, J.; Hoffmann, H. *Macromolecules* **1994**, *27*, 6661.
(36) Shi, A. C.; Noolandi, J. *Macromolecules* **1994**, *27*, 2936.
(37) Spontak, R. J. *Macromolecules* **1994**, *27*, 6363.
(38) Dan, N.; Safran, S. A. *Macromolecules* **1994**, *27*, 5766.
(39) Matsen, M. W. *J. Chem. Phys.* **1995**, *103*, 3268.
(40) Zhulina, E. B.; Halperin, A. *Macromolecules* **1992**, *25*, 5730.
(41) Jones, R. L.; Kane, L.; Spontak, R. J. *Chem. Eng. Sci.* **1996**, *51*, 1365.
(42) Vilesov, A. D.; Floudas, G.; Pakula, T.; Melenevskaya, E. Yu.; Birshtein, T. M.; Lyatskaya, Yu. V. *Macromol. Chem. Phys.* **1994**, *195*, 2317.
(43) Hajduk, D. A.; Harper, P. E.; Gruner, S. M.; Honeker, C. C.; Thomas, E. L.; Fetters, L. J. *Macromolecules* **1995**, *28*, 2570.
(44) Burger, C.; Antonietti, M.; Ruland, W. *J. Chem. Phys.*, submitted for publication.
(45) Albalak, R. J.; Thomas, E. L. *J. Polym. Sci., Polym. Phys. Ed.* **1993**, *31*, 37; **1994**, *32*, 341.
(46) Thomas, E. L.; Alward, D. B.; Kinning, D. J.; Martin, D. C.; Handlin, D. L.; Fetters, L. J. *Macromolecules* **1986**, *19*, 2197.
(47) Schwark, D. W. Ph.D. Dissertation, University of Massachusetts at Amherst, 1991.
(48) Olmsted, P. D.; Milner, S. T. *Phys. Rev. Lett.* **1994**, *72*, 936.
(49) Matsen, M. W.; Schick, M. *Phys. Rev. Lett.* **1994**, *72*, 2660.
(50) Horowitz, R. A.; Agard, D. A.; Sedat, J. W.; Woodcock, C. L. *J. Cell Biol.* **1994**, *125*, 1.
(51) Moritz, M.; Braunfeld, M. B.; Fung, J. C.; Sedat, J. W.; Alberts, B. M.; Agard, D. A. *J. Cell Biol.* **1995**, *130*, 1149.
(52) McEwen, B. F.; Arena, J. J.; Frank, J.; Rieder, C. L. *J. Cell Biol.* **1993**, *120*, 301.
(53) McEwen, B. F.; Radermacher, M.; Rieder, C. L.; Frank, J. *Proc. Natl. Acad. Sci. U.S.A.* **1986**, *83*, 9040.
(54) Frank, J., Ed. *Electron Tomography: Three-Dimensional Imaging with the Transmission Electron Microscope*; Plenum: New York, 1992.
(55) Bates, R. H. T.; McDonnell, M. J. *Image Restoration and Reconstruction*; Clarendon: Oxford, U.K., 1986.
(56) Spontak, R. J.; Williams, M. C.; Agard, D. A. *Polymer* **1988**, *29*, 387.
(57) Koster, A. J.; Braunfeld, M. B.; Fung, J. C.; Abbey, C. K.; Han, K. R.; Liu, W.; Chen, H.; Sedat, J. W.; Agard, D. A. *Microsc. Soc. Am. Bull.* **1993**, *23*, 176.
(58) Fung, J. C.; Liu, W.; deRuijter, W. J.; Chen, H.; Abbey, C. K.; Sedat, J. W.; Agard, D. A. *J. Struct. Biol.*, in press.
(59) Chen, H.; Swedlow, J. R.; Grote, M.; Sedat, J. W.; Agard, D. A. In *Handbook of Biological Confocal Microscopy*; Pawley, J. B., Ed.; Plenum Press: New York, 1995.
(60) Anderson, D. M.; Bellare, J.; Hoffman, J. T.; Hoffman, D.; Gunther, J.; Thomas, E. L. *J. Colloid Interface Sci.* **1992**, *148*, 398.
(61) Hashimoto, T.; Koizumi, S.; Hasegawa, H.; Izumitani, T.; Hyde, S. T. *Macromolecules* **1992**, *25*, 1433.
(62) Laughlin, R. G. *The Aqueous Phase Behavior of Surfactants*; Academic: London, 1994. Safran, S. A. In *Micelles, Membranes, Microemulsions, and Monolayers*; Gelbart, W. M., Ben-Shaul, A., Roux, D., Eds.; Springer-Verlag: New York, 1994. See also: Luzzati, V.; Vargas, R.; Mariani, P.; Gulik, A.; Delacroix, H. *J. Mol. Biol.* **1993**, *229*, 541.
(63) Birshtein, T. M.; Lyatskaya, Yu. V.; Zhulina, E. B. *Polymer* **1990**, *31*, 2185. Zhulina, E. B.; Birshtein, T. M. *Polymer* **1991**, *32*, 1299. Lai, P.-Y.; Zhulina, E. B. *Macromolecules* **1992**, *25*, 5201.

MA9515689

Appendix 2:

Architecture-Induced Phase Immiscibility in Diblock/Multiblock Copolymer Blend

Macromolecules **1996,** *29,* 2850−2856

Architecture-Induced Phase Immiscibility in a Diblock/Multiblock Copolymer Blend

Richard J. Spontak,*,† Jennifer C. Fung,‡ Michael B. Braunfeld,§ John W. Sedat,§ David A. Agard,§ Arman Ashraf,⊥ and Steven D. Smith*,⊥

Department of Materials Science & Engineering, North Carolina State University, Raleigh, North Carolina 27695, Graduate Group in Biophysics and Department of Biophysics & Biochemistry and Howard Hughes Medical Institute, University of California, San Francisco, California 94143, and Corporate Research Division, The Procter & Gamble Company, Cincinnati, Ohio 45239

Received October 24, 1995; Revised Manuscript Received December 27, 1995[⊗]

ABSTRACT: Ordered diblock copolymer blends have recently become the subject of tremendous research interest since they can be used to elucidate the intramicrodomain segregation of blocks differing in length, as well as to identify the molecular and blend parameters yielding phase immiscibility. In this work, we explore the influence of molecular architecture on block copolymer blend miscibility by examining an equimolar mixture of two symmetric styrene (S)/isoprene (I) block copolymers, one an SI diblock and the other an $(SI)_4$ octablock. Their molecular weights are identical, so that the ratio of block lengths is 4:1 SI:$(SI)_4$. While this ratio is expected to yield a single phase in diblock copolymer blends, transmission electron microscopy reveals here that the diblock/multiblock blend is macrophase-separated due to the linear multiblock architecture and midblock conformations of the $(SI)_4$ copolymer. Electron tomography (3D imaging) permits direct visualization of connected SI and $(SI)_4$ microdomains at the SI/$(SI)_4$ interface at relatively high spatial resolution (ca. 3 nm). In addition, the presence of SI molecules in the $(SI)_4$ phase or $(SI)_4$ molecules in the SI phase frustrates SI lamellae, resulting in curved microphase boundaries.

Introduction

Microphase-ordered block copolymers continue to constitute a fascinating, and technologically important, class of materials since they elucidate the factors governing polymer self-assembly and exhibit a wide (and controllable) range of properties.[1−4] While the morphology and properties of a neat block copolymer can be altered[5−7] or refined[8−10] through processing, they are usually tailored for a specific application via chemical synthesis. Another, potentially more effective, route by which to obtain a microphase-ordered polymeric material possessing particular morphological characteristics or properties is through blending at the molecular level. Studies of diblock copolymer/homopolymer blends, for instance, have demonstrated that the addition of a parent homopolymer (hA) to an ordered (usually lamellar) AB copolymer can result in either preferential microstructural swelling,[11,12] a morphological transition,[13−16] or macrophase separation,[14] depending on both the blend volume-fraction composition (Φ_A) and the molecular weight of hA relative to that of the A block of the copolymer (M_{hA}/M_A). In fact, theoretical studies[17] predict that a wide variety of morphologies can be readily accessed through the use of AB/hA blends.

To avoid the complication of hA localization within the host microdomains of such blends, recent efforts have begun to focus more on the use of block copolymer/copolymer, $(AB)_\alpha/(AB)_\beta$, blends as an alternative means to produce microphase-ordered materials with controlled morphologies and properties. While this idea is not new,[18] such blends thus far have expedited the study of (i) morphological transitions between adjacent microphases,[19−21] (ii) intramicrodomain block mixing and conformations,[22−25] and (iii) molecular/blend parameters responsible for either morphological coexistence or phase immiscibility.[23,25−27] According to experimental studies[22,26] and self-consistent field (SCF) predictions,[25] phase immiscibility between two symmetric diblock copolymers (of equal composition) occurs when the ratio of copolymer chain lengths (N_α/N_β, with $N_\alpha > N_\beta$) exceeds a critical value that is dependent on the thermodynamic incompatibility (χN, where χ is the Flory−Huggins interaction parameter) of the longer α copolymer. It is important to recognize at this juncture that the blocks of each diblock copolymer in a binary $(AB)_\alpha/(AB)_\beta$ blend are constrained only at one end, in which case the α and β blocks occupying each microphase in the blend constitute a bidisperse mixture of grafted chains that comprises a two-tier polymer brush[28] (with the long α blocks forcing the short β blocks to reside in a boundary layer adjacent to the highly repulsive microdomain interphase). Phase immiscibility in such blends therefore is the result of a critical difference in copolymer block lengths.

In contrast to diblock copolymers, perfectly alternating linear $(AB)_n$ multiblock copolymers with $n > 1$ (n denotes the number of AB block pairs) consist of 2 single-grafted endblocks and $2(n - 1)$ double-grafted midblocks, each of which is capable of adopting a bridged or looped conformation (see Figure 1). Previous experimental[29−32] and theoretical[33] studies have demonstrated that, at constant χ, the microstructural dimensions of symmetric $(AB)_n$ copolymers are dependent on molecular factors such as n and N, as well as on conformational factors such as q, where q denotes the fraction of bridged midblocks present in the lamellar microstructure. Related studies[34] have also shown that the linear multiblock architecture and the existence of bridged/looped midblock conformations effect a reduction in the miscibility of $(AB)_n$/hA blends. While blend composed of hA and an AB diblock copolymer ($M_{hA}/M_{AB} \approx 0.5$) are miscible at $\Phi_A = 0.66$, for example, identical blends with an $(AB)_n$ copolymer ($2 \leq n \leq 4$) are not.

* Authors to whom correspondence should be addressed.
† North Carolina State University.
‡ Graduate Group in Biophysics, University of California.
§ Department of Biophysics & Biochemistry and Howard Hughes Medical Institute, University of California.
⊥ The Procter & Gamble Co.
⊗ Abstract published in *Advance ACS Abstracts,* February 15, 1996.

0024-9297/96/2229-2850$12.00/0

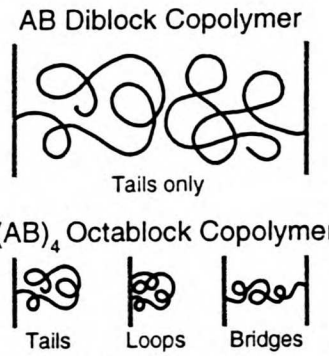

Figure 1. Schematic illustration showing the differences in chain length and conformations of the AB diblock and $(AB)_4$ octablock copolymers examined in this study. While diblock molecules are restricted to one conformation, an octablock molecule may assume any one of 64 conformations, with each of its 6 midblocks adopting either a bridged or looped conformation.

The objective of this work is to examine the phase behavior of an equimolar diblock/multiblock copolymer blend. Conventional and advanced transmission electron microscopy (TEM) techniques, including intermediate-voltage electron microscopic tomography (IVEM-T), are employed here to characterize the blend morphology, so that the effect of copolymer architecture on copolymer/copolymer blend miscibility can be discerned.

Experimental Section

Materials. Two block copolymers composed of styrene (S) and isoprene (I) monomers were synthesized in the presence of *sec*-butyllithium catalyst via living anionic polymerization in cyclohexane at 60 °C. One copolymer was a symmetric (50:50 wt % S/I) SI diblock with $\bar{M}_n$ = 120 000 (60 000 blocks) and $\bar{M}_w/\bar{M}_n \approx 1.05$, while the other was a symmetric $(SI)_4$ octablock with $\bar{M}_n$ = 120 000 (15 000 blocks) and $\bar{M}_w/\bar{M}_n \approx 1.09$. Copolymer compositions and molecular weights/molecular weight distributions were measured by ^{1}H NMR and GPC, respectively, and are described in detail elsewhere.[29] On the basis of small-angle X-ray scattering (SAXS) results,[35] the thermodynamic incompatibility (χN) of the SI copolymer is estimated to be about 86 at its upper glass transition temperature (≈100 °C, from differential scanning calorimetry), indicating that the neat copolymer resides in the intermediate-segregation regime at ambient temperature.

Methods. Equal masses of the two copolymers were dissolved in toluene to produce a 4% (w/v) solution, which, upon complete copolymer dissolution (12 h), was cast into a Teflon mold. To obtain a near-equilibrium blend morphology, solvent was removed slowly over the course of 3 weeks, and the resultant film, measuring ca. 2 mm thick, was heated at 100 °C under low vacuum for 5 h to remove residual solvent. The film was subsequently encapsulated in a glass tube that was first cycled between Ar and vacuum three times and then subjected to 160 °C for 1 week. No gross signs of thermooxidative degradation were evident, and the film readily redissolved in toluene (suggesting that little, if any, cross-linking occurred during heat treatment). The film was trimmed so that its interior (presumably removed from surface artifacts) could be cross-sectioned on a Reichert-Jung Ultracut-S microtome maintained at −100 °C. Sections measuring less than 100 nm thick were subsequently stained with the vapor of 2% OsO_4(aq) for 90 min to enhance electron contrast between the S and I microphases. Specimens employed in electron tomography were coated with a 1% polylysine solution to enhance surface hydrophilicity and then decorated with 30 nm colloidal gold (required as reference markers, as described in the following).

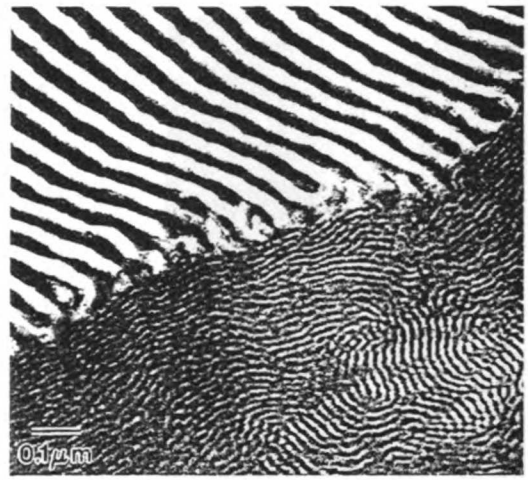

Figure 2. Transmission electron micrograph of an equimolar SI/$(SI)_4$ blend, revealing that the blend, is immiscible and that the SI and $(SI)_4$ phases (large and small lamellae, respectively) are separated by relatively sharp interfaces.

Conventional TEM micrographs were obtained on a Zeiss EM902 electron spectroscopic microscope operated at 80 kV and ΔE = 50 eV. For IVEM-T, digital images of an SI/$(SI)_4$ interface were collected on a 12 bits/pixel cooled slow-scan CCD camera in a Philips 430 electron microscope operated at 200 kV. The image resolution was 1.7 nm/pixel. Forty-nine 480 × 480 pixel images were collected from a single specimen at tilt angles (θ) ranging from −60° to 60° in 2.5° increments along a single-tilt axis. Of these, 43 images were mass-normalized (i.e., converted from image intensity to mass density) and then aligned (by least-squares minimization) by using eight colloidal gold beads as fiducial markers. Upon satisfactory alignment, as discerned from the mean error in bead position (σ), the image stack was reconstructed according to the *r*-weighted (filtered) back-projection method[21,36-38] using the EMCAT reconstruction software package.[39] The resultant 3D volume element was displayed and analyzed in the PRIISM image graphics package,[40] where it was sliced along orthogonal directions to facilitate parallel and perpendicular viewing of the interface.

Results and Discussion

Presented in Figure 2 is a conventional TEM micrograph of the macroscopic interface separating the SI and $(SI)_4$ phases, clearly revealing that these two copolymers, while of equal molecular weight and composition, are immiscible. The ratio of block lengths between these two copolymers is 4:1 SI:$(SI)_4$, which is less than that needed for immiscibility in a symmetric blend of two diblock copolymers (about 5.6:1, as discerned from the predictions provided in ref 33 evaluated at χN_α = 80, where α denotes the longer copolymer). According to the SAXS and TEM data of Hashimoto *et al.*[26] and Kane *et al.*,[41] ordered diblock copolymers remain fully miscible for $\bar{M}_n$ ratios less than 5.2:1. Thus, it is reasonable to attribute the copolymer immiscibility evident in Figure 2 to the molecular architecture of the $(SI)_4$ molecules, each of which contains six midblocks that are capable of adopting either a bridged or a looped conformation. Since either conformation halves the lateral extension of a midblock along the lamellar normal (relative to that of an endblock), the ratio between SI endblocks and (SI) midblocks is effectively 8:1, which exceeds the experimental and predicted miscibility limits for two diblock copolymers.

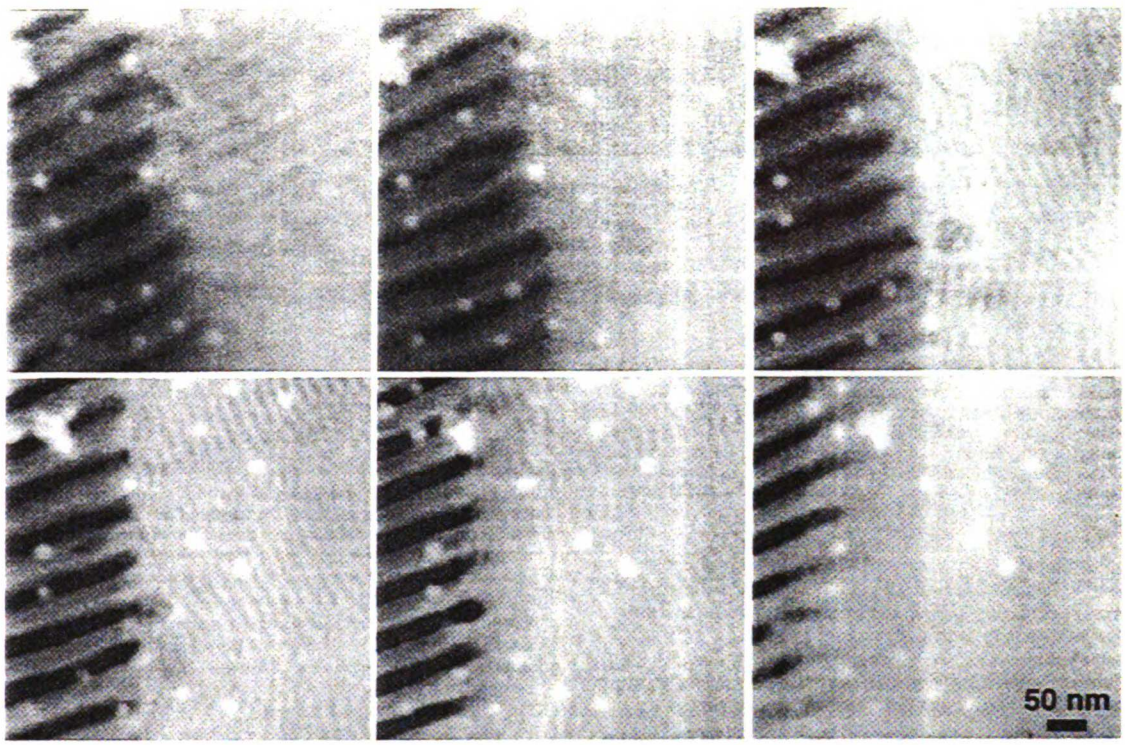

Figure 3. Series of digital micrographs of the SI/(SI)$_4$ interface at tilt angles ranging from −45° to 30° in 15° increments (from left to right and top to bottom) along a single-tilt axis. The images are contrast-reversed, mass-normalized, and aligned to facilitate viewing. The bright dots correspond to the colloidal gold beads used during image alignment.

Microdomain periodicities of the SI and (SI)$_4$ phases measured from micrographs such as the one shown in Figure 2 are about 60 and 18 nm, respectively. These values are in excellent agreement with those reported earlier,[29,30,32] indicating that (i) the lamellae in each phase are virtually unaffected by those comprising the coexisting phase and (ii) SI/(SI)$_4$ mixing is, for the most part, minimal. In marked contrast, TEM and SAXS data obtained from immiscible diblock copolymer blends reveal that the α phase typically consists of 15−35% β, while the β phase is almost pure β.[26]

A series of digital TEM images showing the SI/(SI)$_4$ interface at different tilt angles between −45° and 30° in 15° increments is displayed in Figure 3. These images are all contrast-reversed to facilitate visualization of the alternating lamellae in each phase and identification of the colloidal gold beads (which appear as small bright dots). The SI/(SI)$_4$ interface is relatively sharp and is oriented almost parallel to the electron beam at θ = 0°. As θ is increased or decreased substantially from 0°, the corresponding 2D TEM projections are seen to consist of superpositioned lamellae from each phase. In addition to being mass-normalized, these images have also been aligned with respect to the colloidal gold beads evident in the figure. The mean error σ incurred during alignment (averaged over all of the beads utilized) is shown as a function of θ in Figure 4, which reveals that, in 98% of the images, σ lies below the image resolution of 1 pixel. In fact, the overall σ averaged over the entire series of collected images is only 1.0 nm, as compared to the image sampling of 1.7 nm/pixel. Contributing to the alignment error is sample shrinkage induced by radiation damage

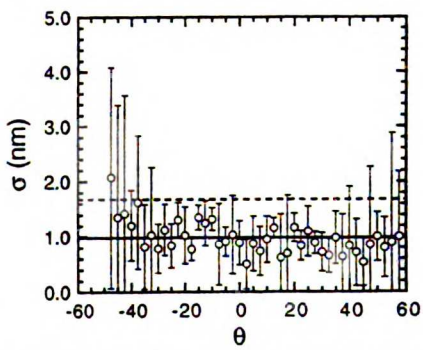

Figure 4. Mean alignment error (σ) as a function of tilt angle (θ). The vertical bars denote the standard deviation in σ, whereas the solid and dashed horizontal lines correspond to the overall mean σ (averaged over all θ) and the image resolution (per pixel).

under the electron beam. By comparing the positions of the colloidal gold beads before and immediately after collection of the tilt series, we estimate that the TEM specimen shrank laterally by about 1.8% during the course of image acquisition.

Unlike model-dependent methods in which 2D TEM micrographs are compared to projections of a postulated structure of known symmetry,[42,43] electron tomography permits direct visualization of the complete 3D structure of an object *in situ*, reconstructed from a set of tilted views. Since this powerful method does not make any *a priori* assumptions or impose any requirements regarding the symmetry of the object, it has been prover

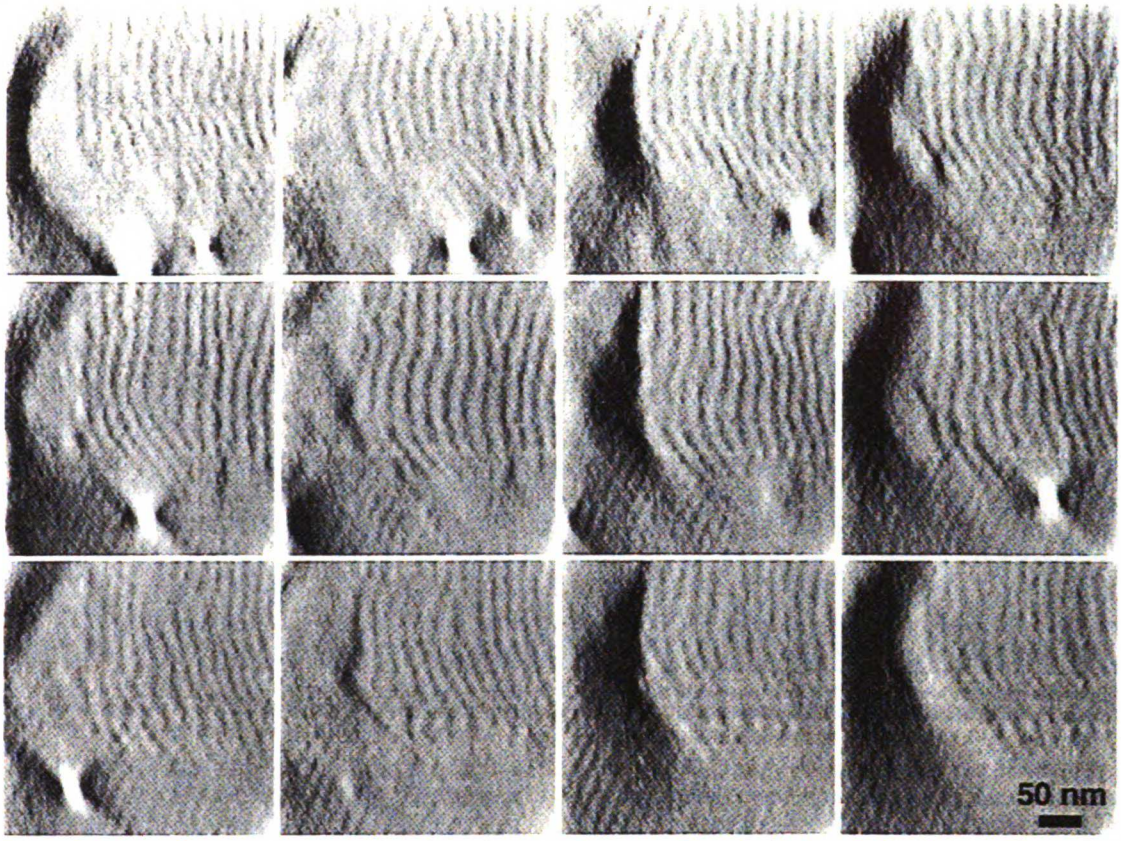

Figure 5. Slices of the reconstructed volume element generated from a complete series of tilt projections (6 out of 43 are shown in Figure 3) by the *r*-weighted (filtered) back-projection method. Each *xz* slice proceeds along the *y*-axis (perpendicular to the electron beam) from left to right and top to bottom. Bright dots correspond to colloidal gold beads.

to be extremely useful in the analysis of complex biological structures,[44-46] as well as of microphase-ordered block copolymers.[21,38] Two-dimensional (contrast-reversed) slices of the reconstructed volume element obtained from the complete series of 43 tilt projections are shown in Figures 5 and 6. Each slice is about 17 nm. To put this into proper perspective, a series of distortion-free sections of comparable thickness would be impossible to obtain by microtomy. While a solid reconstruction, in addition to or instead of the slices, could be provided here, it would not prove to be very beneficial due to the size difference between SI and $(SI)_4$ lamellae. The slices in Figure 5 are *xz* images displayed at different positions along the *y*-axis, where the *x*- and *y*-axes are normal to the electron beam and the *z*-axis is parallel to the electron beam. Large intermittent structures evident in the left portion of the images correspond to cross-sectioned lamellae in the SI phase, whereas the small lamellae evident in the slices are indicative of the $(SI)_4$ phase. Note that the $(SI)_4$ lamellae in this image series exhibit a $S_{1/2}$ disclination that clearly propagates away from the interface as the *y*-axis is traversed. The bright dot seen in one of the images once again identifies a dispersed colloidal gold bead and serves as an additional check on reconstruction accuracy; i.e., the better the reconstruction, the more circular the beads appear in cross section.

Images in Figure 6 are *xy* slices along the *z*-axis and clearly show the SI/$(SI)_4$ interface as in Figure 2. The difference between the images in Figures 2 and 6 is that the thin slices in Figure 6, containing less projected information and therefore exhibiting less interference, facilitate detailed visualization of interfacial features. In particular, the reader's attention is drawn to the points where the SI lamellae are physically connected to the adjacent $(SI)_4$ lamellae. While it is intuitively obvious that the lamellae from each phase must somehow be connected, no previous efforts have provided direct evidence for microphase connectivity (adhesion) in a copolymer/copolymer blend, especially at this spatial resolution. An understanding of such connectivity is vital to the design of multiphasic materials with interface-limited mechanical properties. As the *z*-axis is traversed, the images in Figure 6 reveal that SI/$(SI)_4$ lamellar adhesion can be lost and regained due to mismatch between the lamellar periodicities of the SI and $(SI)_4$ phases.

Thus far, only the interface separating the immiscible SI and $(SI)_4$ phases has been examined. In this section, we explore the morphologies that result when $(SI)_4$ molecules are trapped within the SI phase and when SI molecules reside in the $(SI)_4$ phase. As seen in the conventional TEM micrograph provided in Figure 7, the presence of short $(SI)_4$ molecules in the SI phase induces localized regions wherein the SI lamellae are highly frustrated, as evidenced by pinched lamellae and microstructural elements with nonzero curvature. To appreciate the influence of $(SI)_4$ midblock conformation

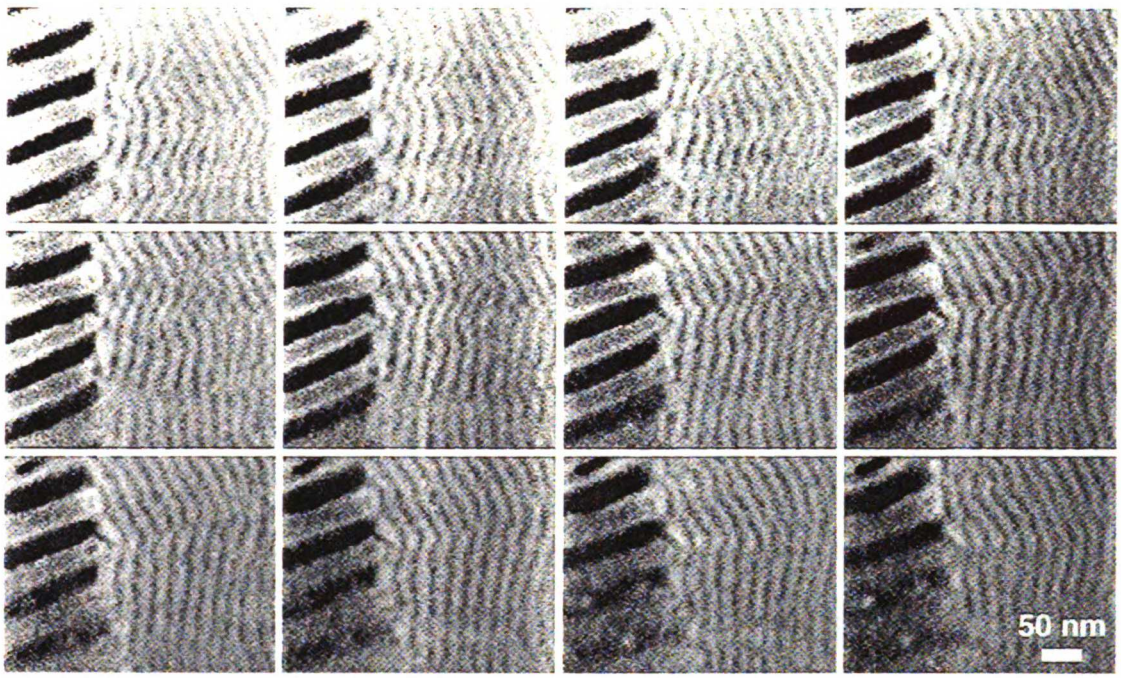

Figure 6. Series of sequential *xy* slices along the *z*-axis (parallel to the electron beam) from left to right and top to bottom. Each slice, measuring about 17 nm thick, reveals that the large lamellae of the SI copolymer adhere to the smaller lamellae of the $(SI)_4$ copolymer at discrete junction sites along the interface.

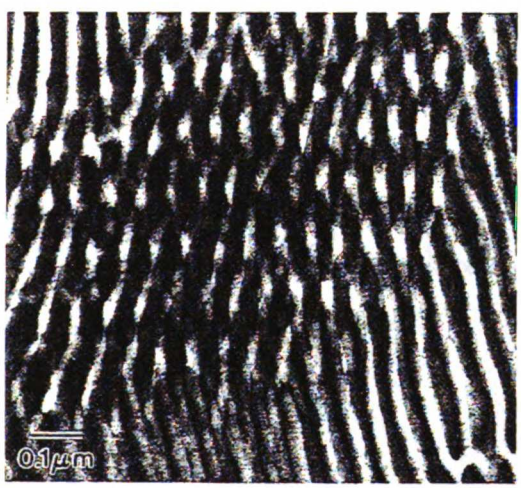

Figure 7. Conventional electron micrograph of an isolated region in the SI phase wherein $(SI)_4$ molecules have been trapped during macrophase separation. The presence of $(SI)_4$ molecules within SI lamellae serves to "pinch" the lamellae and consequently frustrate the local SI lamellar order, resulting in microdomain boundaries with nonzero mean curvature.

on SI conformations and lamellar microstructure, a schematic illustration of SI/$(SI)_4$ mixtures is presented in Figure 8. In the event that all of the $(SI)_4$ midblocks adopt a looped conformation (Figure 8a), the diblock/octablock blend is anticipated to behave as a blend of two diblock copolymers differing in block length by a factor of 8 (recall that a looped midblock is comparable to two single-grafted endblocks of half chain length). According to SCF predictions,[25] phase miscibility in such a diblock copolymer blend (with $\chi N_\alpha = 80$) is retained only up to about 27 vol % β copolymer. Figure 7 demonstrates, however, that innocuous incorporation of $(SI)_4$ molecules into the SI phase is not achieved. The frustrated lamellar morphology seen in this figure suggests that some of the $(SI)_4$ midblocks assume a bridged conformation, squeezing the longer SI molecules along the lamellar parallel (rather than allowing them to stretch along the lamellar normal) to satisfy the requirement of uniform density. Depending on the $(SI)_4$ midblock conformations in neighboring lamellae, squeezed SI molecules could conceivably induce a change in interfacial curvature (and in morphology) through chain packing considerations (see Figure 8b).

If SI molecules are trapped within the $(SI)_4$ phase during either micro- or macrophase separation, they could be similarly constrained, as seen by the SI inclusion in Figure 9. Rather than appearing as a multilamellar ("onion-skinned") vesicle, as block copolymers typically do when they macrophase-separate from, for example, a parent homopolymer of relatively high molecular weight, the SI inclusion seen here once again exhibits a frustrated lamellar-like morphology. Thus, the micrographs in Figures 7 and 9 indicate that, while the SI and $(SI)_4$ phases are almost completely demixed, isolated regions exist in each phase where the dissimilar copolymer molecules are forced to interact locally. In contrast, discrete homopolymer inclusions observed[34,47] in copolymer/homopolymer blends remain, for the most part, demixed due to strongly repulsive interactions between the homopolymer and the chemically dissimilar block of the copolymer. This is not, however, the case in the SI/$(SI)_4$ blend in which the macromolecules comprising the inclusions and matrix are compositionally identical and are both capable of self-assembling into ordered microstructures to minimize the magnitude of unfavorable interactions between covalently linked

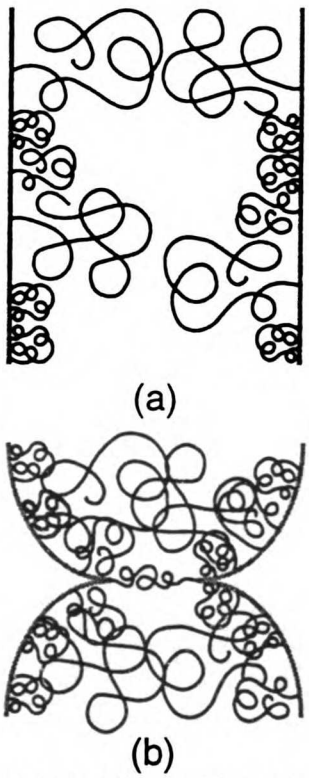

Figure 8. Illustration of SI and $(SI)_4$ copolymer molecules residing in the same microdomain. In (a), the $(SI)_4$ molecules adopt a completely looped conformation so that the blend can be envisioned as a diblock copolymer/copolymer blend in which the block length ratio is 8:1 SI:$(SI)_4$. If the midblocks of the $(SI)_4$ molecules assume a bridged conformation, they constrain and squeeze the longer SI blocks, as in (b).

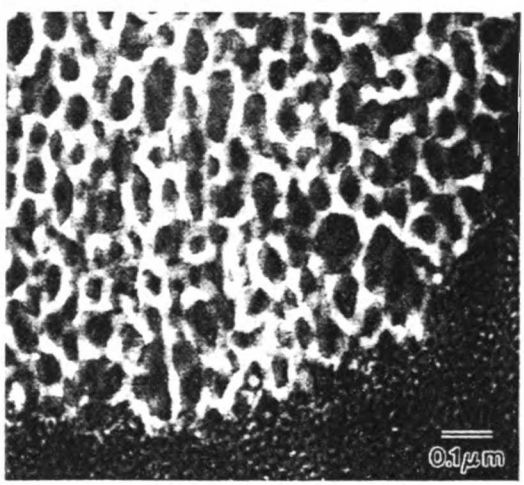

Figure 9. Electron micrograph of an SI copolymer inclusion residing in the $(SI)_4$ matrix. The nonlamellar SI morphology evident here is indicative of mixing between SI and $(SI)_4$ molecules within the inclusion.

blocks. This shared characteristic of the SI and $(SI)_4$ copolymer molecules therefore is responsible for limited intramicrodomain mixing, while the architecture of the $(SI)_4$ copolymer is responsible for SI microdomain frustration, within the isolated regions seen in Figures 7 and 9.

Conclusions

An equimolar blend of a diblock copolymer and an octablock copolymer, both of identical composition and molecular weight, is found to be immiscible. Electron micrographs show that the blend exhibits clearly defined macroscopic interfaces, as well as isolated (and highly frustrated) inclusions of one copolymer within a matrix of the other. In addition, electron tomography has been employed to explore the features of the blend interface at relatively high resolution (ca. 3 nm). Slices parallel and perpendicular to the interface reveal that (i) the octablock phase in close proximity to the interface comprises defects (due to periodicity mismatch) that propagate normal to the interface and (ii) adhesion between the diblock and octablock phases is a result of discretely connected lamellae. These results demonstrate that electron tomography can provide heretofore unavailable adhesion information from interfaces and could be of tremendous value in the study of related structural characteristics, e.g., grain boundaries,[48] in ordered block copolymer systems. Comparison of the morphological features observed here with experimental data[26] and theoretical predictions[25] reported for immiscible diblock copolymer blends suggests that the molecular architecture and midblock conformations of the octablock copolymer are responsible for diblock/octablock blend immiscibility. With this observation in mind, block architecture and conformation should be considered carefully as a design criterion in technological applications employing multiblock copolymers and their blends.

Acknowledgment. This work has been supported by the National Science Foundation (CMS-941-2361) and the Director, Office of Energy Research, Office of Basic Energy Sciences, Materials Science Division of the U.S. Department of Energy, under contract DE-AC03-76SF00098. One of us (R.J.S.) thanks the National Center for Electron Microscopy for a Visiting Scientist Fellowship and Drs. K. M. Krishnan and U. Dahmen for valuable discussions. Funding for D.A.A., J.W.S., M.B.B., and J.C.F. was provided by the Howard Hughes Medical Institute and the National Institutes of Health (GM31627, D.A.A.; GM25101, J.W.S.). We are grateful to Mr. H. Chen (UCSF) for valuable technical assistance.

References and Notes

(1) Leibler, L. *Macromolecules* **1980**, *13*, 1602.
(2) Legge, N. R.; Holden, G.; Schroeder, H. E., Eds. *Thermoplastic Elastomers: A Comprehensive Review*; Hanser: New York, 1987.
(3) Fredrickson, G. H.; Bates, F. S. *Annu. Rev. Phys. Chem.* **1990**, *41*, 525.
(4) Binder, K. *Phys. Scr.* **1994**, *55*, 206.
(5) Almdal, K.; Koppi, K. A.; Bates, F. S.; Mortensen, K. *Macromolecules* **1992**, *25*, 1743.
(6) Hajduk, D. A.; Gruner, S. M.; Rangarajan, P.; Register, R. A.; Fetters, L. J.; Honeker, C.; Albalak, R. J.; Thomas, E. L. *Macromolecules* **1994**, *27*, 490.
(7) Jackson, C. L.; Barnes, K. A.; Morrison, F. A.; Mays, J. W.; Nakatani, A. I.; Han, C. C. *Macromolecules* **1995**, *28*, 713.
(8) Albalak, R. J.; Thomas, E. L. *J. Polym. Sci., Polym. Phys. Ed.* **1993**, *31*, 37; **1994**, *32*, 341.
(9) Scott, D. B.; Waddon, A. J.; Lin, Y. G.; Karasz, F. E.; Winter H. H. *Macromolecules* **1992**, *25*, 4175.
(10) Winey, K. I.; Patel, S. S.; Larson, R. G.; Watanabe, H *Macromolecules* **1993**, *26*, 2542.
(11) Winey, K. I.; Thomas, E. L.; Fetters, L. J. *Macromolecule* **1991**, *24*, 6182.

(12) Tanaka, H.; Hasegawa, H.; Hashimoto, T. *Macromolecules* **1991**, *24*, 240. Kimishima, K.; Hashimoto, T.; Han, C. C. *Macromolecules* **1995**, *28*, 3842.
(13) Winey, K. I.; Thomas, E. L.; Fetters, L. J. *J. Chem. Phys.* **1991**, *95*, 9367.
(14) Winey, K. I.; Thomas, E. L.; Fetters, L. J. *Macromolecules* **1992**, *25*, 422, 2645.
(15) Spontak, R. J.; Smith, S. D.; Ashraf, A. *Macromolecules* **1993**, *26*, 956.
(16) Disko, M. M.; Liang, K. S.; Behal, S. K.; Roe, R.-J.; Jeon, K. J. *Macromolecules* **1993**, *26*, 2983.
(17) Matsen, M. W. *Phys. Rev. Lett.* **1995**, *74*, 4225. Matsen, M. W. *Macromolecules* **1995**, *28*, 5765.
(18) Hadziioannou, G.; Skoulios, A. *Macromolecules* **1982**, *15*, 267.
(19) Zhao, J.; Majumdar, B.; Schulz, M. F.; Bates, F. S.; Almdal, K.; Mortensen, K.; Hajduk, D. A.; Gruner, S. M. *Macromolecules*, in press.
(20) Vilesov, A. D.; Floudas, G.; Pakula, T.; Melenevskaya, E. Yu.; Birshtein, T. M.; Lyatskaya, Yu. V. *Macromol. Chem. Phys.* **1994**, *195*, 2317.
(21) Spontak, R. J.; Fung, J. C.; Braunfeld, M. B.; Sedat, J. W.; Agard, D. A.; Kane, L.; Smith, S. D.; Satkowski, M. M.; Ashraf, A.; Hajduk, D. A.; Gruner, S. M. *Macromolecules*, submitted.
(22) Mayes, A. M.; Russell, T. P.; Deline, V. R.; Satija, S. K.; Majkrzak, C. F. *Macromolecules* **1994**, *27*, 7447.
(23) Shi, A.-C.; Noolandi, J.; Hoffmann, H. *Macromolecules* **1994**, *27*, 6661. Shi, A.-C.; Noolandi, J. *Macromolecules* **1994**, *27*, 2936.
(24) Spontak, R. J. *Macromolecules* **1994**, *27*, 6363.
(25) Matsen, M. W. *J. Chem. Phys.* **1995**, *103*, 3268.
(26) Hashimoto, T.; Yamasaki, K.; Koizumi, S.; Hasegawa, H. *Macromolecules* **1993**, *26*, 2895. Hashimoto, T.; Koizumi, S.; Hasegawa, H. *Macromolecules* **1994**, *27*, 1562.
(27) Matsen, M. W.; Bates, F. S. *Macromolecules* **1995**, *28*, 7298.
(28) Milner, S. T.; Witten, T. A.; Cates, M. E. *Macromolecules* **1989**, *22*, 853.
(29) Spontak, R. J.; Smith, S. D.; Satkowski, M. M.; Ashraf, A.; Zielinski, J. M.; In *Polymer Solutions, Blends, and Interfaces*; Noda, I., Rubingh, D. N., Eds.; Elsevier: Amsterdam, 1992.
(30) Smith, S. D.; Spontak, R. J.; Satkowski, M. M.; Ashraf, A.; Lin, J. S. *Phys. Rev. B* **1993**, *47*, 14555.
(31) Matsushita, Y.; Mogi, Y.; Mukai, H.; Watanabe, J.; Noda, I. *Polymer* **1994**, *35*, 246.
(32) Smith, S. D.; Spontak, R. J., Satkowski, M. M.; Ashraf, A.; Heape, A. K.; Lin, J. S. *Polymer* **1994**, *36*, 4527.
(33) Matsen, M. W. *J. Chem. Phys.* **1995**, *102*, 3884.
(34) Spontak, R. J.; Smith, S. D.; Ashraf, A. *Macromolecules* **1993**, *26*, 5118.
(35) Hong, S.-U.; Duda, J. L.; Smith, S. D.; Hajduk, D. A.; Spontak, R. J. *Macromolecules*, manuscript in preparation.
(36) Frank, J., Ed. *Electron Tomography: Three-Dimensional Imaging with the Transmission Electron Microscope*; Plenum: New York, 1992.
(37) Bates, R. H. T.; McDonnell, M. J. *Image Restoration and Reconstruction*; Clarendon: Oxford, UK, 1986.
(38) Spontak, R. J.; Williams, M. C.; Agard, D. A. *Polymer* **1988**, *29*, 387.
(39) Fung, J. C.; Liu, W.; deRuijter, W. J.; Chen, H.; Abbey, C. K.; Sedat, J. W.; Agard, D. A. *J. Struct. Biol.*, in press.
(40) Chen, H.; Swedlow, J. R.; Grote, M.; Sedat, J. W.; Agard, D. A. In *Handbook of Biological Confocal Microscopy*; Pawley, J. B., Ed.; Plenum Press: New York, 1995.
(41) Kane, L.; Smith, S. D.; Satkowski, M. M.; Ashraf, A.; Spontak, R. J. Presented at the Intersociety Polymer Conference, Baltimore, MD, October 1995. Kane, L. M.S. Thesis, North Carolina State University, in progress.
(42) Anderson, D. M.; Bellare, J.; Hoffman, J. T.; Hoffman, D.; Gunther, J.; Thomas, E. L. *J. Colloid Interface Sci.* **1992**, *148*, 398.
(43) Burger, C.; Antonietti, M.; Ruland, W. *J. Chem. Phys.*, submitted.
(44) McEwen, B. F.; Arena, J. J.; Frank, J.; Rieder, C. L. *J. Cell Biol.* **1993**, *120*, 301.
(45) Horowitz, R. A.; Agard, D. A.; Sedat, J. W.; Woodcock, C. L. *J. Cell Biol.* **1994**, *125*, 1.
(46) Moritz, M.; Braunfeld, M. B.; Fung, J. C.; Sedat, J. W.; Alberts, B. M.; Agard, D. A. *J. Cell Biol.* **1995**, *130*, 1149.
(47) Pan, T.; Huang, K.; Balazs, A. C.; Kunz, M. S.; Mayes, A. M.; Russell, T. P. *Macromolecules* **1993**, *26*, 2860.
(48) Gido, S. P.; Gunther, J.; Thomas, E. L.; Hoffman, D. *Macromolecules* **1993**, *26*, 4506. Gido, S. P.; Thomas, E. L. *Macromolecules* **1994**, *27*, 849, 6137.

MA9515691

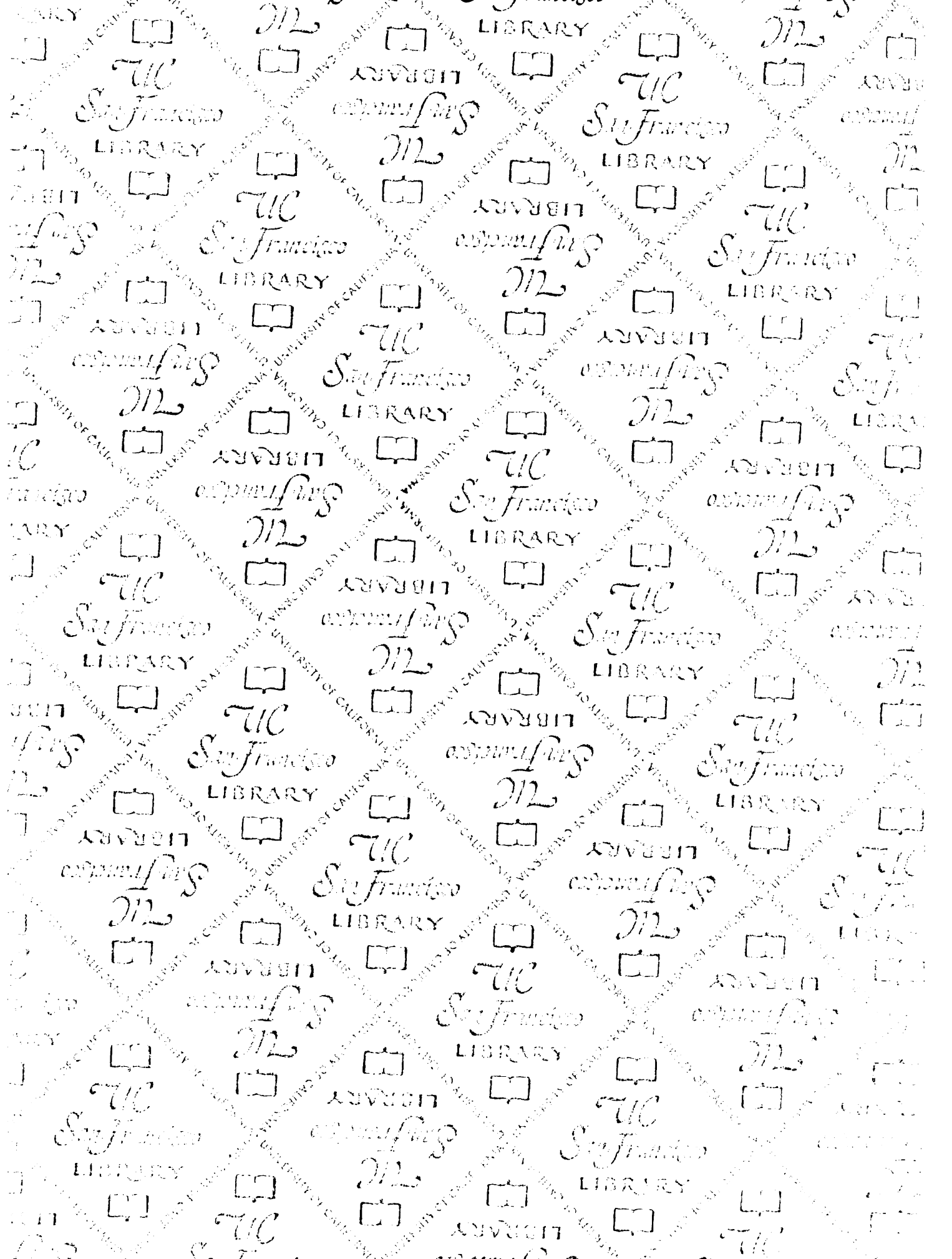
UC
San Francisco
LIBRARY